**Title**

Topological Electronic Properties and Optical Properties of Graphene Nanoribbons and Carbon Conjugated Systems



**Author**

Zhao, Fangzhou

**Publication Date**

2021

Peer reviewed|Thesis/dissertation

# Topological Electronic Properties and Optical Properties of Graphene Nanoribbons and Carbon Conjugated Systems

by

Fangzhou Zhao

A dissertation submitted in partial satisfaction of the

requirements for the degree of

Doctor of Philosophy

in

Physics

in the

Graduate Division

of the

University of California, Berkeley

Committee in charge:

Professor Steven G. Louie, Chair
Professor Michael F. Crommie
Professor Felix R. Fischer

Spring 2021

Topological Electronic Properties and Optical Properties of Graphene Nanoribbons and Carbon Conjugated Systems

Abstract

Topological Electronic Properties and Optical Properties of Graphene Nanoribbons and Carbon Conjugated Systems

by

Fangzhou Zhao

Doctor of Philosophy in Physics

University of California, Berkeley

Professor Steven G. Louie, Chair

In condensed matter physics, first-principles methodologies play a significant role in understanding various interesting phenomena and physical laws, such as electronic and optoelectronic properties of crystals. And low dimensional materials exhibit many extraordinary physical properties due to quantum confinement, enhanced interaction, and special screening effects, and so on. Quasi-one-dimensional graphene nanoribbons (GNRs) are a promising new platform for future nanoelectronics applications, and the recent booming development of bottom-up synthesis techniques enables atomically precise synthesis of GNRs, so that GNRs of different widths, edge shapes and dopants could be well-studied.

This dissertation mainly focuses on the theoretical and computational study of the topological electronic properties of GNRs, the substrate interaction of doped GNRs, the design of a double-quantum-well GNR transistor, and the optical properties of conjugated polymers. This dissertation is organized as follows:

- In Chapter 1, we review the theoretical and computational methodologies that we used to calculate the electronic and optical properties of relevant low-dimensional materials in the dissertation, including density functional theory (DFT) for ground-state properties as well as the GW and the GW plus Bethe-Salpeter equation (GW-BSE) methods for excited-state properties.
- In Chapter 2, we present our study on the topological phases of armchair, cove-edged, and chevron GNRs, as well as GNRs with dopants by first-principles calculations and model-related methods. We further present a novel design of a periodically doped GNR structures with electric field tunable topological properties, which may have potential application in nanoelectronics.

- In Chapter 3, we show our detailed investigation of the bulk-edge correspondence in $Z_2$ classification of quasi 1D systems by using model and first-principles calculations.

- In Chapter 4, we present a first-principles study of electronic properties of GNRs collaborated with the experimental groups. We investigate the strong interaction between the metallic substrate and the dopant states of the boron-doped armchair GNR for different doping concentrations. Strong substrate interactions have been observed both by first-principles calculations and scanning tunneling spectroscopy (STS) measurements.

- Chapter 5 focuses on an application study of the GNRs. We design a double-quantum-well GNR transistor and analyze the possibility of using such a device to break the thermal limit in the swing voltage in order to build energy efficient transistors. We test the validity of a double-quantum-well GNR transistor, and obtain the analytical form of spectral lineshapes of a quantum dot state coupled to a metallic wire with finite band width. The findings shown in this chapter reveal the theoretical principles in designing nanoelectronic transistors with low swing voltages.

- In Chapter 6, we present our first-principles study on the optical and excitonic properties of conjugated polymers using the GW-BSE methodology. We present detailed investigations on different approximations used in density functional theory and GW-BSE calculations and their effects to the calculated results. The new calculated absorption spectrum with improved methodologies agrees much better with the experiments than previous reported first-principles results. We also present a new development on the interface code bridging the BerkeleyGW code with an *ab initio* DFT code to enable GW-BSE calculations starting from DFT using metaGGA and hybrid exchange-correlation functionals.

To my parents and grandparents, Min Zhu, Jie Zhao, Weimin Sun and Zhengben Zhu

For their endless love and support.

# Contents

**Contents** **ii**

**List of Figures** **iv**

**List of Tables** **xvi**

**1 Introduction** **1**
1.1 Density functional theory . . . . . 1
1.2 Many-body theory of Green's functions . . . . . 4
1.3 GW approximation . . . . . 5
1.4 Bethe-Salpeter equation . . . . . 9

**2 Topological phases in graphene nanoribbons** **12**
2.1 Introduction . . . . . 12
2.2 Topological classification in quasi-1D systems . . . . . 13
2.3 Topological phases in armchair graphene nanoribbons . . . . . 15
2.4 Topological phases in graphene nanoribbons of other edge geometries: chevron and cove-edged graphene nanoribbons . . . . . 25
2.5 Topological phases in graphene nanoribbons tuned by electric fields . . 34
2.6 Topological band engineering in graphene nanoribbon superlattices . . 49
2.7 Conclusion . . . . . 51

**3 Bulk-edge correspondence in $Z_2$ classification in quasi-1D systems** **52**
3.1 Introduction . . . . . 52
3.2 Bulk-edge correspondence and $Z_2$ classification in a real GNR system . 52
3.3 Violation of bulk-edge correspondence in some gaps in $Z_2$ classification of (quasi-) 1D systems . . . . . 53

**4 Substrate interaction in boron-doped graphene nanoribbons** **61**
4.1 Introduction . . . . . 61
4.2 Strong substrate interaction in boron-dimer-doped armchair graphene nanoribbons . . . . . 61

**5 Designing of graphene nanoribbon double-quantum-well transistor** **75**

5.1 Introduction . . . . . 75
5.2 Double-quantum-well transistor . . . . . 76
5.3 Lineshape of a quantum well state coupled to metallic leads . . . . . 77
5.4 Lineshape of a quantum well state coupled to metallic leads with finite band width . . . . . 79

**6 Optical properties of crystalline conjugated polymers 84**
6.1 Introduction . . . . . 84
6.2 Optical excitations in poly(p-phenylene vinylene) polymer crystals . . . 84
6.3 Development for the interface code between Quantum ESPRESSO and BerkeleyGW . . . . . 97

**Bibliography 102**

# List of Figures

1.1 The calculated absorption spectra for silicon by the interband transition method with the GW band structure (black dashed) and the GW-BSE (red solid) method which includes electron-hole interactions using the BerkeleyGW package [31]. The dotted line is experimental data from [54]. The figure is taken from Ref. [31]. . . . . 11

2.1 Schematic structure of AGNRs with N rows of carbon atoms. The carbon-carbon bonds and carbon-hydrogen bonds are colored black and gray, respectively. The black numbers on the left label the row number of carbon atoms of the AGNR. The red numbers labels the carbon atom in a unit cell. The red dashed line denotes a unit cell of the AGNR. The red arrows are lattice vectors of graphene. . . . . 17

2.2 Brillouin zone and high symmetry points of graphene. The dashed lines show the specific k path of which the wavefunctions of graphene constitute the $n$-th band of an N-AGNR. . . . . 18

2.3 Heterojunctions formed with N = 9 and N = 7 armchair graphene nanoribbons (9AGNR/7AGNR) between two (a) topologically equivalent segments and (b) topologically inequivalent segments. The red dashed line denotes the interface between the two nanoribbons. The carbon-carbon and carbon-hydrogen bonds are colored black and gray, respectively. The color scale shows the charge density of the localized midgap junction state. The charge density is integrated along the out-of-plane direction [in units of $1/(a.u.)^2$ ]. 22

2.4 Boron-doped graphene nanoribbons. (a) Structure of an N = 7 AGNR periodically doped with boron pairs (B2-7AGNR). The carbon-carbon, carbon-boron, and carbon-hydrogen bonds are colored black, red, and gray, respectively. The dashed black rectangle indicates a unit cell. (b) Band structure of the B2-7AGNR calculated with the *ab initio* GW method. The top of the valence band is set at 0 eV. (c) Wave function of dopant orbitals with $s$ and $p$ symmetries, plotted at 1 Angstrom above the nanoribbon plane. The red and blue color shows positive and negative amplitudes [in units of $1/(a.u.)^{(3/2)}$ ]. . . . . 23

2.5 Doped-pristine AGNR superlattice. (a) Structure of a 7AGNR/B2-7AGNR superlattice. The carbon-carbon, carbon-boron, and carbon-hydrogen bonds are colored black, red, and gray, respectively. The color scale shows the charge density distribution of the lower junction-state band integrated over states in the superlattice BZ and integrated over the direction perpendicular to the ribbon plane [in units of $1/(a.u.)^2$ ]. (b) Schematics of the 1D antiferromagnetic Heisenberg spin 1=2 chain corresponding to the system shown in (a). The arrows denote relative directions of electron spins. (c) *Ab initio* calculated exchange parameters in the Heisenberg model as a function of the separation distance, in log scale and linear scale (inset). . . . . 24

2.6 Schematic structures (top panels) and band structures calculated using DFT-LSDA (bottom panels) of short period cove-edged GNRs of (a) N = 5 (odd), (b) N = 6 (even) with symmetric edges (aligned facing vacancies), and (c) N = 6 (even) with asymmetric edges (misaligned facing vacancies) across the ribbon. The cove-edged GNRs are periodic along the x direction, and the side view in (a) illustrates the structural deformation along the direction perpendicular to the GNR plane. The unit cell of each GNR studied is shown by the black bracket. The gray and silver balls denote carbon and hydrogen atoms, respectively. The pink and blue areas denote edge carbon rings tilting upward and downward from the ribbon plane, respectively. (d) DFT-LSDA band gap of the three types of cove-edged GNRs in (a)-(c). For N = asymmetric-even cove-edged GNRs, the DFT-LSDA band gap is close to 0. (e) Wannier centers of the $\pi$-electron Wannier functions of an N = 5 cove-edged GNR are denoted by red dots in the unit cell. . . . . 28

2.7 Schematic structures (top) and DFT-LDA band structures (bottom) of (a) regular chevron, (b) extended-chevron, and (c) binaphthylchevron GNRs. Gray and silver balls denote carbon and hydrogen atoms, respectively. The structures of extended- and binaphthyl-chevron GNRs are laterally extensions of a regular chevron GNR with additional hexagonal carbon rings (blue) and additional two rows of carbon (orange) in the elbow positions, respectively. They all have the narrowest width portions in the unit cell formed from N = 6 armchair GNR. The green and purple brackets show the unit cell shapes corresponding to topologically trivial and nontrivial phases ( $Z_2 = 0$ and 1), respectively. The DFT-LDA band structures show a semiconducting gap of 1.59, 1.37, and 1.18 eV in regular chevron, extended-chevron, and binaphthyl-chevron GNRs, respectively. . . . . 31

2.8 GNR heterojunctions formed with (a) an N = 7 AGNR and an N = 5 cove-edged GNR (finite length of 7.94 nm), and (b) an N = 7 AGNR and a regular chevron GNR (superlattice with lattice constant a = 10.23 nm). The upper panel and lower panel in (a) and (b) show heterojunctions between two topologically equivalent segments (zigzag/zigzag interface) and inequivalent segments (zigzag'/zigzag interface), respectively. These are zoom-in schematic structures near the junctions. The gray and silver balls represent the carbon and hydrogen atoms, and the green (purple) brackets show the unit cell with $Z_2 = 0$ (1). The color scale shows the square of wave function of the topological junction states integrated over the direction perpendicular to the ribbon plane [in units of $1/(a.u.)^2$ ]. The density of states of (c) the N = 7 AGNR/N = 5 cove-edged GNR heterojunctions and (d) the N = 7 AGNR/chevron GNR heterojunctions, with zigzag/zigzag (red curves) and zigzag'/zigzag (blue curves) interfaces, where a broadening of 0.03 eV is used. Topologically induced junction states emerge at the zigzag'/zigzag interfaces. . . . . 32

2.9 Finite GNR segments with different end terminations for (a) an N = 5 cove-edged GNR (a finite length of 6.21 nm) and (b) a regular chevron GNR (a finite length of 6.67 nm). Both isolated GNR segments consist of one end with $Z_2 = 1$ and the other end with $Z_2 = 0$. The gray and silver balls represent the carbon and hydrogen atoms, respectively, and the green (purple) bracket shows the unit cell with $Z_2 = 0$ (1) at a particular end. The color scale shows the charge density of the topologically induced end state at the end with $Z_2 = 1$. The charge density of the end state is integrated over the out-of-plane direction [in units of $1/(a.u.)^2$ ]. The density of states from DFT-LDA calculation of (c) cove-edged GNR segment and (d) chevron GNR segment with structures shown in (a) and (b) respectively are plotted, where an energy broadening of 0.03 eV is used. A 2-fold degenerate topologically induced end level appears at midgap (or at the Fermi level since it is half occupied) for both GNR segments. . . . . 33

2.10 (a) A unit cell of the B&N-11AGNR (commensurate with a zigzag end termination). The blue arrow shows the direction of a positive TEF. The red dashed line shows a mirror plane of the system, and the blue dashed line defines a normal plane about which the positions of the boron- and nitrogen-dimers are switched upon reflection. (b, c) The BCB wavefunction (b) and TVB wavefunction (c) at the Γ point on a plane at 1 Angstrom above the GNR basal plane. (d) The B&N-11AGNR band structure without any applied field. The blue, red and green colors in the band structure denote the module squared weights of the wavefunction that are projected onto the boron, nitrogen and carbon atomic orbitals, respectively. The scale bar defines the mapping between the color scale and the percentage weight. The projection is normalized according to the total number of atoms of each species per unit cell. The parity eigenvalues $\langle\psi_{n\Gamma_i}|\,\hat{M}\,|\psi_{n\Gamma_i}\rangle$ of the 8 bands near the Fermi level $E_F$ at Γ and $X$ are marked as "+" ("-") for value of +1 (-1). . . . . 36

2.11 The band inversion process under changing TEFs from DFT-LDA calculations. As the TEF goes below a critical field strength of $E_c \sim -0.2$ V/nm, the characters (and parities) of the states of the BCB and TVB at the $X$ point are inverted, and both the $Z$ and $Z_2$ invariants of this system change from 1 to 0. The bands are zoomed in a region near the $X$ point in reciprocal space spanning over 1/10 of the $\Gamma - X$ length. . . . . 37

2.12 Bulk-edge correspondence. (a-c) The red curves show the calculated end-cell LDOS (integrated in the red rectangular region in (d)) of the 24-unit-cell finite-length GNR with TEF of E = 1.09 (a), 0 (b), and -1.09 (c) V/nm, while the blue curves show the bulk DOS per unit cell at the same TEFs. Both the LDOS and DOS are in units of number of states per energy per length without considering spin degeneracy. The Gaussian broadening factor is 1 meV for both the LDOS and bulk DOS. The insets zoom in the green dashed rectangular regions. (d) The iso-surface charge density plot at $1.4\times10^{-5}$ Å$^{-3}$ (1% of the maximum value) of the topological end state in the 24-unit-cell finite segment (only the left 1/3 of the segment is shown). The TEF is 1.09 V/nm ($Z = 1$). (e) DFT-LDA bandgap versus TEF calculated using the SIESTA package ($E_c \sim -0.8$ V/nm). The calculated $Z$ invariant is 1 (0) for $E > E_c$ ($E < E_c$). The colors on different parts of the curve denote the number of end states per end for the system. . . . . 39

2.13 (a) The TEF profile in one repeating period as a function of coordinate x which is along the axis of the ribbon. (b) The iso-surface charge density plot at $2.7 \times 10^{-6}$ Å$^{-3}$ ( 2% of the maximum value) of the topological junction state (evaluated at Γ-point of the superlattice) of a B&N-11AGNR with the superlattice electric field in (a) applied. One repeating period of the TEF (the supercell shown in (b)) contains 24 B&N-11AGNR unit cells. The field strengths in the center of the left (right) region are -1.58 V/nm (0 V/nm) resulting in the system with $Z$ being 0 (1). (c) DOS of the GNR in a superlattice electric field. The red solid curve shows the LDOS computed in the junction region (the red rectangle in (b)). The green (blue) dashed curves show the bulk DOS per unit cell with a uniform TEF of E = -1.58 V/nm (0 V/nm). . . . . 40
2.14 A and B sublattice in pristine and co-doped AGNR systems. In both (a) and (b), the atoms (carbon, boron or nitrogen) circled by blue and orange circles belong to A and B sublattices, respectively. (a) A pristine 11AGNR. (b) A B&N-11AGNR. The blue dashed line defines a normal plane about which the positions of the boron- and nitrogen-dimers are switched upon reflection. . . . . 44
2.15 Calculation of Z index or winding number using the simplified tight-binding model. The parity eigenvalues $\langle\psi_{n\Gamma_i}|\,\hat{M}\,|\psi_{n\Gamma_i}\rangle$ of the high symmetry points are marked as "+" and "-" for value +1 and -1, respectively. (a) The band structure within the tight-binding model ($\epsilon_B = -\epsilon_N = 7.2$ eV,t=-2.7 eV). The blue, red and green colors in the band structure denote the module squared weight of the wavefunction that is projected onto boron, nitrogen, and carbon atomic orbitals, respectively. The projection has been normalized according to the total number of atoms of each species per unit cell. The scale bar defines the mapping between the color scale and the percentage weight. (b-d) The band inversion process in the simplified tight-binding model. The bands are plotted near the $X$ point in a reciprocal space spanning over 1/10 of the $\Gamma - X$ length. (e-f) The real and imaginary part of $det(h(k))$ as k moves across the 1D BZ. The red (green) curve shows the trajectory of $det(h(k))$ in the complex plane corresponding to $k$ going from Γ to $X$ (from $X$ back to Γ), with the arrow showing the direction. The windings of $det(h(k))$ in the complex plane around the origin with the TEF above (e) and below (f, g) $E_c$ are 1 and 0, respectively, corresponding to $Z = 1$ and $Z = 0$. . . . . 45
2.16 The positions of center of the MLWFs of B&N-11AGNR obtained from DFT calculations using the SIESTA package. The radius of the blue dots is proportional to the spread of the WFs. The numbers on each dot denote the onsite energy in the WF basis, while (a) is for the Kohn-Sham Hamiltonian and (b) is for the mapped chiral Hamiltonian. The blue dashed line in (b) is the normal plane about which the atomic sites switch positions upon reflection although the species of the atoms may not be the same. . . . . 46

2.17 (Continued from Fig. 2.16) (c-f). The band structure of the mapped chiral system (colored line) and the Kohn-Sham system (grey line). The blue, red and green colors denote the module squared weight of the wavefunction that is projected onto WFs on boron, nitrogen and carbon atoms. The projection has been normalized according to the total number of WFs of each atom species per unit cell. The scale bar defines the mapping between the color scale and the percentage weight. (c) shows the band structure in the absence of applied field. (d-f) is the zoom-in band structure near the X point (spanning over 1/5 of the $\Gamma - X$ length) where the field-induced band inversion happens. Depicted are the band structures for E = 1.09 V/nm (d), -1.09 V/nm (e) and - 3.27 V/nm (f), which correspond to $E > E_c$ (d), $E_s < E < E_c$ (e) and $E < E_s$ (f), respectively. (g-i) The winding of the value of $det(h(k))$ of the mapped chiral Hamiltonian around the origin in the complex plane, corresponding to the case where E = 1.09 V/nm (g), -1.09 V/nm (h) and -3.27 V/nm (i). The red (green) curve shows the trajectory of $det(h(k))$ in the complex plane corresponding to $k$ going from $\Gamma$ to $X$ (from $X$ back to $\Gamma$), with the arrow showing the direction. . . . . 47

2.18 Electronic structure of 7/9-AGNR superlattice. (a) Inset, STM topography of 7/9-AGNR superlattice ($V_s$ = –0.10 V, $I_t$ = 80 pA). The red (blue) curve shows dI/dV point spectroscopy data collected on the 7-AGNR (9-AGNR) segment (tip position marked by plus sign). The dotted black curve shows a spectrum collected on bare Au(111). The spectroscopy parameters are $V_{ac}$ = 10 mV and f = 581 Hz. (b) Constantcurrent dI/dV maps obtained at voltages corresponding to peaks A, B, C and D marked by arrows in a ($I_t$ = 100 pA, $V_{ac}$ = 10 mV, f = 581 Hz). (c) LDOS maps calculated via DFT at the energies of the 7/9-AGNR superlattice VB, OTB, UTB and CB marked by arrows in (d) (obtained 4 Åabove the GNR plane). (d) Calculated DOS obtained via DFT for the 7/9AGNR superlattice (0.05 eV Gaussian broadening used). All STM data shown here were obtained at T = 4K on a 7/9-AGNR consisting of 12 fused monomer units (the total GNR length was 15.6 nm). . . . . 50

2.19 Topological bands in 7/9-AGNR superlattice. (a) Wireframe sketch of the 7/9-AGNR superlattice with superimposed charge density for only a single, isolated interface state. Arrows represent hopping amplitudes that couple interface states through different AGNR segments. (b) DFT–LDA wavefunctions for the OTB maximum and UTB minimum are composed of bonding and antibonding linear combinations of adjacent interface-state wavefunctions. The wavefunctions are plotted in the plane 1 Å above the GNR atomic plane to demonstrate bonding symmetry. (c) Solid black curves show the DFT-LDA band structure of a freestanding 7/9-AGNR superlattice. The dashed red curve shows a tight-binding fit to DFT OTB and UTB using equation 2.39. . . . . 51

3.1 Bulk-edge correspondence violation in a practical GNR system. (a) A unit cell of the B&N-11AGNR (commensurate with a zigzag end termination). The red dashed line shows a mirror plane of the system. (b) The iso-surface charge density plot at $1.4 \times 10^{-5)}$ Å$^{-3}$ (1% of the maximum value) of the topological end state in the 24-unit-cell finite segment (only the left 1/3 of the segment is shown). (c) The red curves show the calculated end-cell LDOS (integrated in the red rectangular region in (b)) of the 24-unit-cell finite-length GNR, while the blue curves show the bulk DOS per unit cell. Both the LDOS and DOS are in units of number of states per energy per length without considering spin degeneracy. The Gaussian broadening factor is 1 meV for both the LDOS and bulk DOS. The insets zoom in the green dashed rectangular regions. (d) The B&N-11AGNR band structure without any applied field. The parity eigenvalues $\langle\psi_{n\Gamma_i}|\,\hat{M}\,|\psi_{n\Gamma_i}\rangle$ of the 8 bands near the Fermi level $E_F$ at $\Gamma$ and $X$ are marked as "+" ("-") for value of +1 (-1). . . . . 54

3.2 Bulk-edge correspondence violation in a 4-band system. (a) A tight binding model showing the tendency of a 4-band system towards being separated into two subsystems. (b) The band structure of the 4-band system with c. The the bands with blue and green shades are trivial and nontrivial bands, respectively. (c) The band edge that defines gap 3 and the end state in gap 3 in a semi-infinite chain as a function of the interchain coupling $|s_1|$. As $|s_1|$ goes below the critical value $s_c \sim 1.703$ eV, the end state merges into the bulk continuum and thus the bulk-edge correspondence is violated. . . 57

3.3 Bulk-edge correspondence (BEC) violation in a modified SSH model. (a) A SSH model with second- and third-nearest-neighbor hopping. (b) The phase diagram in the ($\frac{|t_2|}{|t_1|}$ , $\frac{|s_2|}{|t_1|}$ ) parameter plane, showing the bulk edge correspondence holds when only nearest-neighbor and second-nearest-neighbor hopping are present. (c, d) The phase diagram in the ( $\frac{s_3^1}{|t_1|}$, $\frac{s_2}{|t_1|}$ ) parameter plane. The red, blue, and grey region in the phase diagram denotes the regime where the bulk edge correspondence is violated, the regime where the bulk edge correspondence holds, and the regime where the system is gapless, respectively. (c) The phase diagram with $\frac{|t_2|}{|t_1|} = 0.9$ fixed. The $Z_2$ invariant of the system in the nonzero gap regime is 0. (d) The phase diagram with $\frac{|t_2|}{|t_1|} = 1.1$ fixed. The $Z_2$ invariant of the system in the nonzero gap regime is 1. . . . . 59

4.1 Band structure evolution of freestanding boron-dimer-doped N = 7 armchair graphene nanoribbons (AGNRs) at different dopant densities. Unit cells of (a) undoped, (b) dilute-doped, and (c) densely doped N = 7 GNRs. (d-f) Corresponding band structures calculated by DFT within LDA. The relative Brillouin zone sizes in panels d, e, f are 9 : 1 : 3, and when this is taken into account, the dispersion of the VB top and CB bottom does not change significantly after doping. . . . . 63
4.2 (a) The unit cell for a freestanding dilute boron-dimer-doped 7AGNR. Red, black, and purple spheres represent boron, carbon, and hydrogen atoms, respectively. (b, c) Calculated wavefunctions of the two dopant states at the Γ point for a freestanding GNR. The wavefunctions are plotted along the axial line of the unit cell in (a) (black dashed line) 1 Å above the GNR. 64
4.3 Band structures of freestanding boron-dimer-doped N=7 AGNR at two intermediate dopant concentrations. (a, b) Unit cells of freestanding N=7 AGNRs at two intermediate dopant concentrations 1 and 2, respectively. (c, d) Corresponding band structures calculated by DFT. The band gap for Intermediate 1 is 40 meV, and for Intermediate 2 is 230 meV. . . . . 65
4.4 Electronic structure of a dilute boron-dimer-doped N = 7 AGNR on Au(111). (a) Wireframe sketch of a dilute-doped GNR. (b) STM topographic image of dilute-doped GNR ($V_s = -0.4$ V, $I_t = 60$ pA). (c) STM dI/dV spectroscopy measurement taken at the edge of an undoped segment of the GNR (green). Top inset shows dI/dV spectroscopy taken at the center of a boron dimer segment (blue) compared to the center of an undoped GNR segment (black). Bottom inset shows dI/dV spectroscopy taken at the edge of a boron-dimer-doped segment (red) compared to the edge of an undoped GNR segment (green). Two new states, dopant States 1 and 2, are observed at -0.52 and 0.8 eV, respectively. dI/dV maps of the GNR are shown at energies corresponding to (d) the CB edge ($V_s = 1.68$ V), (e) State 2 ($V_s = 0.8$ V), (f) State 1 ($V_s = -0.52$ V), and (g) the VB edge (the fact that the VB feature on the left side is darker is due to the asymmetrical defect placement, which likely increases quantum confinement effects on the left side) ($V_s = -0.8$ V). T = 7 K for all measurements. Panels d-g have the same scale as panel b. . . . . 66
4.5 Electronic structure of densely boron-dimer-doped N = 7 AGNR on Au(111). (a) Wireframe sketch of a densely doped GNR. (b) STM topograph parameters: $V_s = 1.60$ V, $I_t = 20$ pA. (c) STM dI/dV spectroscopy measured at the edge and center of a densely doped GNR as shown in panel b. (d) dI/dV map taken at $V_s = 1.60$ V visualizes state at the CB edge. (e) dI/dV map taken at $V_s = 1.0$ V visualizes unoccupied dopant-induced state (State B). (f) dI/dV map taken at $V_s = -0.23$ V visualizes occupied dopant-induced state (State A). T = 4.5 K for all measurements. Panels d-f have the same scale as panel b. . . . . 67

4.6 DFT-LDA calculation of dilute-doped N = 7 GNR on Au(111) substrate. (a) Calculated LDOS 4 Åabove the boron-dimer-doped segment shows dopant States 1 and 2 (theoretical LDOS is broadened by a Gaussian function with standard deviation $\sigma$ = 125 meV). Calculated LDOS map is shown for (b) E = 0.38 eV (integrated over a 0.05 eV energy window) and (c) E = -0.21 eV (integrated over a 0.05 eV energy window). (d) Side-view and top-view of the supercell and the relaxed structure used to calculate the dilute-doped GNR. The supercell includes four layers of Au atoms. Red dashed line shows the surface upon which the LDOS maps are calculated. (e) Calculated wave function along the dashed line in panel b for E = 0.38 eV. (f) Calculated wave function along the dashed line in panel c for E = -0.21 eV. Panels b and c have the same scale. . . . . 71

4.7 DFT-LDA calculation of densely doped N = 7 GNR on Au(111) substrate. (a) Calculated LDOS 4 Åabove boron-dimer-doped segment shows dopant States A and B (theoretical LDOS is broadened by a Gaussian function with standard deviation $\sigma$ = 125 meV). (b) Wireframe sketch shows location of boron dimers. Calculated LDOS maps (each including four boron dimers) are shown for (c) E = 0.35 eV (integrated over a 0.05 eV energy window) and (d) E = -0.22 eV (integrated over a 0.05 eV energy window). (e) Side view and top view of the supercell and the relaxed structure (includes four layers of Au atoms) used to calculate the relaxed densely doped GNR. The red dashed line shows the surface upon which the LDOS maps are calculated. Panels c and d have the same scale. . . . . 72

4.8 Calculated wavefunctions of densely-doped AGNRs. Wavefunctions of States A and B of the densely-doped GNR, (a, b) Calculated LDOS maps of States A and B for the densely-doped AGNR. (c) Calculated wavefunction along the dashed line in (a) at E = 0.35 eV shows the *s*-like symmetry nature of State B. (d) Calculated wavefunction along the dashed line in (b) at E = - 0.22 eV exhibits a node (i.e., the wavefunction crosses the x-axis) which indicates the *p*-like symmetry of State A. (a) and (b) have the same scale. 74

5.1 The schematic configuration of a double-quantum-well transistor. The leads part are made of metallic zigzag GNRs, the barrier parts are made of N=7 AGNRs with $\sim$ 3.8 eV quasiparticle gap, and the quantum dot part are made of deformed N=11 AGNRs with smaller band gap than the barrier part. The dangling bands at the edge the GNR structure should be capped by hydrogen atoms. (b) The band diagram of the double-quantum-well transistor. The orange curve shows the Fermi-Dirac filling in the metallic GNR leads and the density of states of the isolated quantum energy levels in the quantum dots. (c) The band diagram of a typical field effect transistor. 77

5.2 (a) The structure of a quantum well made by N=11 armchair GNR coupled to metallic leads made by nitrogen doped armchair GNR. The barrier is made of N=7 armchair GNR. (b) The calculated quantum conductance $T(E)$ of the system as a function of bias voltage, plotted in logarithm scale. The orange curve is a Lorentzian profile fitted to the peak marked by "1". 80
5.3 The model system of a quantum dot (Q-dot) coupled to a metallic leads with a finite band width. The interaction between the metallic chain and the Q-dot is described by the hopping between the end atom in the metallic chain and the Q-dot, $s$. The hoppings between adjacent atoms in the metallic chain is $t$. . . . . 81
5.4 (a) The local density of states of the quantum well coupled to a narrow band metal. (b) The logarithm of the local density in (a). (c) The configuration of double-quantum-well with quantum dots (Q-dots) coupled to metallic wires with finite band widths. The blue curve and the gray curve are the logarithm of the local density of states on the left Q-dot and right Q-dot, respectively. The horizontal axis is logarithm of density of states while the vertical axis is the dimensionless energy x. It shows the case where the energy level of the two Q-dots are not aligned (off-state). The peak positions of the LDOS of the Q-dots could be tuned by the gate voltage to be aligned (on-state). . . . . 82

6.1 The measured absorption spectrum of crystalline PPV. The data is taken from Ref. [42]. . . . . 85
6.2 Calculated optical absorption spectrum of PPV in arbitrary units. The solid (dashed) lines denote spectra including (neglecting) electron-hole interaction. The polarization vector of the electric field is along the polymer chain. The figure includes an artificial broadening of 0.05 eV. The figure is taken from Ref. [92]. . . . . 86
6.3 Structural optimization of the crystalline PPV. (a) The orthorhombic unit cell of the crystalline PPV determined by experiments. The lattice constants in the three directions a, b, and c are 6.05, 7.90, 6.58 Å, respectively. The angle between the two non-perpendicular axis, $a$ and $c$, is 57 degrees. (b) The definition of the setting angle: the angle between the molecular plane of one PPV chain and the plane defined by axis $a$ and $c$. (c) The definition of the layer shift between the two PPV chains inside one unit cell: the length of the shift vector divided by the lattice constant in the direction defined by $c$. (d) The relative total energy per unit cell as a function of the layer shift. The global (local) minimum is located at layer shift = 0.18 (0.5). . 87
6.4 The quasiparticle band gap as a function of iteration number $n$ in $G_nW_0$ calculations for structure with layer shift being 0.5. We stop at the $G_3W_0$ level at which the self-consistency is reached. The $GW_0$ gap is 2.2 eV, which is about 10 % larger than the $G_0W_0$ gap. . . . . 89

6.5 Quasiparticle band structure of a crystalline PPV with layer shift = 0.5. The red solid line and black dashed line show the $GW_0$ band structure and the DFT-LDA band structure, respectively. The first and second set of valence bands (conduction bands) are marked VB1 and VB2 (CB1 and CB2), respectively. One set contains two bands due to two PPV chains inside one unit cell. The first (second) set of conduction bands and valence bands are mostly contributed from the extended state located at the carbon-carbon double bounds (narrow-band states localized at the benzene rings). 90
6.6 The contour map plot of the absolute value of the wavefunction at Y point. The wavefunction is plotted at a plane 1 Å above the PPV chain molecular plane. . . . . 91
6.7 Quasiparticle band structure of crystalline PPV with layer shift = 0.18. (a) The red solid line and black dashed line show the GW0 band structure and the DFT-LDA band structure, respectively. The first and second set of valence bands (conduction bands) are marked VB1 and VB2 (CB1 and CB2), respectively. One set contains two bands due to two PPV chains inside one unit cell. The first (second) set of conduction bands and valence bands are mostly contributed from the extended state located at the carbon-carbon double bounds (narrow-band states localized at the benzene rings). 92
6.8 Blue line: calculated absorption spectrum for the crystalline PPV with layer shift parameter = 0.5 by GW-BSE starting from DFT-LDA. Black line: the measured absorption spectra on the crystalline PPV sample with chain length of $\sim$ 90 Å(data taken from Ref. [42] ). The three major peaks are indicated by red, green and black arrows. The measured spectra are in arbitrary unit (not to the same scale marked on the vertical axis). A 0.2 eV Gaussian broadening is used in the calculated absorption spectrum. . . 93
6.9 The $GW_0$ quasiparticle band structure showing the transitions contributing to the three major peaks in Fig. 6.8. . . . . 94
6.10 The measured absorption spectra on the crystalline sample with a chain length of $\sim$ 50 Å(red line), $\sim$ 70 Å(green line), and $\sim$ 90 Å(black line) (data taken from Ref. [42] ). The absorbance curve for different samples are not plotted to the same scale. . . . . 95
6.11 Blue line: The calculated absorption spectrum of crystalline PPV with layer shift parameter being 0.5. Black line: the measured absorption spectra on the crystalline PPV sample with chain length of $\sim$ 90 Å(data taken from Ref. [42] ). The calculation solves the full BSE without the TDA. The measured spectra are plotted using an arbitrary unit (not to the same scale marked on the vertical axis). A 0.2 eV Gaussian broadening is used in the calculated absorption spectrum. . . . . 96

6.12 GW-BSE calculation starting from DFT using different exchange-correlation functionals. The GW-BSE absorption spectra calculated starting from SCAN and LDA exchange-correlation functionals (compared with the measured absorption spectra). The measured spectra are plotted using an arbitrary unit (not to the same scale marked on the vertical axis). A 0.2 eV Gaussian broadening is used in the calculated absorption spectra. . . . . 99

# List of Tables

2.1 Categorization of electronic topology of AGNRs. The nanoribbons are identified according to the type of termination (labeled in the first row) and width. Schematics of AGNR structure with different termination types is defined and plotted in the second row. The bracket denotes a specific termination of an infinitely long AGNR. The row number for the carbon atoms along the lateral direction are labeled from "1" to "N". The bulk unit cell of each structure that is commensurate with the termination is indicated by the dashed red rectangle. The bulk symmetry is indicated in the third row. The value of the $Z_2$ invariant is given in the fourth row. The floor function $\lfloor x \rfloor$ takes the largest integer less than or equal to a real number $x$. . . . . 21

2.2 Calculated values of $Z_2$ invariants of short-period cove-edged GNRs for different widths N (mod 8) and shape of the unit cells. Unit cell shapes studied are armchair, armchair', zigzag, zigzag', bearded, and bearded'. The atomic structure in the second row of the table is illustrated with an N = 5 cove-edged GNR, with gray and silver balls denoting carbon and hydrogen atoms, respectively. For N = odd, the unit cell boundary with a zigzag(') and bearded(') shapes forms a 60° and 120° angle with respect to the ribbon axis, respectively. For N = even, only the symmetric carbon vacancy structures which have sizable DFT-LSDA band gap are considered here. For unit cells with atomic structure that does not have spatial symmetry, the Zak phase is not quantized, so that a meaningful $Z_2$ invariant does not exist and this is denoted by "not applicable" (N/A). . . . . 29

6.1 The LDA gap, $G_0W_0$ gap, $GW_0$ gap, optical gap and exciton binding energy calculated for single chain and crystalline PPV with layer shift parameter being 0.18 and 0.5. [1] The 2.00 eV optical gap for single chain PPV is calculated from the $G_0W_0$ quasiparticle band structure. The binding energy $E_b$ for a single chain is defined as the $G_0W_0$ gap minus the optical gap because we did not calculate $GW_0$ gap for a single chain. The bindin energy $E_b$ for crystalline PPV is defined as the $GW_0$ gap minus the optical gap. . 92

6.2 GW-BSE calculation starting from DFT using different exchange-correlation functionals. (a) The calculated DFT gap, $GW_0$ gap and the "head" element of dielectric function $\epsilon_{0,0}(\boldsymbol{q})$ using LDA, PBE and SCAN functionals. $\boldsymbol{q}$ is the wavevector commensurate with the size of the envelope wavefunction of the exciton state with the highest oscillator strength in the first peak. . . 98
6.3 The DFT functionals and type of spin schemes supported by the *pw2bgw.x* interface code. Black: Supported type of DFT functionals and type of spin schemes before the development. Red: Newly supported type of DFT functionals and type of spin schemes after the development. . . . . 100

## Acknowledgments

First of all, I would like to heartfeltedly thank my advisor, Prof. Steven G. Louie. I felt so lucky to be admitted to UC Berkeley, one of the most renowned university for physic research, but the more lucky thing is to be your Ph.D. student and complete my doctoral study under your guidance. You are the greatest scientist I have ever met. You give the greatest patience to me, point out the mistakes I have made in my research, and let me correct the mistakes step by step. You could always ask the most precise question that hit the mark or find the problem when I present my results. Your objective and earnest altitudes towards scientific research facilitates me to get rid of the impetuosity in doing research. I have learnt so much during all the fruitful discussions with you. I learn not only physics, but also how to be a scientist from you.

I would also like to thank Mrs. Jane Louie for her warm and delicious annual Thanksgiving dinner. You and Prof. Louie gave me the feeling of home when studying abroad.

I would also like to thank all of my colleagues in the Louie group: Gabriel Antonius, Omar Ashour, Brad Barker, Ting Cao, Andrea Cepellotti, Yang-hao Chan, Sinisa Coh, Chen Hu, Jingwei Jiang, Felipe da Jornada, Sheng Ju, Yea-Lee Lee, Zhenglu Li, Mit Naik, Diana Qiu, Jiawei Ruan, Chin-Shen Ong, Weichen Tang, Meng Wu, Arica Chhay, and Maria Feng. And I also thank all my collaborators: Prof. Michael Crommie, Prof. Felix Fischer, Prof. Eli Yablonovitch, Chen Chen, Zahra Pedramrazi, Raymond Blackwell, Ilya Piskun.

I am also grateful to all my qualifying exam and dissertation committee members: Prof. Jeffery Neaton, Prof. Michael Crommie, and Prof. Felix Fischer. Thank you for pointing out the problems and deficiency during my qualifying exam talk, for being a great faculty mentor during my doctoral study, and for reading my dissertation.

Finally, I would like to thank my parents and grand parents, Min Zhu, Jie Zhao, Weimin Sun, and Zhengben Zhu. Your love is always my strength and trust to overcome the difficulties. I would also like to thank my cousin and her husband, Junjing Yan and Jun Ying. You had given me the feeling of home at Berkeley.

# Chapter 1

# Introduction

Here, we briefly review the theoretical and computational methods in condensed matter physics used in this thesis to obtain the electronics and optical properties of materials. Density functional theory (DFT) [56] is used for calculation of ground states properties of materials, and many-body perturbation theory from first principles, namely the GW approximation [50] and the GW plus Bethe-Salpeter equations (GW-BSE) method [91], are used to compute the excited states properties of materials involving injection of electron or holes, or both of them into the system, respectively.

## 1.1 Density functional theory

A solid contains periodically-arranged nuclei plus electrons that are either extended through the crystal or bounded to nuclei. The challenges to understand and describe the physical properties of solids arise in the large number of identical particles and complex interactions between the particles. The number of particles is in the order of Avogadro's number ($O(10^{23})$) , so it would be highly impossible to obtain an exact solution from microscopic theory describing the motion of each particles to understand the system. Moreover, the long-range Coulomb interaction, as the dominant interaction for particles in solids, induces complicated correlation effects between electrons.

The many-body Hamiltonian of all the electron and nuclei (in the non-relativistic limit and neglecting spin-orbit interaction) is as follows:

$$H_{tot} = T_e + T_i + V_{ii} + V_{ie} + V_{ee}, \tag{1.1}$$

where the kinetic energy of electron and nuclei are

$$T_e = \sum_i \frac{\boldsymbol{p}_i^2}{2m}, \tag{1.2}$$

$$T_j = \sum_j \frac{\boldsymbol{P}_j^2}{2M_j}. \tag{1.3}$$

The interaction between pairs of electrons $V_{ee}$, pairs of nuclei $V_{ii}$ and between an electron and a nucleus $V_{ei}$ are

$$V_{ee} = \sum_{i<i'} \frac{e^2}{|\boldsymbol{r}_i - \boldsymbol{r}_{i'}|}, \tag{1.4}$$

$$V_{ii} = \sum_{j<j'} \frac{Z_j Z_{j'} e^2}{|\boldsymbol{R}_j - \boldsymbol{R}_{j'}|}, \tag{1.5}$$

$$V_{ei} = \sum_{i,j} \frac{-Z_j e^2}{|\boldsymbol{R}_j - \boldsymbol{r}_i|}. \tag{1.6}$$

Here $\boldsymbol{p}_i$ and $\boldsymbol{r}_i$ denote the momentum and position of the $i^{th}$ electron, and $\boldsymbol{P}_j, \boldsymbol{R}_j, M_j$, and $Z_j$ denote the momentum, position, mass and charge of the $j^{th}$ nucleus.

### 1.1.1 Born-Oppenheimer Approximation

The first approximation we use to tackle the many-body problem is to assume that the position of the nuclei are fixed given the fact that the mass of the nuclei is roughly $10^4$ times larger than the electron mass. As a result, we decouple the Hamiltonian to write down an electronic Hamiltonian only in the subspace for electrons

$$H_e = \sum_i \frac{\boldsymbol{p}_i^2}{2m} + \sum_{i,j} \frac{-Z_j e^2}{|\boldsymbol{R}_j - \boldsymbol{r}_i|} + \sum_{i<i'} \frac{e^2}{|\boldsymbol{r}_i - \boldsymbol{r}_{i'}|}, \tag{1.7}$$

so we have a time independent eigenvalue equation for eigenstates of the electrons

$$H_e \Psi_e(\boldsymbol{r}_1, \boldsymbol{r}_2, ..., \boldsymbol{r}_N) = E \Psi_e(\boldsymbol{r}_1, \boldsymbol{r}_2, ..., \boldsymbol{r}_N). \tag{1.8}$$

We still have a many-body problem for electrons which involves $O(10^{23})$ variables and are almost impossible to solve exactly.

### 1.1.2 Kohn-Sham equations

Thanks to the Hohenberg-Kohn theorem [48], we have a rigorous formalism that any ground state properties of a system of many interacting electrons can be written as a functional of the ground state charge density $n(r)$. And the Kohn-Sham formalism [62] formulates the problem into a mean field equation that can be solved self-consistently to obtain the charge density.

The Kohn-Sham equation reads

$$H^{DFT} \psi_n(\boldsymbol{r}) = \left( -\frac{\hbar^2}{2m} + V_{ion}(\boldsymbol{r}) + V_H[n(\boldsymbol{r})] + v_{xc}[n(\boldsymbol{r})] \right) \psi_n(\boldsymbol{r}) = \epsilon_n \psi_n(\boldsymbol{r}), \tag{1.9}$$

which is the eigen equation for the wavefunction $\psi_n(\boldsymbol{r})$ and energy eigenvalue $\epsilon_n$ of $n^{th}$ non-interacting single electron orbit of an ficticious non-interacting electron system that would give the same density as the true interacting physical system.

After all the non-interacting electron wavefunctions are solved, one could calculate the ground state charge density

$$n(\boldsymbol{r}) = \sum_{n \in occ} |\psi_n(\boldsymbol{r})|^2, \tag{1.10}$$

where *occ* denotes all the occupied orbitals.

In the Kohn-Sham potential, $V_{ion}(\boldsymbol{r})$ denotes the potential generated by the periodically arranged ion cores in a solid, and the Hartree term is

$$V_H[n(\boldsymbol{r})] = e^2 \int d\boldsymbol{r}' \frac{n(\boldsymbol{r}')}{|\boldsymbol{r} - \boldsymbol{r}'|}. \tag{1.11}$$

The exchange-correlation potential $v_{xc}[n(r)]$ describes the effect from exchange interaction and correlation effect in the many-body electron system. The exchange-correlation potential is derived from the functional derivative of the total exchange-correlation energy $E_{xc}$

$$v_{xc}[n(r)] = \frac{\delta E_{xc}[n(\boldsymbol{r})]}{\delta n(\boldsymbol{r})}. \tag{1.12}$$

In general, if we know the exact form of this potential, the Kohn-Sham formalism is exact for ground state properties. However, the exact form of $v_{xc}[n(r)]$ is extremely hard to find, and the the earliest and still very popular approximation for it is the so-called local-density approximation (LDA) [82] , where $v_{xc}[n(\boldsymbol{r})]$ is taken to be only as a function of the local ground state charge density $n(\boldsymbol{r})$. The exchange-correlation functional is approximated as

$$E_{xc}[n(\boldsymbol{r})] \approx E_{xc}^{LDA}[n(\boldsymbol{r})] = \int d\boldsymbol{r} n(\boldsymbol{r}) \epsilon_{xc}(n(\boldsymbol{r})), \tag{1.13}$$

where $\epsilon_{xc}(n(\boldsymbol{r}))$ is the exchange-correlation energy per electron of a uniform electron gas with density $n(\boldsymbol{r})$ which may be obtained from quantum Monte Carlo simulations of uniform electron gas. This LDA works well when the charge density of the system is slow varying. For system with rapidly varying change density, an improvement over LDA is the generalized gradient approximation (GGA) [83].

$$E_{xc}^{GGA}[n(\boldsymbol{r})] = E_{xc}^{GGA}[n(\boldsymbol{r})] = \int d\boldsymbol{r} n(\boldsymbol{r}) \epsilon_{xc}(n(\boldsymbol{r}), \nabla n(\boldsymbol{r})). \tag{1.14}$$

The Kohn-Sham eigenvalues only describe the energy of the particles in the fictitious non-interacting system, which do not represent the quasiparticle excitation energies of the physical system. Hence, for example, the energy band gap of solids calculated by DFT is often underestimated.

Researchers further developed other approximations to imporve the exchange-correlation functional, for example, those involving higher order derivatives in the charge density $n(\boldsymbol{r})$, or those involving the kinetic energy density of the system $\tau(\boldsymbol{r})$ The latter one is called meta-GGA, and a type of meta-GGA, namely the strongly constrained and appropriately normed (SCAN) functional [104], has been producing good result for system with weak interactions such as hydrogen bonding.

$$E_{xc}^{SCAN}[n_\uparrow, n_\downarrow] = \int d\boldsymbol{r} n(\boldsymbol{r}) \epsilon_{xc}(n_\uparrow, n_\downarrow, \nabla n_\uparrow, \nabla n_\downarrow, \tau_\uparrow, \tau_\downarrow). \tag{1.15}$$

We will explore the usage of DFT calculations with SCAN functional and GW-BSE calculations in our study of optical properties of polymers in Chapter 6 .

## 1.2 Many-body theory of Green's functions

The Green's function formalism is a very powerful tool in describing many-body systems. It describes the behaviors of one particle, two particles, or several particles in a many-body interacting system, for which it is in general impossible to track each particle's behavior.

In a many-body systems of N identical particles, we can write the ground-state wavefunction as $|N\rangle$. If the system is in state with different number of particles, their wavefunctions are orthogonal to each other. We introduce the Fock's space, which use number of particles as a quantum number to separate the system into subspaces: $|N\rangle$, $|N-1\rangle$, $|N-2\rangle$ ... . Different subspaces are connected by the particle creation and annihilation operators denoted by $a$ and $a^\dagger$, respectively.

The interacting single-particle Green's function is defined as

$$G(\boldsymbol{r}, t; \boldsymbol{r}', t') = -i \left\langle N \right| T\psi(\boldsymbol{r}, t)\psi^\dagger(\boldsymbol{r}', t') \left| N \right\rangle, \tag{1.16}$$

where $T$ is the time-ordering operator, which keeps the field operator $\psi(\boldsymbol{r}, t)$ and $\psi^\dagger(\boldsymbol{r}', t')$ in a time order, from left to right, which means

$$T\psi(\boldsymbol{r}, t)\psi^\dagger(\boldsymbol{r}', t') = \begin{cases} \psi(\boldsymbol{r}, t)\psi^\dagger(\boldsymbol{r}', t') & (t > t') \\ \psi^\dagger(\boldsymbol{r}', t')\psi(\boldsymbol{r}, t) & (t < t') \end{cases}. \tag{1.17}$$

For $t > t'$ the Green's function describes the propagation of an additional electron injected at time $t'$, whereas for $t < t'$ it describes the propagation of a hole (extraction of an electron at time $t'$) .

We can write the Green's function in the Lehmann representation

$$G(\boldsymbol{r},t;\boldsymbol{r}',t') = -i\sum_s \langle N|\,\psi(\boldsymbol{r},t)\,|N+1,s\rangle\,\langle N+1,s|\,\psi^\dagger(\boldsymbol{r}',t')\,|N\rangle\,\Theta(t-t') \quad (1.18)$$

$$+i\sum_s \langle N|\,\psi^\dagger(\boldsymbol{r}',t')\,|N-1,s\rangle\,\langle N-1,s|\,\psi(\boldsymbol{r},t)\,|N\rangle\,\Theta(t'-t) \quad (1.19)$$

$$= -i\sum_s f_s(\boldsymbol{r}')f_s^*(\boldsymbol{r})exp(-i\epsilon_s\tau)(\Theta(\tau)\Theta(\epsilon_s-\mu)-\Theta(-\tau)\Theta(\mu-\epsilon_s). \quad (1.20)$$

Here we introduce the complete set of eigenstates of the many-body Hamiltonian for the $(N+1)$ or $(N-1)$ particles. The quantum labels of these states are denoted by $s$. $f_s(\boldsymbol{r})$ are overlap amplitudes for particle removal, that is, an occupied state (when $\epsilon_s < \mu$) or for particle injection, that is, an unoccupied state (when $\epsilon_s > \mu$). Here $\epsilon_s$ are the energy of the exact eigenstates of either the $(N+1)$ or $(N-1)$ particle system in reference to the $N$ particle ground state energy, and it is not rigorously equal to the quasiparticle energy which describes the effective energy of an excited state of a N particle system. Transforming it into the frequency space, we get the spectral representation:

$$G(\boldsymbol{r},\boldsymbol{r}',\omega) = \sum_s \frac{f_s(\boldsymbol{r})f_s^*(\boldsymbol{r})}{\omega-\epsilon_s\pm i\eta}, \quad (1.21)$$

where $\pm$ takes the $+$ for an unoccupied state and $-$ for an occupied state. The imaginary part of $G(\boldsymbol{r},\boldsymbol{r}',\omega)$ is defined as the spectral function $A(\boldsymbol{r},\boldsymbol{r}',\omega)$ .

$$A(\boldsymbol{r},\boldsymbol{r}',\omega) = \frac{1}{\pi}|ImG(\boldsymbol{r},\boldsymbol{r}',\omega)|. \quad (1.22)$$

The position of the poles of the spectral function gives the quasiparticle energies, and the equal position ($r = r'$) spectral function is related to the single-particle local density of states.

## 1.3 GW approximation

The electron-electron interaction could be considered as a perturbation on the non-interacting Hamiltonian for many materials. Solving the equation of motion for the single-particle Green's function with electron-electron interaction as a perturbation, we can get a Dyson's equation for the interacting single particle Green's function.

$$G(\boldsymbol{r},\boldsymbol{r}',\omega) = G_0(\boldsymbol{r},\boldsymbol{r}',\omega) + \int d\boldsymbol{r}_1 d\boldsymbol{r}_2 G_0(\boldsymbol{r},\boldsymbol{r}_1,\omega)\Sigma(\boldsymbol{r}_1,\boldsymbol{r}_2,\omega)G(\boldsymbol{r}_2,\boldsymbol{r}',\omega), \quad (1.23)$$

where $G_0$ and $G$ denote the non-interacting and interacting Green's function, respectively, and $\Sigma$ denotes a non-local and energy-dependent self-energy operator. The self-energy is the correction from a non-interacting particle energy to the interacting quasiparticle energy.

To solve for the self-energy of the many-body electron system, Hedin arrived at a set of self-consistent equations. [44, 45] The self-energy operator is expanded in terms of the interacting Green's function and the screened Coulomb interaction. The set of coupled integral equation is shown below, with the numbers denote the combined real-space position and time, e.g. $1 := (\boldsymbol{r}_1, t_1)$, $2^+ := (\boldsymbol{r}_2, t_2 + \delta)$ where $\delta$ is a positive infinitely small number.

$$\Sigma(12) = i \int W(1^+3)G(14)\Gamma(42;3)d(34), \tag{1.24}$$

$$W(12) = v(12) + \int W(13)P(34)v(42)d(34), \tag{1.25}$$

$$P(12) = -i \int G(23)G(42)\Gamma(34;1)d(34), \tag{1.26}$$

$$\Gamma(12;3) = \delta(12)\delta(13) + \int \frac{\delta\Sigma(12)}{\delta G(45)} G(46)G(75)\Gamma(67;3)d(4567), \tag{1.27}$$

where $W$ is the screened Coulomb interaction, $P$ is the irreducible polarizability, and $\Gamma$ is the vertex function.

Within the GW approximation, an important approximation on the vertex function $\Gamma$ is taken by letting $\Gamma(12;3) = \delta(12)\delta(13)$. This approximation omits the higher order terms of $W$ in the expansion of the self-energy $\Sigma$. This simplifies the equation and made the first-principles calculation of the self-energy feasible. The Hedin equation then reads

$$\Sigma(12) = iW(1^+2)G(12), \tag{1.28}$$

$$W(12) = v(12) + \int W(13)P(34)v(42)d(34), \tag{1.29}$$

$$P(12) = -iG(12)G(42)d(21). \tag{1.30}$$

As a result, the self-energy $\Sigma$ could be approximated by

$$\Sigma(\boldsymbol{r}, \boldsymbol{r}', \omega) = \frac{i}{2\pi} \int_{-\infty}^{\infty} d\omega' G(\boldsymbol{r}, \boldsymbol{r}', \omega - \omega')W(\boldsymbol{r}, \boldsymbol{r}', \omega')e^{i\delta\omega'}. \tag{1.31}$$

The screened Coulomb interaction is

$$W(\boldsymbol{r}, \boldsymbol{r}', \omega) = \int d\boldsymbol{r}'' \epsilon^{-1}(\boldsymbol{r}, \boldsymbol{r}'')v(\boldsymbol{r}'', \boldsymbol{r}'), \tag{1.32}$$

where $\epsilon^{-1}$ is the inverse of the dielectric function, and $v$ is the bare Coulomb interaction. The inverse of the dielectric function can be further evaluated from the irreducible polarizability

$$\epsilon^{-1}(\boldsymbol{r}, \boldsymbol{r}', \omega) = \delta(\boldsymbol{r}, \boldsymbol{r}') + \int d\boldsymbol{r}'' v(\boldsymbol{r}, \boldsymbol{r}'') P(\boldsymbol{r}'', \boldsymbol{r}', \omega). \tag{1.33}$$

The polarizability can be approximated to be a function of the non-interacting Green's function

$$P(\boldsymbol{r}, \boldsymbol{r}', \omega) = -\frac{i}{2\pi} \int d\omega' G_0(\boldsymbol{r}, \boldsymbol{r}', \omega') G_0(\boldsymbol{r}'', \boldsymbol{r}', \omega' - \omega). \tag{1.34}$$

### 1.3.1 First-principles GW calculations

The approximations above made the calculation of the self-energy and thus the quasiparticle band structures possible from first-principles calculations [51, 50]. The self-energy could be calculated from a starting mean field Hamiltonian given by the DFT Kohn-Sham equations. The energy levels and wavefunctions obtained by the DFT calculations are used as the energy eigenvalues and wavefunctions for the non-interacting Green's function. With the GW approximation to the self-energy, the Dyson equation leads to the quasiparticle equation below

$$\left(-\frac{\hbar^2}{2m} + V_{ion}(\boldsymbol{r}) + V_H[n(\boldsymbol{r})]\right) \psi_{n\boldsymbol{k}}(\boldsymbol{r}) + \int d\boldsymbol{r}' \Sigma(\boldsymbol{r}, \boldsymbol{r}', \epsilon^{GW}_{n\boldsymbol{k}}) \psi_{n\boldsymbol{k}}(\boldsymbol{r}') = \epsilon^{GW}_{n\boldsymbol{k}} \psi_n(\boldsymbol{r}). \tag{1.35}$$

Here we have made use of Bloch's theorem for crystals, where $\psi_{n\boldsymbol{k}}(\boldsymbol{r}) = e^{i\boldsymbol{k}\cdot\boldsymbol{r}} u_{n\boldsymbol{k}}(\boldsymbol{r})$ is the Bloch wavefunction for the solids, and $\boldsymbol{k}$ is the crystal momentum, a quantum number associated with the crystalline translational invariance.

In solving the quasiparticle equation, we first use the mean-field DFT results for the Green's function

$$G(\boldsymbol{r}, \boldsymbol{r}', \epsilon) = \sum_{n\boldsymbol{k}} \frac{\psi_{n\boldsymbol{k}}(\boldsymbol{r}) \psi^*_{n\boldsymbol{k}}(\boldsymbol{r}')}{\epsilon - \epsilon_{n\boldsymbol{k}} - i\delta_{n\boldsymbol{k}}}, \tag{1.36}$$

where $\delta_{n\boldsymbol{k}} = 0^+$ for $\epsilon_{n\boldsymbol{k}}$ below the Fermi level, and $\delta_{n\boldsymbol{k}} = 0^-$ for $\epsilon_{n\boldsymbol{k}} > \epsilon_F$ above the Fermi level. The irreducible polarizability is calculated from the DFT eigenfunctions and eigen energies [45, 31]:

$$P_{\boldsymbol{GG'}}(\boldsymbol{q};\omega) = \sum_{n}^{occ}\sum_{n'}^{emp}\sum_{\boldsymbol{k}} \langle\psi_{n',\boldsymbol{k}}|\, e^{-i(\boldsymbol{q}+\boldsymbol{G})\cdot\boldsymbol{r}}\, |\psi_{n,\boldsymbol{k}+\boldsymbol{q}}\rangle \langle\psi_{n,\boldsymbol{k}+\boldsymbol{q}}|\, e^{i(\boldsymbol{q}+\boldsymbol{G})\cdot\boldsymbol{r}}\, |\psi_{n',\boldsymbol{k}}\rangle \tag{1.37}$$

$$\left(\frac{1}{\omega - (E_{n,\boldsymbol{k}+\boldsymbol{q}} - E_{n',\boldsymbol{k}}) + i\delta} - \frac{1}{\omega + (E_{n,\boldsymbol{k}+\boldsymbol{q}} - E_{n',\boldsymbol{k}}) - i\delta}\right), \tag{1.38}$$

where *occ* denotes the occupied states, and *emp* denotes the empty states. The dielectric function is given by

$$\epsilon_{\boldsymbol{GG'}}(\boldsymbol{q};\omega) = \delta_{\boldsymbol{GG'}} - v(\boldsymbol{q}+\boldsymbol{G})P_{\boldsymbol{GG'}}(\boldsymbol{q};\omega), \tag{1.39}$$

where the bare Coulomb interaction $v(\boldsymbol{q}+\boldsymbol{G}) = \frac{4\pi e^2}{|\boldsymbol{q}+\boldsymbol{G}|^2}$. The screened Coulomb interaction is evaluated by

$$W_{\boldsymbol{GG'}}(\boldsymbol{q};\omega) = \epsilon^{-1}_{\boldsymbol{GG'}}(\boldsymbol{q};\omega)v(\boldsymbol{q}+\boldsymbol{G'}). \tag{1.40}$$

The self-energy for a quasiparticle state $|\psi_{n,\boldsymbol{k}}\rangle$ could be calculated using the Green's function and the screened Coulomb interaction by the equation

$$\langle\psi_{n,\boldsymbol{k}}|\, \Sigma(\boldsymbol{r},\boldsymbol{r'};\epsilon)\, |\psi_{n,\boldsymbol{k}}\rangle = \sum_{n'}\sum_{\boldsymbol{q},\boldsymbol{G},\boldsymbol{G'}} \langle\psi_{n,\boldsymbol{k}}|\, e^{i(\boldsymbol{q}+\boldsymbol{G})\cdot\boldsymbol{r}}\, |\psi_{n',\boldsymbol{k}-\boldsymbol{q}}\rangle \langle\psi_{n',\boldsymbol{k}-\boldsymbol{q}}|\, e^{-i(\boldsymbol{q}+\boldsymbol{G})\cdot\boldsymbol{r'}}\, |\psi_{n,\boldsymbol{k}}\rangle \tag{1.41}$$

$$\frac{i}{2\pi}\int d\epsilon' \frac{W_{\boldsymbol{GG'}}(\boldsymbol{q};\omega)}{\epsilon - E_{n',\boldsymbol{k}-\boldsymbol{q}} + i\delta_{n'\boldsymbol{k}-\boldsymbol{q}}}. \tag{1.42}$$

We note that the argument in the self-energy operator in Eqn. (1.35) is the quasiparticle energy level, so we need to solve a self-consistent equation to get the self-consistent value for the quasiparticle energy level $\epsilon^{GW}_{n\boldsymbol{k}}$

$$\epsilon^{GW}_{n\boldsymbol{k}} = \epsilon^{DFT}_{n\boldsymbol{k}} + \langle\psi_{n\boldsymbol{k}}|\, \Sigma(\epsilon^{GW}_{n\boldsymbol{k}}) - V_{xc}\, |\psi_{n\boldsymbol{k}}\rangle\,. \tag{1.43}$$

This could be solved by Newton's method iteratively [31].

The wavefunctions calculated by DFT could often be a very good approximation to the wavefunctions of quasiparticles, so in most of the system we do not need to update the wavefunctions to get better approximations to the quasiparticle wavefunctions, but one would do that for calculation of systems with significant wavefunction character change near small energy gaps of materials such as topological insulators.

## 1.4 Bethe-Salpeter equation

The optical absorption spectra provides extremely useful ways to investigate condensed matter systems. The theory of optical excitations will provide solid foundations in designing devices such as the light-emitting devices, laser technology and photovoltaics. Previously we have reviewed the GW approximation to calculate the quasiparticle properties in materials, and to investigate the optical excitations, we need to solve for the interacting two-particle Green's function which includes information regarding the interactions between two elementary excitations, the quasi electron states and quasi hole states. The quasi electron and quasi hole state will form correlated bound or resonant excitonic states through electron-hole interactions, and the excitonic states may be obtained through the Bethe-Salpeter equation [91]

$$L(1,2;1',2') = L_0(1,2;1',2') + \int d(3456) L_0(1,4;1',3) K(3,5;4,6) L(6,2;5,2'), \quad (1.44)$$

where $L$ is the electron-hole correlation function defined by the interacting two-particle Green's function $G_2$ and the interacting one-particle Green's function $G$

$$L(1,2;1',2') = -G_2(1,2;1',2') + G(1,1')G(2,2'), \quad (1.45)$$

$L_0$ is the free electron-hole state propagator

$$L_0(1,2;1',2',\omega) = i \sum_{v,c} \left[ \frac{\psi_c(\boldsymbol{r}_1)\psi_v^*(\boldsymbol{r}_1')\psi_v(\boldsymbol{r}_2)\psi_c^*(\boldsymbol{r}_2')}{\omega - (E_c - E_v)} - \frac{\psi_v(\boldsymbol{r}_1)\psi_c^*(\boldsymbol{r}_1')\psi_c(\boldsymbol{r}_2)\psi_v^*(\boldsymbol{r}_2')}{\omega + (E_c - E_v)} \right], \quad (1.46)$$

where the first term is the free electron-hole state excitation, and the second term is the free anti-electron-hole state excitation. On the other hand, the electron-hole correlation function $L$ is given by

$$L(1,2;1',2',\omega) = i \sum_{S} \left[ \frac{\chi_S(\boldsymbol{r}_1,\boldsymbol{r}_1')\chi_S^*(\boldsymbol{r}_2,\boldsymbol{r}_2')}{\omega - \Omega_S} - \frac{\chi_S(\boldsymbol{r}_2,\boldsymbol{r}_2')\chi_S^*(\boldsymbol{r}_1,\boldsymbol{r}_1')}{\omega + \Omega_S} \right], \quad (1.47)$$

where $\chi_S(\boldsymbol{r}_1,\boldsymbol{r}_1')$ denotes the electron-hole amplitude of a specific exciton state with index $S$ , and $\Omega_S$ is the corresponding excitation energy of the exciton state. The wavefunction of the exciton state is given by

$$\chi_S(\boldsymbol{r}_1,\boldsymbol{r}_1') = \sum_{v}^{occ} \sum_{c}^{emp} A_{vc}^S \psi_c(\boldsymbol{r}_1)\psi_v^*(\boldsymbol{r}_1') + B_{vc}^S \psi_v(\boldsymbol{r}_1)\psi_c^*(\boldsymbol{r}_1') \quad (1.48)$$

where $A^S_{vc}$ are the coefficients that correlate the free electron-hole pair excitations, and $B^S_{vc}$ are the coefficients that correlate the free anti- electron-hole pair excitations.

The exciton eigenstates $|S\rangle$ and eigenenergies $\Omega_S$ could be obtained by solving a BSE for $A$, where the wavefunction of states $\psi_c(\boldsymbol{r}_1)$ and $\psi_v(\boldsymbol{r}_1)$ are obtained from DFT, and $E_c - E_v$ uses the quasiparticle energy levels obtained from GW calculations. With the help of Eqn. (1.46 1.47 1.48), the BSE turns into a generalized eigenvalue problem for the coefficients $A^S_{vc}$ and $B^S_{vc}$ [91]

$$(E_c - E_v)A^S_{vc} + \sum_{v'c'} K^{AA}_{vc,v'c'}(\Omega_S)A^S_{v'c'} + \sum_{v'c'} K^{AB}_{vc,v'c'}(\Omega_S)B^S_{v'c'} = \Omega_S A^S_{vc}, \tag{1.49}$$

$$\sum_{v'c'} K^{BA}_{vc,v'c'}(\Omega_S)A^S_{v'c'} + (E_c - E_v)B^S_{vc} + \sum_{v'c'} K^{BB}_{vc,v'c'}(\Omega_S)B^S_{v'c'} = -\Omega_S B^S_{vc}, \tag{1.50}$$

where the matrix elements of the electron-hole interaction kernel $K$ are given by

$$K^{AA}_{vc,v'c'}(\Omega_S) = i\int d(3456)\psi_v(\boldsymbol{r}_4)\psi^*_c(\boldsymbol{r}_3)K(35,46;\Omega)\psi^*_{v'}(\boldsymbol{r}_5)\psi_{c'}(\boldsymbol{r}_6), \tag{1.51}$$

$$K^{AB}_{vc,v'c'}(\Omega_S) = i\int d(3456)\psi_v(\boldsymbol{r}_4)\psi^*_c(\boldsymbol{r}_3)K(35,46;\Omega)\psi^*_{v'}(\boldsymbol{r}_6)\psi_{c'}(\boldsymbol{r}_5), \tag{1.52}$$

and similiar expressions for $K^{BA}$ and $K^{BB}$.

For some systems, the off-diagonal blocks $K^{AB}$ and $K^{BA}$ are found to be small so that one can make the approximation to set $K^{AB} = K^{BA} = 0$, and this is known as the Tamm-Dancoff approximation [8, 33]. Therefore the BSE for the exciton amplitute $A^S_{vc}$ under the Tamm-Dancoff approximation is

$$(E_c - E_v)A^S_{vc} + \sum_{v'c'} K^{AA}_{vc,v'c'}(\Omega_S)A^S_{v'c'} = \Omega_S A^S_{vc}. \tag{1.53}$$

We could further calculate the imaginary part of the transverse dielectric function $\epsilon_2$ by $|S\rangle$ and $\Omega_S$.

$$\epsilon_2(\omega) = \frac{16\pi e^2}{\omega^2}\sum_S |\boldsymbol{\lambda}\cdot\langle 0|\,\boldsymbol{v}\,|S\rangle\,|^2\delta(\omega-\Omega_S), \tag{1.54}$$

where $\boldsymbol{\lambda}$ is the polarization vector of the light and $\boldsymbol{v} = i/\hbar[H,\boldsymbol{r}]$ is the single-particle velocity operator (which corresponds to the current operator).

The optical absorption spectrum of bulk silicon was calculated using i) the GW band structure within the interband transition approximation and ii) the GW-BSE method from first-principles using the BerkeleyGW package [31]. The GW-BSE method includes the electron-hole interactions (excitonic effects), so it agrees very well with the experimentally measured absorption spectra [54].

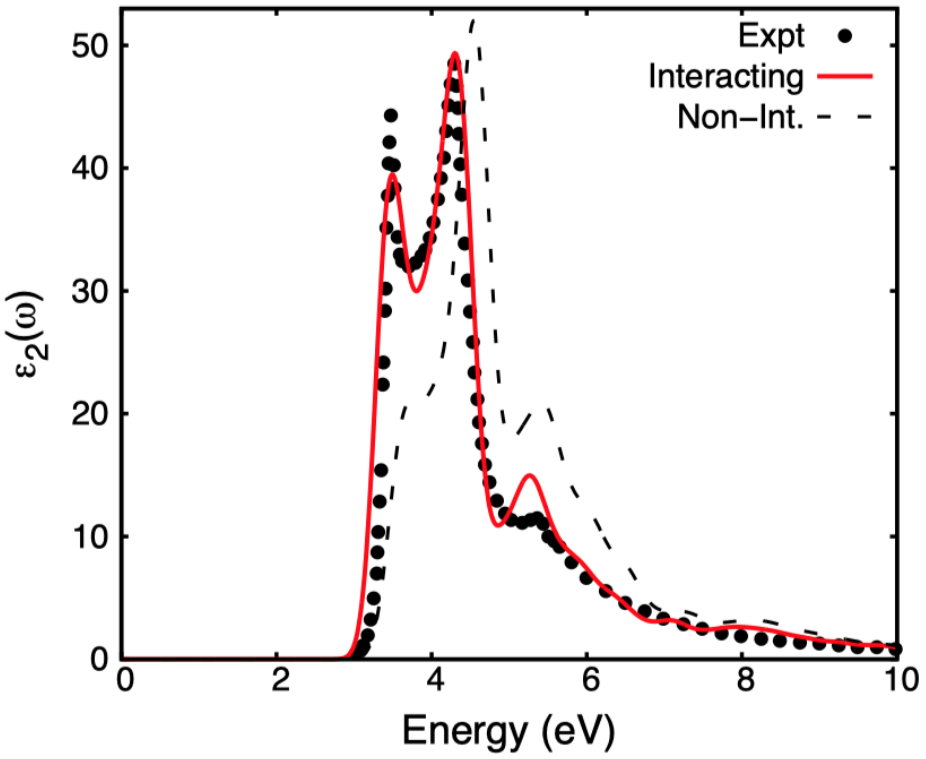


Figure 1.1: The calculated absorption spectra for silicon by the interband transition method with the GW band structure (black dashed) and the GW-BSE (red solid) method which includes electron-hole interactions using the BerkeleyGW package [31]. The dotted line is experimental data from [54]. The figure is taken from Ref. [31].

# Chapter 2

# Topological phases in graphene nanoribbons

In this chapter, we present a systematic study of topological electronic properties of a class of quasi-one-dimensional carbon-based material, the graphene nanoribbons (GNRs). We first present our development of topological classification schemes for theses systems, and present our results of topological classification in armchair GNRs and GNRs of other edge shapes. We then present a possible application of topological phases in GNRs in electronic devises, which utilize the electric field to explore tunable properties in topological phases. Finally, we present a theory and experiment collaborated work on topological band engineering in GNRs. This chapter is based on published papers [21, 65, 90] and preprint [116].

## 2.1 Introduction

GNR is a quasi-one-dimensional material that could be cut from two-dimensional graphene sheets. Depending on how one cuts the ribbon, the GNR can have different edge shapes, and the most common edge shapes are the armchair- and zigzag-like edges. The armchair GNR (AGNR) has sizable energy gaps depending on its width arising from quantum confinement effect [101, 113] and has been used in building extremely narrow transistors [70, 10] because of its high mobility and narrow size. The zigzag GNRs (ZGNRs) have anti-ferromagnetically aligned spin ordered states which makes it a promising material in spintronics. In addition, ZGNRs also have field- or strain-driven half-metallicity behaviors [36, 102].

Moreover, the recent rapid development of bottom-up synthesis techniques of GNRs from precursor molecules enables atomically precise design of a large variety of GNRs, including the control of widths [18, 27, 10], dopant atoms [79, 81, 95], and diverse edge shapes [19, 26, 77, 106].

In this chapter, we show that semiconducting GNRs possess topological phases, and GNRs of different widths, edge and termination (synthesizable from molecular

precursors with atomic precision) belong to different electronic topological classes. The topological phase of GNRs is protected by spatial symmetries and dictated by the terminating unit cell. We derive explicit formulas for their topological invariants and show that localized junction states developed between two GNRs of distinct topology may be tuned by lateral junction geometry, according to the bulk edge correspondence. The topology of a GNR can be further modified by dopants, such as a periodic array of boron atoms. In a superlattice consisting of segments of doped and pristine GNRs, the junction states are stable spin centers, forming a Heisenberg antiferromagnetic spin 1/2 chain with tunable exchange interaction. The discoveries here not only are of scientific interest for studies of quasi-one-dimensional systems, but also open a new path for design principles of future GNR-based devices through their topological characters.

## 2.2 Topological classification in quasi-1D systems

The topology of a crystal's electronic structure, in par with its band structure and electron filling, plays an essential role in its electronic properties [107, 43, 87]. The discovery of topology in the electronic structure of crystalline materials has led to deep insights to novel electronic phenomena such as the integer quantum Hall effect [60, 107] and fermion number fractionalization [53, 103, 46], and other properties [63, 112]. Joining two insulators of different topological classes produces fascinating localized boundary states in the band gap [107, 43, 87]. This section is primarily adapted from Ref. [21].

In mathematics, the topology of a compact object is characterized by global invariants that may be obtained through an integral of local quantities. In a quasi-one-dimensional (1D) crystal, the electronic bands are defined in the 1D Brillouin zone (BZ). The 1D BZ has the shape of a circle and is therefore a closed compact manifold which may host topological quantities.

The band topological invariant of a 1D insulating crystal with multiple atoms per unit cell such as GNRs depends on the assignment of its unit cell, which in turn is dictated by the atomic structure at the end termination of the 1D system (i.e., the unit cell should be commensurate with the boundary geometry) [21]. These topological phases can be characterized by a $Z_2$ invariant that is protected by the spinless time reversal symmetry (TRS) and a spatial mirror and/or inversion symmetry commensurate with the GNR terminating unit cell [21, 35], as well as a Z bulk winding number protected by an approximate chiral symmetry (if exists) at the charge neutral gap [55]. We introduce both these two classification schemes below for the GNRs.

### 2.2.1 $Z_2$ classification

A $Z_2$ topological classification can be exactly applied to an 1D insulating crystal with spinless time reversal symmetry (TRS) and spatial inversion/mirror symmetry [21].

In an 1D crystal, the Zak phase [31] for the nth band is defined as the integral of the Berry's connection across the 1D Brillouin zone (BZ)

$$\gamma_n = i\left(\frac{2\pi}{d}\right)\int_{-\pi/d}^{\pi/d} dk\,\langle u_{nk}|\,\frac{\partial}{\partial k}\,|u_{nk}\rangle\,, \tag{2.1}$$

where $u_{nk}$ is the lattice-periodic part of the Bloch state, d is the unit cell size, and $k$ is the wavevector. The Zak phase of an isolated band of a general 1D insulator can take on any value, depending on the choice of the shape and origin of the unit cell. Nevertheless, if the unit cell of the crystal has inversion/mirror symmetry, the intercell (origin independent) part of the Zak phase is uniquely determined for a given unit cell shape and is quantized to 0 or $\pi$ (mod $2\pi$) [21, 65]. The $Z_2$ invariant of a 1D insulator with such symmetries is then given by

$$(-1)^{Z_2} = e^{i\sum_{n\in occ}\gamma_n}, \tag{2.2}$$

where the sum is over the occupied bands. When the total intercell Zak phase is $\pi$ (0) (mod $2\pi$ ), the $Z_2$ invariant is 1 (0). As shown in previous work [35, 21], for a unit cell with inversion $\hat{I}$ or mirror $\hat{M}$ symmetry ( $\hat{O} = \hat{I}$ or $\hat{M}$), the $Z_2$ invariant of a GNR may be determined by the product of the eigenvalues of $\hat{O}$ of the states at all the time reversal invariant momentum (TRIM) k-points in the occupied band manifold:

$$(-1)^{Z_2} = \prod_{n\in occ}\prod_{\Gamma_i}\langle\psi_{n\Gamma_i}|\,\hat{O}\,|\psi_{n\Gamma_i}\rangle\,, \tag{2.3}$$

where the TRIM $\Gamma_i = \Gamma, X$ in the 1D BZ.

For experimentally bottom-up synthesized GNR systems, the dangling $\sigma$ orbitals of the edge carbon atoms are capped by hydrogen, and are removed in energy from the band gap region, so these $\sigma$ states are not involved in the formation of the end/junction in-gap states. Also, because the GNRs considered in this work have a mirror symmetry with respect to the carbon basal plane, the $\sigma$ (mirror even) and $\pi$ (mirror odd) bands do not hybridize. Only the $\pi$ bands account for the in-gap physics of interest. Thus, both the $Z$ (which we will talk about in the section below) and $Z_2$ invariants of the GNRs of interest are calculated from the occupied band manifold of $\pi$ electrons (denoted by "$\pi$&$occ$") only. For example, $Z_2$ is given by

$$(-1)^{Z_2} = \prod_{n\in\pi\&occ}\langle\psi_{n\Gamma}|\,\hat{O}\,|\psi_{n\Gamma}\rangle\,\langle\psi_{nX}|\,\hat{O}\,|\psi_{nX}\rangle\,. \tag{2.4}$$

### 2.2.2 $Z$ classification

On the other hand, for GNRs with no spatial symmetry, using the approximate chiral symmetry (the A/B sublattice symmetry) of the GNRs, the band topology of this

multi-band system can be characterized by a winding number Z, which may be obtained using the difference between the intercell part of the Zak phase contributed by the A sublattice and that contributed by the B sublattice, summed over all bands up to the charge neutrality gap as shown in Ref. [55]. For such a system with a winding number $Z$, there will be Z topologically protected localized in-gap state at its end termination with vacuum, according to the bulk-edge correspondence [86].

A system has chiral symmetry if there exists a unitary operator, $\hat{\Gamma}$, such that

$$\hat{\Gamma} H \hat{\Gamma}^\dagger = H, \tag{2.5}$$

$$\hat{\Gamma}\hat{\Gamma}^\dagger = I. \tag{2.6}$$

In the basis of the eigenvectors of the chiral operator $\hat{\Gamma}$, the Hamiltonian can be written in a block off-diagonal form

$$H = \begin{pmatrix} 0 & h(k) \\ h(k)^\dagger & 0 \end{pmatrix}. \tag{2.7}$$

The chiral symmetry constrains some degrees of freedom of the Hamiltonian matrix, making it block off-diagonal in certain basis, so a winding number of the determinant of $h(k)$ around the origin in the complex plane may be defined. The Z index defined by this winding number is given as [5]

$$Z = \frac{1}{2\pi i}\int_{-\pi}^{\pi} dk \frac{d}{dk} \ln(\det(h(k))). \tag{2.8}$$

## 2.3 Topological phases in armchair graphene nanoribbons

### 2.3.1 Calculation of the $Z_2$ invariant of armchair graphene nanoribbons within the tight-binding model

We shall use the construction that the $Z_2$ invariant of a 1D crystal with inversion and/or mirror symmetries is given by Eqn. (2.4). We start from the wavefunction of graphene to construct the wavefunctions of the AGNRs by imposing proper boundary conditions, and then analyze the wavefunction parities of the AGNR. Considering only nearest neighbor hopping between the carbon $\pi$ orbitals, the Hamiltonian of graphene is

$$H^g(\boldsymbol{k}) = -t \begin{pmatrix} 0 & 1 + e^{ia(-\frac{\sqrt{3}}{2}k_x + \frac{1}{2}k_y)} + e^{ia(-\frac{\sqrt{3}}{2}k_x - \frac{1}{2}k_y)} \\ 1 + e^{ia(\frac{\sqrt{3}}{2}k_x + \frac{1}{2}k_y)} + e^{ia(\frac{\sqrt{3}}{2}k_x - \frac{1}{2}k_y)} & 0 \end{pmatrix}, \tag{2.9}$$

where $t$ is the nearest neighbor hopping parameter, $a$ the lattice constant, $k_x$ and $k_y$ the components of Bloch wavevector $\boldsymbol{k}$ in the $x$ and $y$ directions, respectively (Fig. 2.1 and 2.2). The wavevector $\boldsymbol{k}$ is measured from the center of the 2D BZ. The off-diagonal matrix element can be written as

$$H_{12}^{g}(\boldsymbol{k}) = -t\left[1 + 2\cos(\frac{ak_y}{2})\cos(\frac{\sqrt{3}ak_x}{2}) - 2i\cos(\frac{ak_y}{2})\sin(\frac{\sqrt{3}ak_x}{2})\right]. \tag{2.10}$$

Using the pseudospin notation, the Hamiltonian of graphene can be rewritten as

$$H^{g}(\boldsymbol{k}) = -t\boldsymbol{h}(\boldsymbol{k})\cdot\sigma, \tag{2.11}$$

where $\sigma_i$ are the Pauli matrices. The $x$ and $y$ components of the pseudo-magnetic field $\boldsymbol{h}(\boldsymbol{k})$ are

$$h^{x}(\boldsymbol{k}) = 1 + 2\cos(\frac{ak_y}{2})\cos(\frac{\sqrt{3}ak_x}{2}), \tag{2.12}$$

and

$$h^{y}(\boldsymbol{k}) = 2\cos(\frac{ak_y}{2})\sin(\frac{\sqrt{3}ak_x}{2}). \tag{2.13}$$

By solving the Hamiltonian in Eqn. (2.11) , the energies $E$ and eigenstates $u^g$ of the conduction band and valence band from the carbon $\pi$ orbitals at each $\boldsymbol{k}$ point are

$$E_{\pm}(\boldsymbol{k}) = \pm t\sqrt{h_x^2(\boldsymbol{k}) + h_y^2(\boldsymbol{k})} \tag{2.14}$$

$$u_{\pm}^{g}(\boldsymbol{k}) = \frac{1}{\sqrt{2}}\begin{pmatrix} e^{-i\phi(\boldsymbol{k})} \\ \mp 1 \end{pmatrix}, \tag{2.15}$$

where

$$e^{-i\phi(\boldsymbol{k})} = \frac{h_x(\boldsymbol{k}) - h_y(\boldsymbol{k})}{\sqrt{h_x^2(\boldsymbol{k}) + h_y^2(\boldsymbol{k})}}. \tag{2.16}$$

The "-" and "+" signs in the equations above denote the valence and conduction bands, respectively. To obtain the symmetry properties of wavefunctions, we now construct the wavefunctions of the AGNRs using the graphene wavefunctions with proper boundary conditions. With only nearest neighbor hopping between carbon atoms considered, the wavefunction of the AGNR must vanish beyond the carbon atoms at the armchair edge. Therefore, the boundary conditions for the AGNR with $N$ rows of carbon atoms (see Fig. 2.1) are

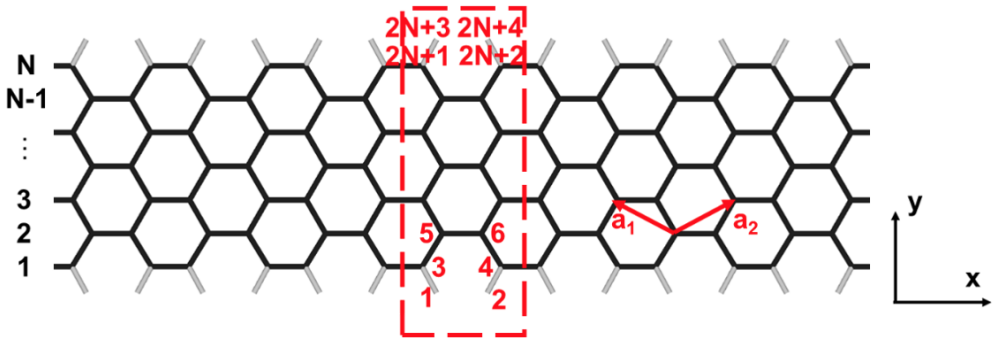


Figure 2.1: Schematic structure of AGNRs with N rows of carbon atoms. The carbon-carbon bonds and carbon-hydrogen bonds are colored black and gray, respectively. The black numbers on the left label the row number of carbon atoms of the AGNR. The red numbers labels the carbon atom in a unit cell. The red dashed line denotes a unit cell of the AGNR. The red arrows are lattice vectors of graphene.

$$\langle 1|u_n(k_x)\rangle = \langle 2|u_n(k_x)\rangle = \langle 2N+3|u_n(k_x)\rangle = \langle 2N+4|u_n(k_x)\rangle = 0. \tag{2.17}$$

Here the orbitals "$\langle 1|$", "$\langle 2|$", "$\langle 2N+3|$", and "$\langle 2N+4|$" are the $\pi$ orbitals of the virtual carbon atoms located next to the outmost edge carbon atoms "3", "4", "2N+1", and "2N+2", respectively (Fig. 2.1). $u_n(k_x)$ denotes the wavefunction of the $n$-th band of an AGNR at the wavevector $k_x$.

Using the boundary conditions in Eqn. (2.17), we construct the wavefunctions of the occupied states in the $n$th band of the AGNR,

$$u_n(k_x) = \frac{1}{\sqrt{2}}\left[u^g_-(k_x, k_y(n)) - u^g_-(k_x, -k_y(n))\right]. \tag{2.18}$$

As shown in Fig. 2.2, the state in band $n$ of wavevector $k_x$ is composed of states of graphene with momentum $(k_x, k_y)$ and $(k_x, -k_y)$ with $k_y$ given by the quantized value,

$$\frac{(N+1)a}{2}k_y(n) = n\pi, \tag{2.19}$$

or

$$k_y(n) = \frac{n}{N+1}\frac{2\pi}{a}, (n = 1, 2, ..., N). \tag{2.20}$$

The wavefunctions of the AGNR are then obtained from the wavefunctions of graphene. Using the unit cell of the AGNR shown in Fig. 2.1, the tight-binding wavefunction of the valence band of graphene is

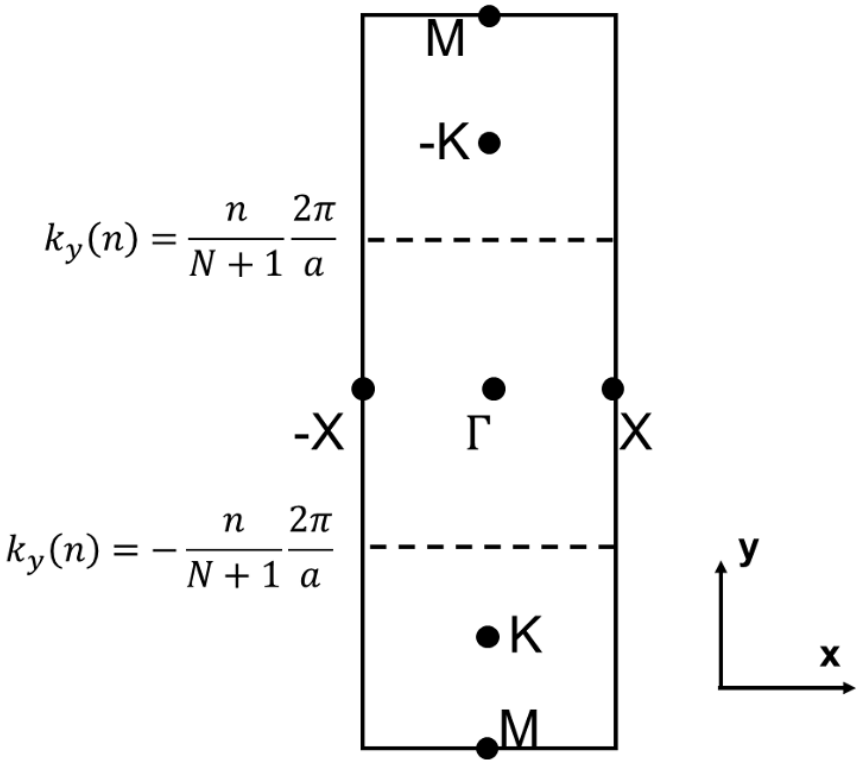


Figure 2.2: Brillouin zone and high symmetry points of graphene. The dashed lines show the specific k path of which the wavefunctions of graphene constitute the $n$-th band of an N-AGNR.

$$u_{-}^{g}(k_x, k_y(n)) = \frac{1}{\sqrt{2N}} \begin{pmatrix} e^{i\boldsymbol{k}\cdot\boldsymbol{a}_1} \\ e^{-i\phi(\boldsymbol{k})} e^{i\boldsymbol{k}\cdot\boldsymbol{a}_2} \\ e^{-i\phi(\boldsymbol{k})} e^{ik_y a} \\ e^{ik_y a} \\ \cdots \end{pmatrix}, \tag{2.21}$$

where the first component is the amplitude on site #3, the second component is the amplitude on site #4, etc. (Fig. 2.1) (Here for notational simplicity, we have just used "$k_y$" for "$k_y(n)$" on the right hand side of Eqn. (2.21) and in subsequent equations below.) Using Eqn. (2.18) and (2.21), the explicit form of the $n$-th valence band wavefunctions of the AGNR is

$$u_n(k_x, k_y(n)) = \frac{1}{\sqrt{N}} \begin{pmatrix} e^{-ik_x \frac{\sqrt{3}}{2}a} i \sin(k_y \frac{a}{2}) \\ e^{-i\phi(\boldsymbol{k})} e^{ik_x \frac{\sqrt{3}}{2}a} i \sin(k_y \frac{a}{2}) \\ e^{-i\phi(\boldsymbol{k})} i \sin(k_y a) \\ i \sin(k_y a) \\ ... \end{pmatrix}. \tag{2.22}$$

We define a function $f(\boldsymbol{k}) = e^{-i\phi(\boldsymbol{k})}$. The wavefunction of the band $n$ at the $\Gamma$ point is

$$u_n(\Gamma) = \frac{1}{\sqrt{N}} \begin{pmatrix} i \sin(\frac{n\pi}{N+1}) \\ f_n(\Gamma) i \sin(\frac{n\pi}{N+1}) \\ f_n(\Gamma) i \sin(\frac{2n\pi}{N+1}) \\ i \sin(\frac{2n\pi}{N+1}) \\ ... \end{pmatrix}. \tag{2.23}$$

We obtain that for $N = 3m$ and $3m + 1$ ($m$ is a positive integer),

$$\prod_{n \in \pi \& occ} \langle \psi_{n\Gamma} | \hat{O} | \psi_{n\Gamma} \rangle = (-1)^m. \tag{2.24}$$

For $N = 3m+2$. The system does not have a gap in this simple tight-binding model, as one of the bands passes through the K point of graphene. However, a sizeable band gap does exist in these graphene nanoribbons from *ab initio* DFT calculations. The presence of the band gap in most part is due to the contraction of carbon-carbon bond on the armchair edges, leading to a stronger electron hopping between these edge carbon atoms. Using bigger hopping parameters on the edge carbon atoms, the tight-binding band gap approaches the *ab initio* results. We thus calculate the $\Gamma$ point wavefunctions in these cases ($N = 3m+2$) using this method, and find that the relation Eqn. (2.24) still holds.

The wavefunction of the band $n$ at the X point is

$$u_n(X) = \frac{1}{\sqrt{N}} \begin{pmatrix} \sin(\frac{n\pi}{N+1}) \\ -f_n(\Gamma) \sin(\frac{n\pi}{N+1}) \\ f_n(\Gamma) i \sin(\frac{2n\pi}{N+1}) \\ i \sin(\frac{2n\pi}{N+1}) \\ ... \end{pmatrix}. \tag{2.25}$$

For the parity eigenvalues at $X$ point, we obtain that for $N = 4r$ and $4r + 3$ ($r$ is a positive integer),

$$\prod_{n \in \pi \& occ} \langle \psi_{nX} | \hat{O} | \psi_{nX} \rangle = 1. \tag{2.26}$$

For $N = 4r + 1$ and $4r + 2$,

$$\prod_{n\in\pi\&occ} \langle\psi_{nX}|\,\hat{O}\,|\psi_{nX}\rangle = -1. \tag{2.27}$$

As a result, the products of the parity eigenvalues of states at $\Gamma$ and $X$,

$$\prod_{n\in\pi\&occ} \langle\psi_{n\Gamma}|\,\hat{O}\,|\psi_{n\Gamma}\rangle\,\langle\psi_{nX}|\,\hat{O}\,|\psi_{nX}\rangle = (-1)^{\lfloor\frac{N}{3}\rfloor}(-1)^{\lfloor\frac{N+1}{2}\rfloor}, \tag{2.28}$$

where the floor function $\lfloor x\rfloor$ takes the largest integer less than or equal to a real number $x$. Therefore, we obtain the value of $Z_2$ of AGNR with zigzag' (N = odd) and zigzag (N = even) terminations, which is shown in the table in Table 2.1.

We have also derived the value of $Z_2$ for the bearded (N = even) and zigzag (N = odd) terminations (shown in Fig. 2.1) that have inversion symmetry using similar methods. The products of the parity eigenvalues of states at $\Gamma$ and $X$ are $(-1)^{\lfloor\frac{N}{3}\rfloor}$ and $-(-1)^{\lfloor\frac{N}{3}\rfloor}(-1)^{\lfloor\frac{N+1}{2}\rfloor}$ for the bearded (N = even) and zigzag (N = odd) terminations, respectively. These results together give the formulae presented in Table 2.1.

### 2.3.2 the $Z_2$ invariant of armchair graphene nanoribbons

Since the band topological classification of a 1D insulating crystal requires the unit cell to be commensurate with the boundary geometry, there are 4 kinds of terminations of the AGNRs that possess the unit cell with inversion symmetry. As shown in Table 2.1, for N = odd AGNRs, both the zigzag and zigzag$'$ terminations have inversion and mirror symmetry, while for N = even AGNRs, the zigzag and bearded terminations have only one type of symmetry, mirror and inversion symmetry, respectively. Other types of terminations, e.g., ones that cut nonperpendicular to the AGNR axis, should also support symmetry phases, as long as its bulk unit cell has spatial symmetries.

### 2.3.3 Junction states in armchair graphene nanoribbon heterojunctions

A topological classification of the GNRs (e.g., the one given in Table 2.1 for the AGNRs) provides a useful, systematic way to understand and design the electronic and transport properties of GNR junctions. Since the topology of the ground state of a GNR segment depends on the shape of its termination, the electronic structure at a junction can vary, depending on how the two segments are joined laterally (without making any other changes). We demonstrate this novel effect by constructing GNR junctions with two AGNRs of different widths. In this pristine AGNR system, there is also an approximate chiral symmetry, which implies approximate electron-hole symmetry. In the charge neutral energy gap, the bulk-edge correspondence in the $Z_2$ classification still holds,

| Termination type | Zigzag ($N$ = Odd) | Zigzag' ($N$ = Odd) | Zigzag ($N$ = Even) | Bearded ($N$ = Even) |
|---|---|---|---|---|
| Unit cell shape | 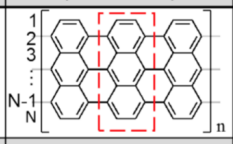 | 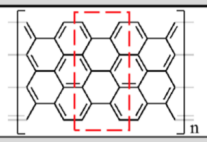 | 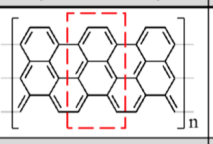 | 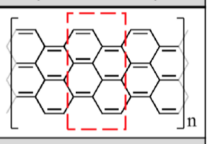 |
| Bulk Symmetry | Inversion/mirror | Inversion/mirror | Mirror | Inversion |
| $Z_2$ | $\frac{1+(-1)^{\lfloor\frac{N}{3}\rfloor+\lfloor\frac{N+1}{2}\rfloor}}{2}$ | $\frac{1-(-1)^{\lfloor\frac{N}{3}\rfloor+\lfloor\frac{N+1}{2}\rfloor}}{2}$ | | $\frac{1-(-1)^{\lfloor\frac{N}{3}\rfloor}}{2}$ |

Table 2.1: Categorization of electronic topology of AGNRs. The nanoribbons are identified according to the type of termination (labeled in the first row) and width. Schematics of AGNR structure with different termination types is defined and plotted in the second row. The bracket denotes a specific termination of an infinitely long AGNR. The row number for the carbon atoms along the lateral direction are labeled from "1" to "N". The bulk unit cell of each structure that is commensurate with the termination is indicated by the dashed red rectangle. The bulk symmetry is indicated in the third row. The value of the $Z_2$ invariant is given in the fourth row. The floor function $\lfloor x \rfloor$ takes the largest integer less than or equal to a real number $x$.

and we will discuss the bulk-edge correspondence in the $Z_2$ classification in detail in Chapter 3.

Figure 2.3 shows two possible types of junctions formed by an N = 7 and an N = 9 AGNR. For the non-symmetric junction [Fig. 2.3 (a)], both the N = 7 and N = 9 segments have $Z_2 = 1$ (Table 2.1). From the bulk-edge correspondence, zero or an even number of localized junction states is expected in the charge neutral gap. For the symmetric junction [Fig. 2.3 (b)], though the N = 7 and N = 9 AGNRs only shift laterally with each other, the $Z_2$ of the N = 7 segment changes from 1 to 0 owing to a different termination (Table 2.1), while the $Z_2$ of the N = 9 segment remains unchanged. As a result, one or an odd number of localized junction states should emerge in the charge neutral gap.

We verified these rather counterintuitive results by performing explicit DFT calculations on these two types of junctions. Our DFT calculations show that no junction state exists at the non-symmetric junction, whereas one localized junction state with midgap energy appears at the symmetric junction even though the structure is now more symmetrical. The calculated charge density distribution of the junction state is shown in Fig. 2.3(b). For both the non-symmetric and the symmetric junctions, only the carbon $\pi$ orbitals are involved with the formation of states near or in the band gap, and the number of carbon atoms is exactly the same.

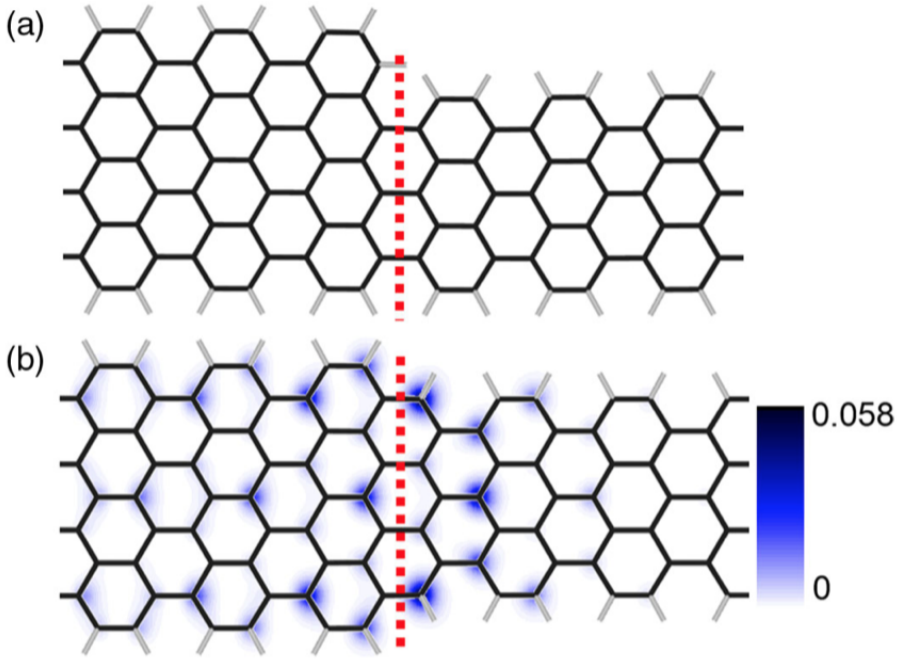


Figure 2.3: Heterojunctions formed with N = 9 and N = 7 armchair graphene nanoribbons (9AGNR/7AGNR) between two (a) topologically equivalent segments and (b) topologically inequivalent segments. The red dashed line denotes the interface between the two nanoribbons. The carbon-carbon and carbon-hydrogen bonds are colored black and gray, respectively. The color scale shows the charge density of the localized midgap junction state. The charge density is integrated along the out-of-plane direction [in units of $1/(a.u.)^2$ ].

### 2.3.4 Topological invariant modified by dopant atoms

The symmetry protected topological phase may be modified by periodically doping in GNRs. The physics for this phenomenon is that, upon doping, a GNR may acquire a different Zak phase from the dopant bands and can therefore change its topological class. An N = 7 AGNR with periodically substitutional boron doped atoms at its backbone has been successfully synthesized recently with bottom-up molecular precursor techniques [81]. We investigate the topological phase in this doped GNR systems.

Figure 2.4(a) shows the experimentally synthesized structure of a periodically substitutionally doped N = 7 AGNR by boron pairs (B2-7AGNR). Because of the change in ground-state topology, as we shall show, contrary to 7AGNR, there is no midgap end state at the vacuum/B2-7AGNR interface for the neutral system, but there is a midgap junction state at the 7AGNR/B2-7AGNR interface. Figure 2.4(b) depicts the quasiparticle band structure of B2-7AGNR calculated using the *ab initio* GW approach with the BerkeleyGW package [31]. The lowest conduction (at ∼2 eV) and the highest

valence (at ∼0 eV) band of the doped system have wave functions derived from the dopant orbitals of an isolated boron pair in 7AGNR and are therefore named as the upper and lower dopant bands, respectively. The calculated quasiparticle band gap, 2.0 eV from the *ab initio* GW energies, is significantly larger than the Kohn-Sham band gap (0.6 eV) from the DFT within the local density approximation, although the basic character of the wave functions does not change. This large change in the band gap between the two methods reflects the strong many-electron effects in the band energy of a quasi-1D material; the GW approach more accurately computes the electron self-energy than the DFT [50]. The calculated Zak phases of the lower and upper dopant bands in Fig. 2.4(b) are $-\pi$ and $\pi$, respectively. As the B2-7AGNR has two less electrons per unit cell than pristine AGNR, the total Zak phase of B2-7AGNR must differ from that of a pristine 7AGNR by $\pi$, owing to the emptying out of the upper dopant band and that the Hamiltonian of the doped system may be obtained adiabatically from the pristine system without closing the band gap. We verified this reasoning with an explicit calculation of the $Z_2$ invariant for B2-7AGNR. Therefore, substitutionally periodic doping by boron pairs changes the topological class of 7AGNR.

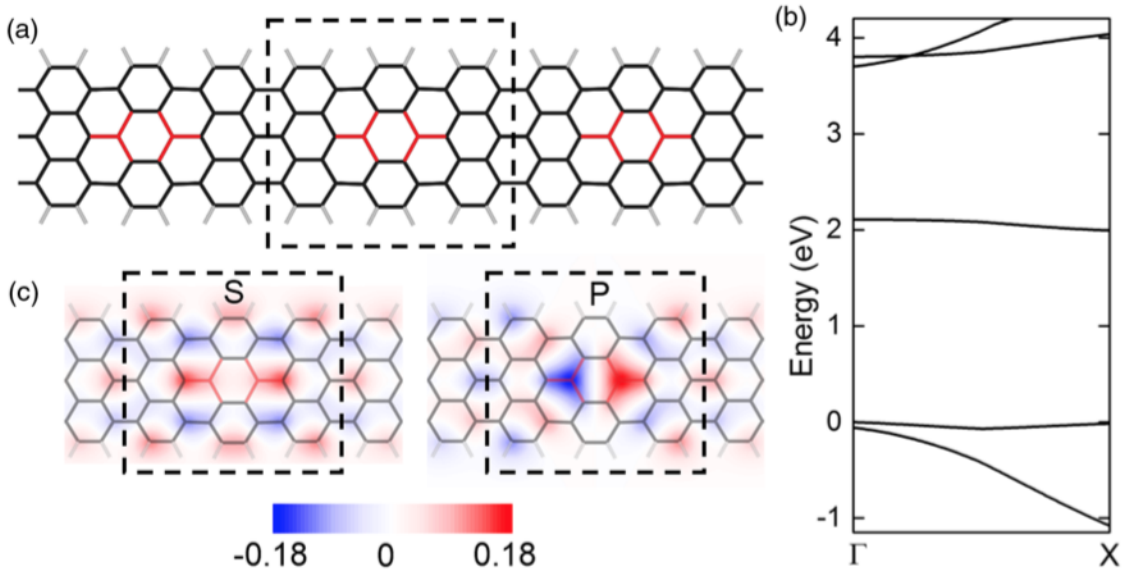


Figure 2.4: Boron-doped graphene nanoribbons. (a) Structure of an N = 7 AGNR periodically doped with boron pairs (B2-7AGNR). The carbon-carbon, carbon-boron, and carbon-hydrogen bonds are colored black, red, and gray, respectively. The dashed black rectangle indicates a unit cell. (b) Band structure of the B2-7AGNR calculated with the *ab initio* GW method. The top of the valence band is set at 0 eV. (c) Wave function of dopant orbitals with $s$ and $p$ symmetries, plotted at 1 Angstrom above the nanoribbon plane. The red and blue color shows positive and negative amplitudes [in units of $1/(a.u.)^{(3/2)}$ ].

### 2.3.5 Quantum spin chains

A superlattice formed with alternate segments of doped (B2-7AGNR) and pristine 7AGNR ribbons hosts a periodic array of junction states, with one electron occupying each localized junction state for the neutral system [Fig. 2.5(a)]. The midgap junction state in this system has a large calculated onsite Coulomb U of nearly 500 meV within the local spin density approximation (LSDA) and therefore is a localized spin center at each junction.

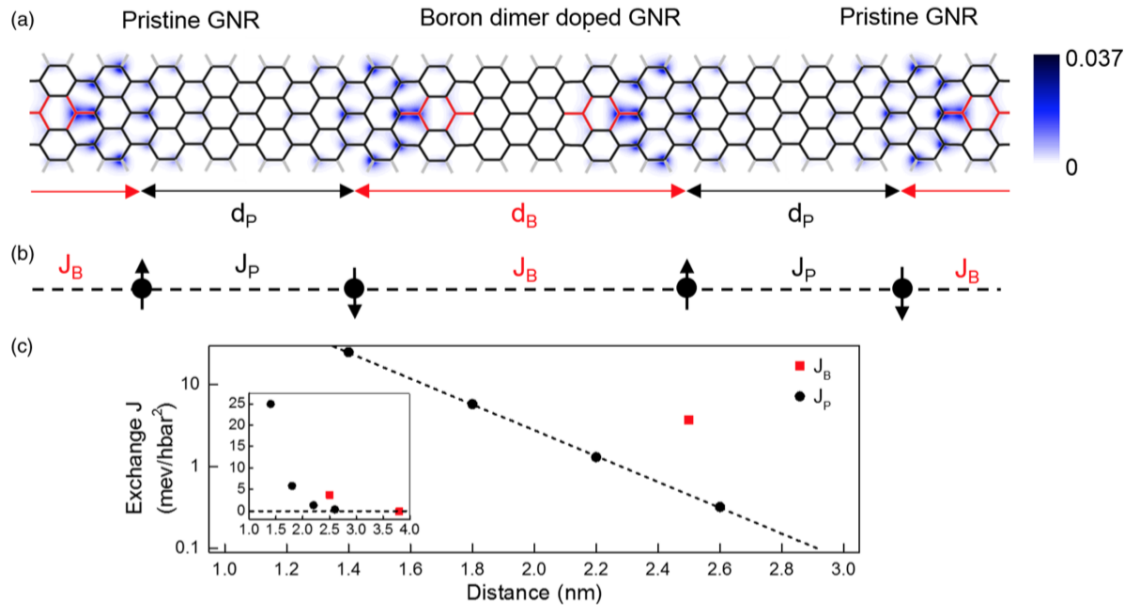


Figure 2.5: Doped-pristine AGNR superlattice. (a) Structure of a 7AGNR/B2-7AGNR superlattice. The carbon-carbon, carbon-boron, and carbon-hydrogen bonds are colored black, red, and gray, respectively. The color scale shows the charge density distribution of the lower junction-state band integrated over states in the superlattice BZ and integrated over the direction perpendicular to the ribbon plane [in units of $1/(a.u.)^2$ ]. (b) Schematics of the 1D antiferromagnetic Heisenberg spin 1=2 chain corresponding to the system shown in (a). The arrows denote relative directions of electron spins. (c) *Ab initio* calculated exchange parameters in the Heisenberg model as a function of the separation distance, in log scale and linear scale (inset).

The interactions between these spin centers give rise to a 1D Heisenberg-type antiferromagnetic (AFM) spin 1/2 chain [Fig. 2.5(b)]. The effective exchange interactions between the spin centers are mediated both through the boron-doped segment and the pristine segment. The spin-dependent part of the Hamiltonian may be cast as

$$H = \sum_i \left[ J_B(d_B) \boldsymbol{S}_i^1 \cdot \boldsymbol{S}_i^2 + J_P(d_P) \boldsymbol{S}_i^2 \cdot \boldsymbol{S}_{i+1}^1 \right], \tag{2.29}$$

where "i" labels the unit cell index of the superlattice. There are two spin centers (labeled 1 and 2) in each supercell. We calculate by the DFT in the LSDA (from total-energy differences among different constrained spin configurations) the exchange parameters $J_B$ (through the B2-7AGNR segment) and $J_P$ (through the pristine 7AGNR segment) as a function of the distance between the spin centers, i.e., $d_B$ and $d_P$, respectively. Figure 2.5(c) shows the dependence of the exchange parameters on the distance. All the calculated exchange interactions are positive, indicative of an AFM coupling between the spins. Remarkably, the exchange interaction energies can be as large as $\sim$ 5 meV, even if the two spin centers are $\sim$ 2 nm apart. These highly stable spin centers and their exchange interactions offer a useful and tunable material platform to study novel quantum spin effects in 1D systems [11].

## 2.4 Topological phases in graphene nanoribbons of other edge geometries: chevron and cove-edged graphene nanoribbons

This section is primarily adapted from Ref. [65].

In addition to the AGNRs, we also study the topological phases in GNRs of other edge shape and terminations. In this section, we focus on the topological phases in cove-edged and chevron GNRs. Cove-edged and chevron GNRs moreover are chemically and structurally diverse, quasi-one-dimensional (1D) nanostructures whose structure and electronic properties can be rationally controlled by bottom-up synthesis from precursor molecules. We derive the value of the topological invariant of the different types of cove-edged and chevron GNRs, and we investigate the electronic properties of various junctions formed by these GNRs, as well as such GNRs with the more common armchair or zigzag GNRs.

We use both tight-binding models and first-principles calculations to calculate the topological invariants $Z_2$ in cove-edged and chevron GNRs. In this section, we first summarize the two methods we use to calculate the topological invariants, and we show the calculated $Z_2$ for cove-edged GNR of different widths and chevron GNRs. We study the topological junction states at the interface of two topologically distinct segments. For an isolated GNR having two ends of different terminations, topological end states are shown to develop only at the topologically nontrivial end.

### 2.4.1 The tight-binding formalism in calculating $Z_2$: degenerate band case

For the cove-edge and chevron GNRs, most of the ribbons has a screw rotation symmetry (a 180 degree rotation plus a half-unit-cell-length translation) which preserves the degeneracy at X point. We generalize our formalism (Eqn. (2.4)) to deal with the degeneracy

$$(-1)^{Z_2} = \det_{n,m\in\pi\&occ} \langle\psi_{n\Gamma}|\,\hat{O}\,|\psi_{m\Gamma}\rangle \det_{n,m\in\pi\&occ} \langle\psi_{nX}|\,\hat{O}\,|\psi_{mX}\rangle\,, \tag{2.30}$$

because degenerate bands allows arbitrary mixing between bands within the degenerate subspace, which makes the off-diagonal element $\langle\psi_{n\Gamma}|\,\hat{O}\,|\psi_{m\Gamma}\rangle$ nonzero. We replace the calculation of a product over all the diagonal elements to the calculation of the determinant.

### 2.4.2 Calculation of $Z_2$: the Wannier function method

We present in this subsection another method for calculating Z2 of GNRs. Wannier functions (WFs) are an orthonormal set of the spatially localized functions in a crystal that spans the same space as a specified set of Bloch bands. The Zak phase of the $n$th isolated band in a 1D crystal is directly given by the center of the WF associated with the $n$th band, which is defined to be the expectation value of the position operator $r$ of the WF. The position of the Wannier center of an isolated band is defined as

$$\bar{r_n} = \langle 0, n|\,\hat{r}\,|0, n\rangle\,, \tag{2.31}$$

where $|0, n\rangle$ is the $n$th WF associated with the unit cell labeled by the 0th lattice vector.

The position of the Wannier center of an isolated band is proportional to the intercell Zak phase of that band [12, 73, 99, 100] . It is uniquely determined for a system once the unit cell is defined. Thus, the summation of all the $\pi$ electron Wannier centers gives the total intercell Zak phase associated with the occupied manifold of the $\pi$ electrons when the unit cell of the crystal has inversion/mirror symmetry. We have

$$(-1)^{Z_2} = e^{i\sum_{n\in\pi\&occ}\gamma_n} = e^{i(\frac{2\pi}{d})\sum_{n\in\pi\&occ}\bar{x_n}}, \tag{2.32}$$

where $d$ is the length of the unit cell in the periodic direction $x$.

For example, we can arrive at the value of the topological invariant of the N = 5 cove-edged GNR system from the centers of the WFs shown in Figure 2.6e. The red dots represent the positions of the $\pi$-electron Wannier function centers (WCs). The sum of the positions of all the occupied $\pi$-WCs is located at the center of the unit cell as shown in Figure 2.6e, which indicates that the total intercell Zak phase is 0 and $Z_2$ = 0. If we shift the defining boundary of the unit cell by 1/4 of a primitive translation

vector, inversion symmetry still holds, but the sum of the positions of the $\pi$-electron WCs is now located at the boundary of the new unit cell. As a result, the topological invariant $Z_2$ becomes 1 for the new, shifted unit cell.

### 2.4.3 $Z_2$ invariants for cove-edged and cheveron GNRs

The structures of cove-edged GNRs are essentially zigzag GNRs with periodic carbon atom vacancies on both edges (see Fig. 2.6). Depending on the vacancy positions and density, the cove-edged GNRs can be semiconducting or nearly metallic (with a tiny gap) within the local spin-density functional approximation (DFT-LSDA). We consider here a prototypical family of cove-edged GNRs where one carbon vacancy and one hexagonal carbon ring alternatively occur along each edge. Among all possible cove-edged GNRs, this family gives the smallest unit cell size along the 1D periodic direction and has been recently synthesized by the bottom-up process [68]. This family of short-period cove-edged GNRs can be further categorized into three types–determined by its width specified by N (the number of zigzag chains forming the width of the parent zigzag ribbon) and the relative positions of the vacancies placed across the opposite edges (Fig. 2.6). For N = odd, there is only one type of structure [68] (see Fig. 2.6a) In contrast, when N = even, there are two distinct types of structures: the carbon vacancies on the opposite edges can either be directly facing each other (named N = symmetric-even) or be staggered (named N = asymmetric-even) as depicted in panels b and c, respectively, of Fig. 2.6.

The fully relaxed atomic structures of free-standing cove-edged GNRs show that the hexagonal carbon rings on the edges (Fig. 2.6a) are either tilted upward (pink) or downward (blue) from the GNR plane. This is because the edge carbon atoms are passivated by hydrogen atoms, as in the experimental bottom-up samples, and the steric hindrance between neighboring hydrogen atoms leads to an out-of-plane bending of the edge carbon rings. For the N = 5 cove-edged GNR in Fig. 2.6a, the edge carbon atoms have a maximum height of $\pm 1.2$ Angstrom from the center plane in our DFT calculations. We did not find any spin polarization at the DFT-LSDA level for the cove-edged GNRs studied, even though the parent zigzag GNRs have spin-polarized edge states.

The short-period cove-edged GNRs of types N = odd and N = symmetric-even have sizable DFT-LSDA energy gaps that increase as the GNR gets narrower. By contrast, the cove-edged GNRs of type N = asymmetric-even show almost zero band gap regardless of its width. Comparing between the two types of N = even cove-edged GNRs, shifting of the vacancy positions on one edge relative to those on the other edge gives rise to dramatically different electronic structures. As shown in the DFT-LSDA band structure of the N = 6-asymmetric cove-edged GNR (lower panel of Fig. 2.6c), the linear band dispersion near the Fermi energy that originates from the Dirac-like band dispersion at the K point of graphene folds to the zone center of the 1D BZ. This feature of the band structure for N = asymmetric-even survives in our LSDA and fully relativistic calculations including spin-orbit interaction.

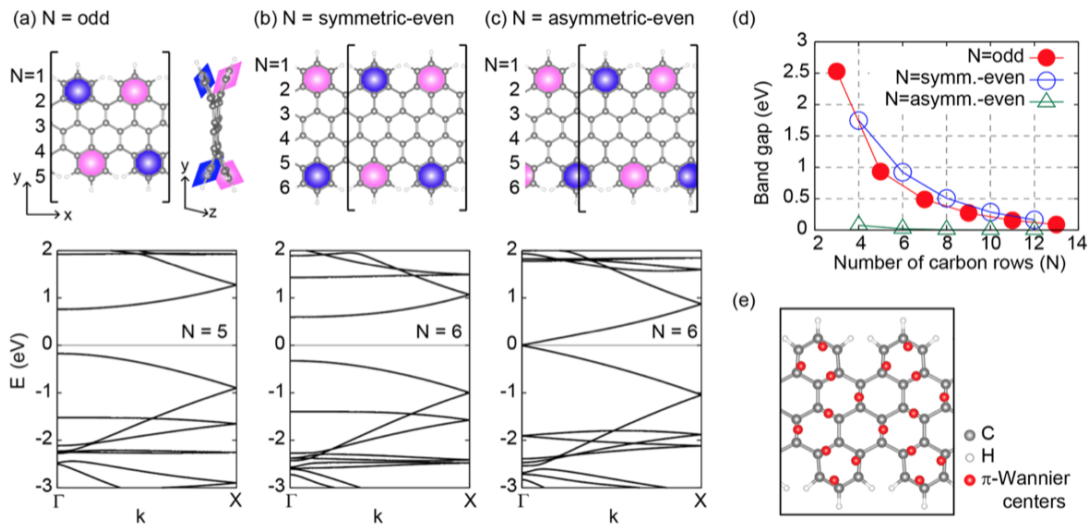


Figure 2.6: Schematic structures (top panels) and band structures calculated using DFT-LSDA (bottom panels) of short period cove-edged GNRs of (a) N = 5 (odd), (b) N = 6 (even) with symmetric edges (aligned facing vacancies), and (c) N = 6 (even) with asymmetric edges (misaligned facing vacancies) across the ribbon. The cove-edged GNRs are periodic along the x direction, and the side view in (a) illustrates the structural deformation along the direction perpendicular to the GNR plane. The unit cell of each GNR studied is shown by the black bracket. The gray and silver balls denote carbon and hydrogen atoms, respectively. The pink and blue areas denote edge carbon rings tilting upward and downward from the ribbon plane, respectively. (d) DFT-LSDA band gap of the three types of cove-edged GNRs in (a)-(c). For N = asymmetric-even cove-edged GNRs, the DFT-LSDA band gap is close to 0. (e) Wannier centers of the $\pi$-electron Wannier functions of an N = 5 cove-edged GNR are denoted by red dots in the unit cell.

We calculate the values of the $Z_2$ invariant for various short-period cove-edged GNRs using the tight-binding model for the $p_z$ $\pi$ orbitals in the GNR systems. The $Z_2$ invariants (Table 2.2) depend on their widths and the choice of unit cells. We use the nomenclatures established above to present and categorize the topological phases of these cove-edged GNRs. For cove-edged GNR with N = odd and N = symmetric-even, we select six representative unit cells (commensurate to different structural terminations of the ribbon) that have inversion and/or mirror symmetry. For N = odd cove-edged GNRs, unit cells with armchair and armchair' cell boundary shapes have trivial and nontrivial topological phases, respectively, regardless of the GNR widths. In comparison, for the other four types of cell boundary shapes (zigzag, zigzag', bearded, and bearded') considered, the $Z_2$ invariant for the N = odd cover-edged GNRs changes cyclically with a periodic of 8 on N (see Table 2.2). For example, for N = 8p + 5

(p is an integer), such a cove-edged GNR can have all the six cell boundary shapes. The armchair and armchair' shapes lead to $Z_2 = 0$ and 1, respectively. For the other unit cell boundary shapes, a zigzag (zigzag') 60°-tilted unit cell has $Z_2 = 1$ (0), and a bearded (bearded') 120°-tilted unit cell has $Z_2 = 1$ (0). The $Z_2$ for all other N = odd cove-edged GNRs are similarly presented in the Table. For N = symmetric-even, spatial symmetry only exists in zigzag- (zigzag'-) shaped unit cells for N = 8p + 2 and 8p + 6, and in bearded- (bearded'-) shaped unit cells for N = 8p and 8p + 4. The zigzag- (zigzag'-) shaped boundaries result in $Z_2 = 0$ (1) for N = 8p + 2, and $Z_2 = 1$ (0) for N = 8p + 6. The bearded- (bearded'-) shaped boundaries have $Z_2 = 1$ (0) for N = 8p, and $Z_2 = 0$ (1) for N = 8p + 4. For N = asymmetric-even, the cove-edged GNRs are virtually gapless within DFT-LSDA; so, we do not consider their topological invariants in this study.

| Termination type | | Armchair | Armchair′ | Zigzag | Zigzag′ | Bearded | Bearded′ |
|---|---|---|---|---|---|---|---|
| Unit cell shape / N=width (*p* integer) | | 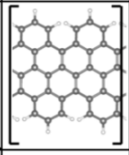 | 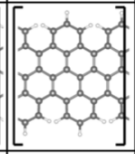 | 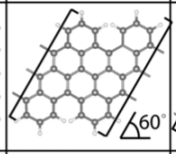 | 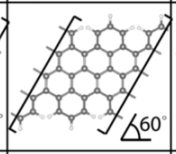 | 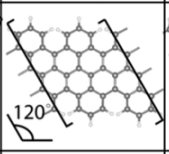 | 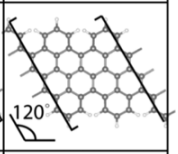 |
| odd | 8*p* + 1 | 0 | 1 | 0 | 1 | 0 | 1 |
| | 8*p* + 3 | 0 | 1 | 0 | 1 | 1 | 0 |
| | 8*p* + 5 | 0 | 1 | 1 | 0 | 1 | 0 |
| | 8*p* + 7 | 0 | 1 | 1 | 0 | 0 | 1 |
| even | 8*p* + 2 | N/A | | 0 | 1 | N/A | |
| | 8*p* + 6 | | | 1 | 0 | | |
| | 8*p* | | | N/A | | 1 | 0 |
| | 8*p* + 4 | | | | | 0 | 1 |

Table 2.2: Calculated values of $Z_2$ invariants of short-period cove-edged GNRs for different widths N (mod 8) and shape of the unit cells. Unit cell shapes studied are armchair, armchair', zigzag, zigzag', bearded, and bearded'. The atomic structure in the second row of the table is illustrated with an N = 5 cove-edged GNR, with gray and silver balls denoting carbon and hydrogen atoms, respectively. For N = odd, the unit cell boundary with a zigzag(') and bearded(') shapes forms a 60° and 120° angle with respect to the ribbon axis, respectively. For N = even, only the symmetric carbon vacancy structures which have sizable DFT-LSDA band gap are considered here. For unit cells with atomic structure that does not have spatial symmetry, the Zak phase is not quantized, so that a meaningful $Z_2$ invariant does not exist and this is denoted by "not applicable" (N/A).

Next, we investigate the electronic structure and $Z_2$ of the chevron GNRs [18, 17, 85]. The geometric structures of chevron GNRs are related to those of armchair GNRs.

Three specific kinds of chevron GNRs with different unit cell shapes are considered in this work: regular chevron GNR [18], extendedchevron GNR [85], and binaphthyl-chevron GNR [17] (Figure 2.7). They all have the narrowest width portions in the unit cell formed from N = 6 armchair GNR. These chevron GNRs have been recently synthesized through bottom-up self-assembly of molecular building blocks [18, 17, 85]. The extended-chevron GNR and binaphthyl-chevron GNR are laterally extended structures that can be viewed as a regular chevron GNR with additional hexagonal carbon rings and additional two rows of carbon in the elbow positions, respectively (see Fig. 2.7). The band structures of the three types of chevron GNRs are shown in Fig. 2.7. Their band gaps, evaluated by DFT-LDA, are 1.18 (binaphthyl), 1.37 (extended), and 1.59 (regular) eV. The band gaps of extended- and binaphthyl- chevron GNRs are smaller than their parent regular chevron GNR because increasing effectively the ribbon widths by the additional carbon atoms leads to weaker quantum confinement.

We have calculated the $Z_2$ invariants of these chevron GNRs for the two different unit cell shapes indicated in Fig. 2.7. For regular chevron and binaphthyl-chevron GNRs, $Z_2 = 0$ for the 60° or 120° unit cells with armchair shape at the unit cell boundary, and $Z_2 = 1$ for the 90° unit cells with zigzag shape at the unit cell boundary. However, extended-chevron GNRs with 60°, 90°, and 120° unit cells all belong to the topological trivial class (i.e. $Z_2 = 0$).

We next explore various GNR heterojunctions or finite segments that show junction states or end states, resulting from the topological nature of the electronic structure of their components. Guided by the values of $Z_2$ of GNRs with various widths and terminations, we construct a number of different GNR heterojunctions-consisting of combination of an N = 7 AGNR, an N = 5 cove-edged GNR, or a regular chevron GNR, at which two topologically equivalent or inequivalent segments are connected together. The emergence of topologically induced junction states for the latter class of junctions has been confirmed for all these structures.

Figure 2.8a shows two heterojunctions made from an N = 7 AGNR and an N = 5 cove-edged GNR with tilting angle of 30°. The two junctions are structurally different, corresponding to either (1) a zigzag ($Z_2 = 1$) termination or (2) a zigzag' ($Z_2 = 0$) termination of an N = 7 AGNR joining with a zigzag ($Z_2 = 1$) termination of an N = 5 cove-edged GNR. For case (2), as expected, a topologically induced junction state emerges and is localized at the interface between the two topologically inequivalent segments (the zigzag'-terminated N = 7 AGNR and zigzag-terminated N = 5 cove-edged GNR junction). In comparison, there is no in-gap state in case (1), the heterojunction formed between the zigzag-terminated N = 7 AGNR and zigzag-terminated N = 5 cove-edged GNR. Figure 2.8b depicts that an N = 7 AGNR/regular chevron GNR heterojunction can also be formed in two different configurations. Again, by bulk-edge correspondence (in presence of an approximate chiral symmetry in the charge neutral gap), a topological junction state arises at the zigzag'-terminated N = 7 AGNR/zigzagterminated chevron GNR junction; however, in the other case of zigzag-terminated N = 7 AGNR/zigzag-terminated chevron GNR junction, there is no in-gap state. The square of wave function of the junction states from DFT-LDA, integrated

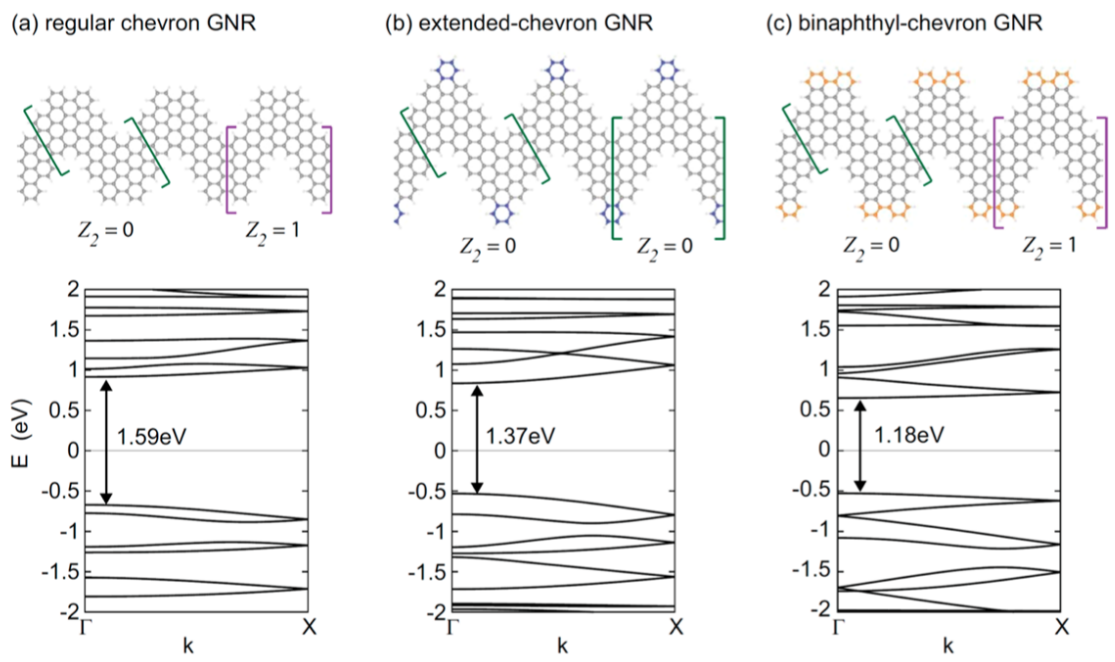


Figure 2.7: Schematic structures (top) and DFT-LDA band structures (bottom) of (a) regular chevron, (b) extended-chevron, and (c) binaphthylchevron GNRs. Gray and silver balls denote carbon and hydrogen atoms, respectively. The structures of extended- and binaphthyl-chevron GNRs are laterally extensions of a regular chevron GNR with additional hexagonal carbon rings (blue) and additional two rows of carbon (orange) in the elbow positions, respectively. They all have the narrowest width portions in the unit cell formed from N = 6 armchair GNR. The green and purple brackets show the unit cell shapes corresponding to topologically trivial and nontrivial phases ( $Z_2 = 0$ and 1), respectively. The DFT-LDA band structures show a semiconducting gap of 1.59, 1.37, and 1.18 eV in regular chevron, extended-chevron, and binaphthyl-chevron GNRs, respectively.

over the direction perpendicular to the ribbon plane [in units of $1/(a.u.)^2$ ], are shown in the bottom panel of Fig. 2.8a,b. Figure 2.8c,d show the DFT-LDA density of states (DOS) of the two systems, where a broadening of 0.03 eV is used. Because we have a finite length for each of the GNR segments in the calculation, the DOS from the bulk regions away from the junction does not dominate so that the junction states are visible in the DOS plot.

Our calculations show that the bulk bands of the N = 7 AGNR/N = 5 cove-edged GNR heterojunctions (for both cases in Fig. 2.8a) are aligned in the form of a type-I heterojunction. The energy band gaps within DFT-LDA of the individual N = 7 AGNR and the N = 5 cove-edged GNR are 1.6 and 0.93 eV, respectively. The type-I band alignment gives the wave functions of the low-energy conduction and valence

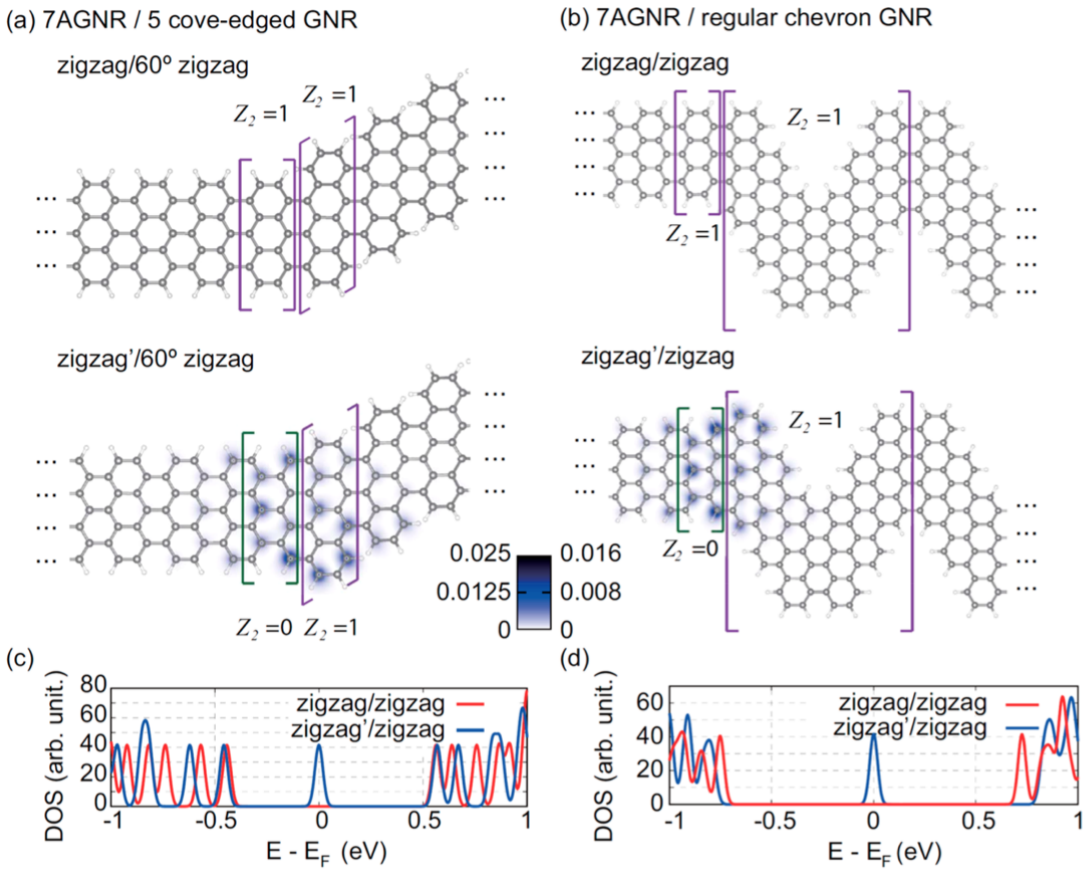


Figure 2.8: GNR heterojunctions formed with (a) an N = 7 AGNR and an N = 5 cove-edged GNR (finite length of 7.94 nm), and (b) an N = 7 AGNR and a regular chevron GNR (superlattice with lattice constant a = 10.23 nm). The upper panel and lower panel in (a) and (b) show heterojunctions between two topologically equivalent segments (zigzag/zigzag interface) and inequivalent segments (zigzag'/zigzag interface), respectively. These are zoom-in schematic structures near the junctions. The gray and silver balls represent the carbon and hydrogen atoms, and the green (purple) brackets show the unit cell with $Z_2 = 0$ (1). The color scale shows the square of wave function of the topological junction states integrated over the direction perpendicular to the ribbon plane [in units of $1/(a.u.)^2$ ]. The density of states of (c) the N = 7 AGNR/N = 5 cove-edged GNR heterojunctions and (d) the N = 7 AGNR/chevron GNR heterojunctions, with zigzag/zigzag (red curves) and zigzag'/zigzag (blue curves) interfaces, where a broadening of 0.03 eV is used. Topologically induced junction states emerge at the zigzag'/zigzag interfaces.

band states away from the band gap of the combined systems (not counting the in-gap state) residing in the cove-edged GNR region, and the ones of the higher-energy states

are extended throughout the whole system. On the other hand, a regular chevron GNR has a DFT-LDA band gap of 1.59 eV, which is almost the same as that of the N = 7 AGNR. Our results show that the bulk band states of the N = 7 AGNR/regular chevron GNR heterojunction systems (for both cases in Fig. 2.8b) are all extended throughout the system (i.e., it is a type-I alignment between two semiconductors with nearly identical band gaps).

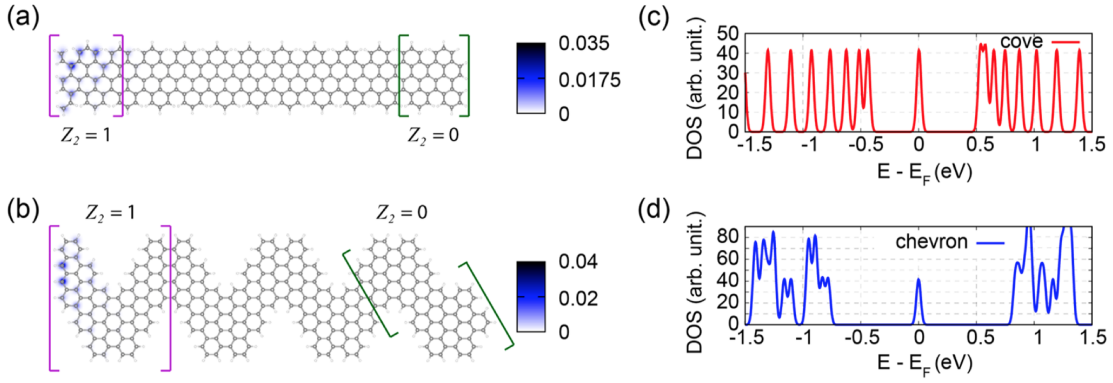


Figure 2.9: Finite GNR segments with different end terminations for (a) an N = 5 cove-edged GNR (a finite length of 6.21 nm) and (b) a regular chevron GNR (a finite length of 6.67 nm). Both isolated GNR segments consist of one end with $Z_2 = 1$ and the other end with $Z_2 = 0$. The gray and silver balls represent the carbon and hydrogen atoms, respectively, and the green (purple) bracket shows the unit cell with $Z_2 = 0$ (1) at a particular end. The color scale shows the charge density of the topologically induced end state at the end with $Z_2 = 1$. The charge density of the end state is integrated over the out-of-plane direction [in units of $1/(a.u.)^2$ ]. The density of states from DFT-LDA calculation of (c) cove-edged GNR segment and (d) chevron GNR segment with structures shown in (a) and (b) respectively are plotted, where an energy broadening of 0.03 eV is used. A 2-fold degenerate topologically induced end level appears at midgap (or at the Fermi level since it is half occupied) for both GNR segments.

As mentioned before, the value of the $Z_2$ invariant of a 1D system is related to how the end of the system terminates. Thus, we can design a finite GNR segment with different $Z_2$ at the two ends. We now consider the topologically induced end states of individual finite segments of N = 5 cove-edged GNRs and of regular chevron GNRs, for which one end has a terminating unit cell of $Z_2 = 0$ and the other end has a terminating unit cell of $Z_2 = 1$ (Fig. 2.9a,b). From bulk-edge correspondence in the charge neutral gap, an end state would arise at the end with $Z_2 = 1$ since vacuum is topologically trivial, and there would not be an end state at the other end with $Z_2 = 0$. Of course, at the end of a ribbon, it is also possible that localized states occur not from a difference in topological phases, but from a modification of the potential seen by the electron, such as broken chemical bonds, imperfection/distortion of the

carbon rings, etc. Even so, if the commensurate unit cell to a specific end structure is inversion/mirror symmetric, the total number of end states at the GNR-vacuum interface should follow the $Z_2$ invariant rule - an even or odd number of localized states at the end with $Z_2 = 0$ or $Z_2 = 1$, respectively. In Fig. 2.9, we illustrate the character of the topological end states for several such finite segments with plots of their wave functions from explicit DFT-LDA calculations.

We have also tested that the topologically induced junction and end states are robust against perturbations such as small displacements in atomic positions and/or changes in the atomic potentials (e.g., within tight-binding formalism, changes in the hopping integrals and onsite energies); these have been explicitly confirmed in our calculations for the systems studied. Since only the $\pi$ electrons are relevant to the topological phase of the GNRs, perturbations to the edge structure that retain the integrity of the band structure of the $\pi$-electron system should not change the junction or end states. However, since the topological invariants are determined by the spatial symmetry of the unit cell that is commensurate to the termination structure, a change in termination geometry for the $\pi$ electrons will change a segment's topological phase or making it ill-defined.

## 2.5 Topological phases in graphene nanoribbons tuned by electric fields

Having investigated the topological invariants of GNRs of various kinds of edge shapes, end terminations, widths and dopants, a natural direction to work on is to investigate the tunability of the topological invariants in GNRs by external applied fields or other tuning knobs. In this section, we show, through first-principles calculations, that by applying an experimentally accessible transverse electric field (TEF), certain boron and nitrogen periodically co-doped GNRs have tunable topological phases. The tunability arises from a field-induced band inversion due to an opposite response of the conduction- and valence-band states to the electric field. With a spatially-varying applied field, segments of GNRs of distinct topological phases are created, resulting in a field-programmable array of topological junction states, each may be occupied with charge or spin. Our findings not only show that electric field may be used as an easy tuning knob for topological phases in quasi-one-dimensional systems, but also provide new design principles for future GNR-based quantum electronic devices through their topological characters. This section is primarily adapted from Ref. [116].

Having the ability to controllably tune the topological invariants of materials is an actively pursued topic since it opens new opportunities for scientific studies and applications. Despite proposals on switching between normal and topological insulators (TIs) in 2D and 3D based on first-principles calculations, using external electric fields [69], tensile strains [28, 114], temperature and alloying [3, 75, 67, 1], and so on, strategies for tuning topological phases in 1D systems remain relatively underexplored. In

this work, by first-principles calculations, we discover that topological phases of certain quasi-1D systems may be practically tuned by a new strategy that exploits external TEF. We demonstrate this strategy using a designed GNR periodically co-doped with nitrogen and boron. [Fig. 2.10(a).]

In general, a transition from one topological phase to another one for an insulator requires its bandgap to close and reopen by external tuning parameters while preserving the symmetries desired. In our case, a TEF along the width of the GNR (the y-axis) [Fig. 2.10(a)] is used because it preserves both the approximate chiral symmetry in the GNR and the mirror symmetry of the GNR unit cell. (See section 2.5.1 below.)

As indicated by Eqn. (2.4), changing the $Z_2$ invariant by band reordering at the fundamental band gap requires the wavefunctions at the minimum of the bottom conduction band (BCB) and the maximum of the top valence band (TVB) to have opposite parities at one of the $\Gamma_i$ points, i.e., $\langle\psi_{BCB,\Gamma_i}|\,\hat{M}\,|\psi_{BCB,\Gamma_i}\rangle\,\langle\psi_{TVB,\Gamma_i}|\,\hat{M}\,|\psi_{TVB,\Gamma_i}\rangle = -1$. This ensures zero wavefunction mixing between the two states at this $\Gamma_i$ point of the BCB and TVB as a function of the TEF strength; so, a band gap closing is ensured during the induced band inversion process.

We satisfy this requirement by designing an armchair GNR (AGNR) with periodic arrays of substitutional boron-dimer and nitrogen-dimer dopants [Fig. 2.10(a)]. From our density functional theory (DFT) calculations, comparing results for an isolated boron-dimer to a nitrogen-dimer substitutionally doped onto the backbone of an AGNR shows that these two dimer defects introduce dopant states of opposite parity in the fundamental bandgap of the pristine AGNR. We therefore incorporate both boron- and nitrogen-dimer arrays into the same AGNR, and achieve having a boron-dimer (nitrogen-dimer) dopant band as its new BCB (TVB) with -1 (+1) parity eigenvalue at both $\Gamma$ and $X$.

Secondly, to make possible a field-induced band inversion, the BCB and TVB should have opposite energy shift in response to the applied TEF, requiring the wavefunction amplitude of BCB and TVB (and thus the GNR structure) to be asymmetric along the transverse (width-wise) direction of the GNR. Thus, we put the boron- and nitrogen-dimer dopants near the opposite edges of the AGNR [Fig. 2.10(a)].

The boron- and nitrogen-dimer dopants are symmetric to a mirror plane (red dashed vertical line in Fig. 2.10(a)) which retains the mirror symmetry of the system. In addition, in AGNRs with odd number of rows of atom forming the width, the boron- and nitrogen-dimer exchange positions upon a reflection with respect to the perpendicular plane at the central backbone, defined by the blue dashed line in Fig. 2.10(a). This ensures the system to have chiral symmetry within the nearest-neighbor tight-binding model, with and without the presence of the TEF. (See sections 2.5.2 and 2.5.3 below) Thus, the topology of the system can be classified by either a $Z_2$ index (using spatial symmetry) or a $Z$ index (using the approximate chiral symmetry).

Among a series of GNR structures designed, guided by the above design principles, an AGNR having 11 rows of carbon atoms with one boron-dimer dopant and one nitrogen-dimer dopant in every 3 pentacene units (abbreviated as B&N-11AGNR) [Fig. 2.10(a)] is found to have the desired properties for field-tunable topological phases. The

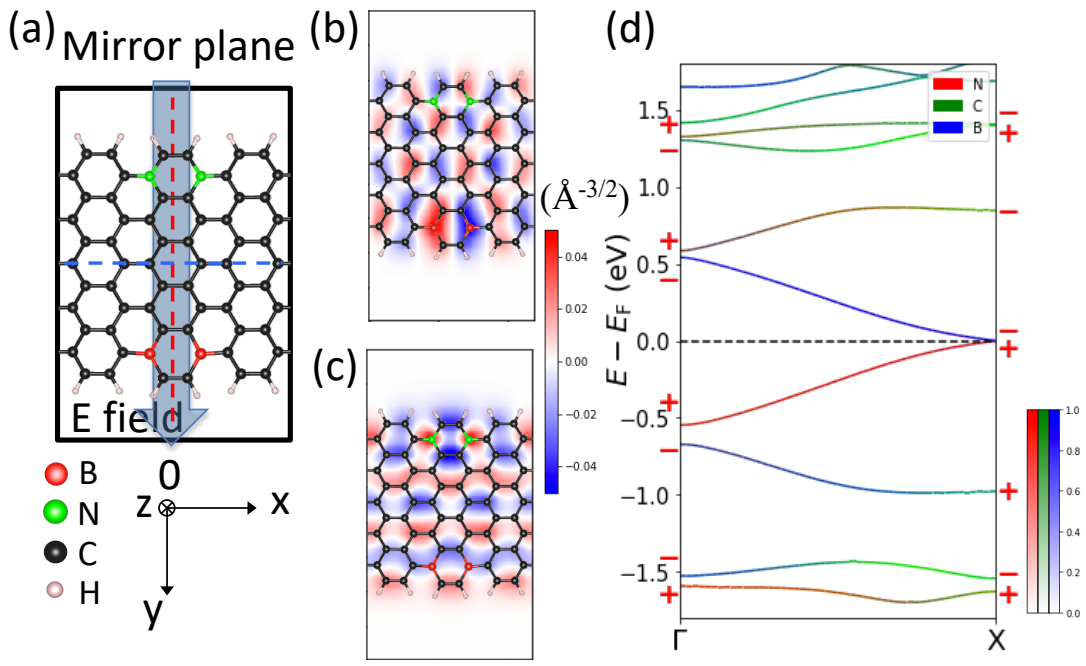


Figure 2.10: (a) A unit cell of the B&N-11AGNR (commensurate with a zigzag end termination). The blue arrow shows the direction of a positive TEF. The red dashed line shows a mirror plane of the system, and the blue dashed line defines a normal plane about which the positions of the boron- and nitrogen-dimers are switched upon reflection. (b, c) The BCB wavefunction (b) and TVB wavefunction (c) at the Γ point on a plane at 1 Angstrom above the GNR basal plane. (d) The B&N-11AGNR band structure without any applied field. The blue, red and green colors in the band structure denote the module squared weights of the wavefunction that are projected onto the boron, nitrogen and carbon atomic orbitals, respectively. The scale bar defines the mapping between the color scale and the percentage weight. The projection is normalized according to the total number of atoms of each species per unit cell. The parity eigenvalues $\langle\psi_{n\Gamma_i}|\,\hat{M}\,|\psi_{n\Gamma_i}\rangle$ of the 8 bands near the Fermi level $E_F$ at Γ and $X$ are marked as "+" ("-") for value of +1 (-1).

pristine B&N-11AGNR without any applied field has a direct band gap of $\sim 2.9$ meV, calculated using DFT within LDA as implemented in the QUANTUM ESPRESSO (QE) package [37]. This small gap (dictated by the ribbon width [101], density and exact positions of dopants) makes an electric-field-induced band inversion experimentally feasible.

The evolution of the DFT-LDA band structure with different applied TEFs [Fig. 2.11] is calculated using a supercell method that has a saw-tooth potential changing along the y direction and that accounts for dipole correction and depolarization field appropriately [9]. We find that band inversion at the X point happens at a critical

TEF (with positive direction defined in Fig. 2.10(a)) strength of $E_c \sim -0.2$ V/nm. For TEF with $E < E_c$, the orbital characters and parity eigenvalues of the bottom of the BCB and the top of the TVB at the X point switch with each other, giving rise to inverted bands. A wavefunction projection analysis shows that, for $E < E_c$, the orbital character of the band states, as a function of wavevector $k$, does recover to its original character at some distance away from the $X$ point [Fig. 2.11(c, d)]. From Eqn. (2.4), we obtain that the value of $Z_2$ changes from 1 to 0 as E goes below $E_c$. We also evaluate the $Z_2$ invariant and obtained the same result by calculating the center of the Wannier functions [12, 73, 99, 100] using the WANNIER90 package [76]. Moreover, we show that the DFT Hamiltonian for our system may be mapped approximately to a chiral Hamiltonian in a maximally localized Wannier function basis (see section 2.5.3), and that its $Z$ index changes from 1 to 0 as the E goes below $E_c$, consistent with the above $Z_2$ classification. Thus, the B&N-11AGNR satisfies all our designing principles and has a topological $Z_2$ invariant and a $Z$ invariant that are tunable with an experimental realizable TEF in the order of 0.1 V/nm.

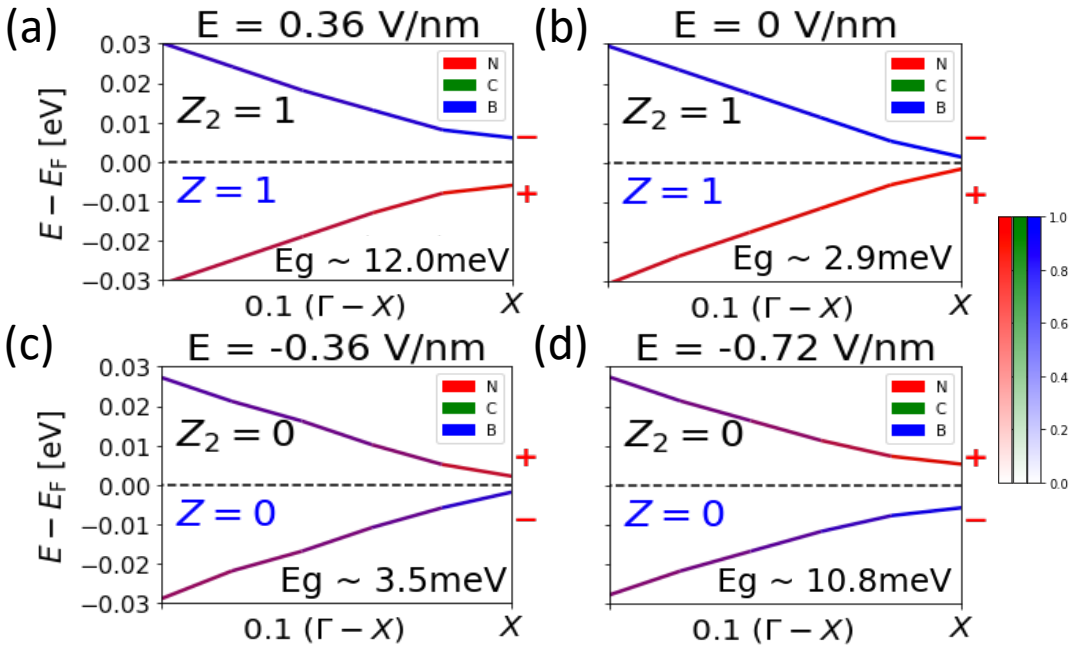


Figure 2.11: The band inversion process under changing TEFs from DFT-LDA calculations. As the TEF goes below a critical field strength of $E_c \sim -0.2$ V/nm, the characters (and parities) of the states of the BCB and TVB at the $X$ point are inverted, and both the $Z$ and $Z_2$ invariants of this system change from 1 to 0. The bands are zoomed in a region near the $X$ point in reciprocal space spanning over 1/10 of the $\Gamma - X$ length.

We next investigate the topological end states of a B&N-11AGNR finite-length

segment and the relation between the number of the end states and the value of $Z$, namely, the bulk-edge correspondence [86, 5]. We perform DFT calculation of the electronic structure of a finite-length B&N-11AGNR including 24 repeating unit cells of the form shown in Fig. 2.10(a), with the SIESTA package [98] using a limited single zeta atomic basis. All the dangling $\sigma$ bonds at the end of the ribbon (which is a zigzag termination) are capped by hydrogen atoms. The number of in-gap end states at one end in the charge neutrality gap as a function of the TEF strength and direction have three regions of distinct behavior [Fig. 2.12(e)]. For $E > E_c$, (with the critical field $E_c \sim -0.8$ V/nm for band inversion from the SIESTA calculation) one topological in-gap end state appears at each end, while for $E_s < E < E_c$, no in-gap end state emerges ($E_s \sim -1.8$ V/nm). For $E < E_s$, two localized states emerge in the band gap at each end. However, these two end states, unlike the topologically protected one in the case of $E > E_c$, can be eliminated by small perturbations on the end atoms (see section 2.5.4), so they are trivial end states. Thus, as expected, the bulk-edge correspondence holds in this system. The planewave basis set used in the QE calculation of the periodic system [Fig. 2.11] is well converged. However, for the finite segment SIESTA calculations [Fig. 2.12], a limited basis set was used (because of the large number of atoms), leading to less converged band gap values. This results in different values of $E_c$ and $E_s$ obtained by the two software packages. Nevertheless, the topological character of the bands of the two calculations remains the same.

From our theory, the TEF strength not only changes the number of end states, it also controls how localized the end states are. The local density of states (LDOS) at the end unit cell of the finite segment for 3 different TEFs [Fig. 2.12(a-c)] are compared with the bulk density of states (DOS) per unit cell. For E = 1.09 V/nm ($Z = 1$), the end-cell LDOS shows a sharp and big peak at $E - E_F = 0$, arising from a very localized in-gap state at each end [Fig. 2.12(a)]. A smaller bulk gap at E = 0 V/nm makes the end states less localized, resulting in a lower peak height at $E - E_F = 0$ [Fig. 2.12(b)]. For E = -1.09 V/nm ($Z = 0$), no in-gap peak emerges in the end-cell LDOS [Fig. 2.12(c)], showing absence of in-gap end state.

A field switchable topological phase enables the use of a spatially varying TEF to create and confine topological junction states between two insulating regions of different $Z$ invariants. To illustrate this effect, we apply a superlattice electric field (i.e., a periodically repeated pattern of TEF with a repeating unit profile shown in Fig. 2.13(a)) on a B&N-11AGNR as shown in Fig. 2.13(b). The TEF is negative (zero) in the left (right) half of the supercell, and has a form

$$E_y = \frac{E_0}{\pi}[arctan(x) - arctan(x - d_{sc}/2) - arctan(x + d_{sc}/2) - \pi/2], \qquad (2.33)$$

where the length of the supercell along the x direction is $d_{sc} = 305.2$ Å. A TEF of such pattern may be created by a periodic array of parallel gates with alternating bias voltages. For example, a topological junction state is confined at the junction between the left part with E = -1.58 V/nm and the right part with E = 0 V/nm ($E_0 = 1.58$ V/nm) [Fig. 2.13(b)] because the $Z$ invariant changes by 1 across the junction under

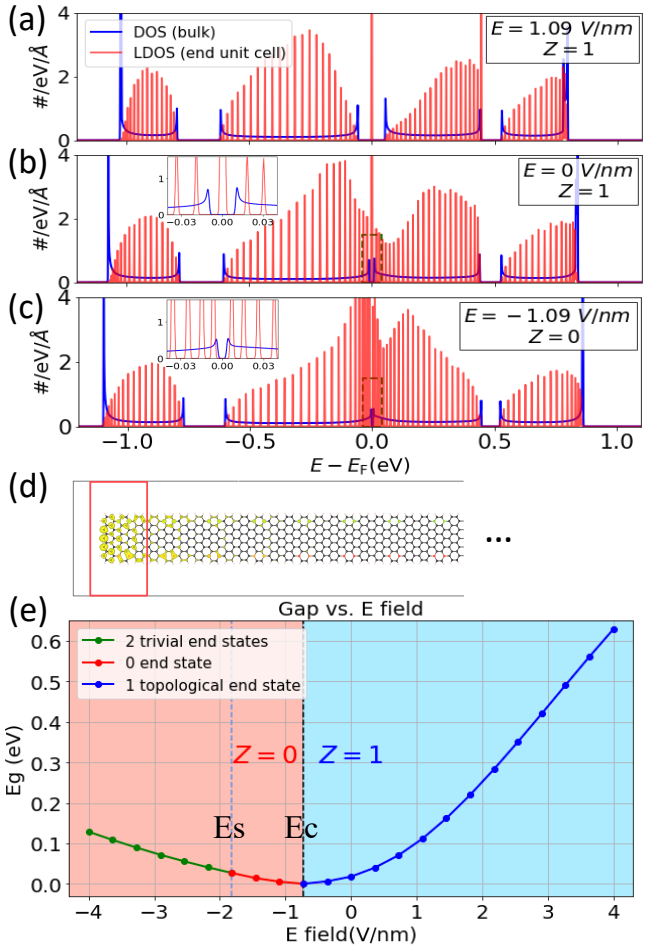


Figure 2.12: Bulk-edge correspondence. (a-c) The red curves show the calculated end-cell LDOS (integrated in the red rectangular region in (d)) of the 24-unit-cell finite-length GNR with TEF of E = 1.09 (a), 0 (b), and -1.09 (c) V/nm, while the blue curves show the bulk DOS per unit cell at the same TEFs. Both the LDOS and DOS are in units of number of states per energy per length without considering spin degeneracy. The Gaussian broadening factor is 1 meV for both the LDOS and bulk DOS. The insets zoom in the green dashed rectangular regions. (d) The iso-surface charge density plot at $1.4\times10^{-5}$ Å$^{-3}$ (1% of the maximum value) of the topological end state in the 24-unit-cell finite segment (only the left 1/3 of the segment is shown). The TEF is 1.09 V/nm ($Z = 1$). (e) DFT-LDA bandgap versus TEF calculated using the SIESTA package ($E_c \sim -0.8$ V/nm). The calculated $Z$ invariant is 1 (0) for $E > E_c$ ($E < E_c$). The colors on different parts of the curve denote the number of end states per end for the system.

this field profile. The two junctions in one supercell each hosts a protected junction state, which form 2 bands with small dispersions ($\sim$ 5 meV) inside the common gap of the left and right "bulk" region. Hence the LDOS of the unit cell at the junction (the red rectangle in Fig. 2.13(b)) shows two $\sim$ 5 meV wide peaks inside the common bulk gap [Fig. 2.13(c)]. In contrast to heterostructures made of geometrically different GNRs of distinct topological phases in which junction states appear at the junction [21, 65, 55, 90, 40], the topological junction states of the B&N-11AGNR are created by the profile of the TEF and can be moved freely to different locations in the material by varying the field profile. This gives us another degree of freedom in the rational control of topological junction states in 1D systems [21]. Furthermore, the coupling between two nearby localized states of the junction array, given by the junction separation, is programmable by the spatial profile of the field.

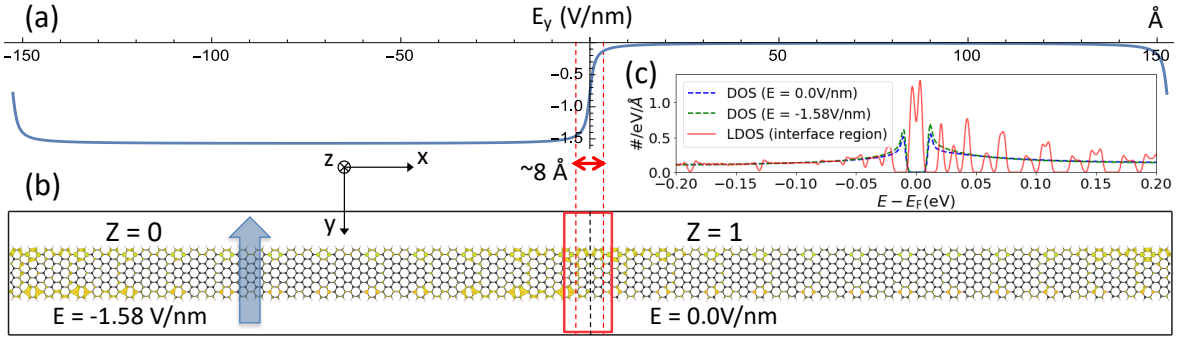


Figure 2.13: (a) The TEF profile in one repeating period as a function of coordinate x which is along the axis of the ribbon. (b) The iso-surface charge density plot at $2.7 \times 10^{-6}$ Å$^{-3}$ ( 2% of the maximum value) of the topological junction state (evaluated at $\Gamma$-point of the superlattice) of a B&N-11AGNR with the superlattice electric field in (a) applied. One repeating period of the TEF (the supercell shown in (b)) contains 24 B&N-11AGNR unit cells. The field strengths in the center of the left (right) region are -1.58 V/nm (0 V/nm) resulting in the system with $Z$ being 0 (1). (c) DOS of the GNR in a superlattice electric field. The red solid curve shows the LDOS computed in the junction region (the red rectangle in (b)). The green (blue) dashed curves show the bulk DOS per unit cell with a uniform TEF of E = -1.58 V/nm (0 V/nm).

In conclusion, we have proposed a scheme for designing GNRs with tunable topological phase by an applied TEF and demonstrated its feasibility through *ab initio* studies of GNRs. Our analyses and first-principles calculations show that topological end states can be created/annihilated by a uniform applied TEF on a GNR finite segment, and topological junction states can be generated in a homogeneous GNR by applying specific profile of piecewise uniform TEFs. Our study provides a new way of controlling topological junction/end states in 1D systems and is a promising new approach for designing future GNR-based quantum electronic devices.

### 2.5.1 Approximate chiral symmetry in boron-dimer and nitrogen-dimer periodically co-doped armchair graphene nanoribbon with 11 rows of carbon atoms (11AGNR)

We show here that chiral symmetry is satisfied to a very high degree even in the presence of the boron-dimer and nitrogen-dimer dopants in the AGNR as shown in Fig. 2.10. The $\pi$ electron bands in GNRs are formed by the $p_z$ orbitals of the carbon atoms, which are oriented perpendicular to the GNR basal plane. Given the overlap between the $p_z$ orbitals from adjacent carbon atoms is much larger than the overlap of that from next-nearest-neighbor carbon atoms, it is well-known and a common practice to use a nearest-neighbor tight-binding model to describe pristine graphene and GNR systems. As a result, the atomic orbitals of a GNR system can be divided in to A and B sublattices (Fig. 2.14(a)), such that no hopping is considered between any two orbitals belonging to the same sublattice. In this basis, grouping indices of all the atoms in A sublattice together to the upper left block of the Hamiltonian and taking the onsite energy of the carbon $p_z$ orbital as zero, the Hamiltonian of a pristine GNR reads:

$$H = \begin{pmatrix} 0 & H_{AB} \\ H_{AB}^{\dagger} & 0 \end{pmatrix}. \tag{2.34}$$

Defining a unitary operator:

$$\Gamma = \begin{pmatrix} I & 0 \\ 0 & -I \end{pmatrix}. \tag{2.35}$$

$H$ and $\Gamma$ satisfies Eqn. (2.5) and thus the Hamiltonian has chiral symmetry. A system with chiral symmetry has an energy spectrum symmetric to the charge neutrality point (defined as 0 energy) [5]. For any state with energy E, there is a chiral symmetric partner with energy –E. Any interactions beyond nearest neighbor would break the chiral symmetry in graphene; and previous density functional theory (DFT) calculations of general pristine GNRs show that the second-nearest-neighbor interaction and beyond are quite small. Thus, a pristine GNR has chiral symmetry to a high degree.

Now we argue that the boron-dimer and nitrogen-dimer periodically co-doped AGNRs of interest also have chiral symmetry, within a nearest-neighbor tight-binding model. In a tight-binding model, the orbital of the electron used in the basis is assumed to closely resemble the atomic orbital, and the onsite energy of the orbital $\langle i| H |i\rangle$, with $|i\rangle$ denoting the $i$th atomic orbital, is close to the ionization energy of the electron in a free atom. The ionization energy difference between nitrogen and carbon: $E_N^i - E_C^i = 3.27$ eV is quite close to that between carbon and boron: $E_C^i - E_B^i = 2.96$ eV. As a result, to a very good approximation, with the onsite energy of carbon taken

to be $\epsilon_C = 0$ eV, we may approximate the onsite energy of nitrogen and boron to be the same with opposite signs, i.e., $\epsilon_B = -\epsilon_N$. In the same spirit, the $p_z$ orbital from the carbon, nitrogen and boron atoms are assumed to be similar, leading to the same hopping integral for any two nearest-neighbor atoms: t = -2.7 eV. We note that any small deviations from the above model can be treated perturbatively as in previous analyses of chiral systems, since rigorously chiral symmetry in general is never strictly satisfied in physical systems.

For the boron-dimer and nitrogen-dimer co-doped 11AGNR (abbreviated as B& N-11AGNR) of interest here (see Fig. 2.10(a)), grouping the atomic orbitals into A and B sublattices as shown in Fig. 2.14 (b), the simplified tight-binding Hamiltonian reads (after rearranging the rows and columns so that the boron (nitrogen) atom in sublattice A has row/column index $i = 1(2)$, and correspondingly, the boron (nitrogen) atom in sublattice B has row/column index $i = N/2 + 1(N/2 + 2)$, where $N$ is the number of rows/columns which is equal to the total number of the carbon, nitrogen and boron atoms in the unit cell)

$$H = \begin{pmatrix} \epsilon_B & 0 & \cdots & & & \\ 0 & -\epsilon_B & \cdots & & H_{AB} & \\ \vdots & \vdots & \ddots & & & \\ & & & \epsilon_B & 0 & \cdots \\ & H_{AB}^\dagger & & 0 & -\epsilon_B & \cdots \\ & & & \vdots & \vdots & \ddots \end{pmatrix}. \tag{2.36}$$

In B&N-11AGNR, the boron and nitrogen dimers exchange positions upon a reflection with respect to the perpendicular plane at the central backbone, defined by the blue dashed line in Fig. 2.14 (b). We now define another unitary operator $U$ which is an index-exchanging operator for the indices of a pair of two atoms (which need not be identical) upon this reflection. For atoms on the central line, the U operator leaves the atom indices unchanged. The Hamiltonian $H' = UHU^\dagger$ describes a mirrored system with boron-dimer and nitrogen-dimer dopants interchanged with each other.

Applying $M = U\Gamma$ to $H$, we have:

$$MHM^\dagger = \begin{pmatrix} -\epsilon_B & 0 & \cdots & & & \\ 0 & \epsilon_B & \cdots & & -H_{AB} & \\ \vdots & \vdots & \ddots & & & \\ & & & -\epsilon_B & 0 & \cdots \\ & -H_{AB}^\dagger & & 0 & \epsilon_B & \cdots \\ & & & \vdots & \vdots & \ddots \end{pmatrix} = -H. \tag{2.37}$$

With $MM^\dagger = MM = I$. Hence, $M = U\Gamma$ is a chiral operator for the B&N-11AGNR system (or for any such B&N-AGNR with the dopant dimers similarly placed).

The boron- and nitrogen-dimer dopants also generate an electric polarization along the transverse direction (y direction). A self-consistent tight-binding model [66] could include this effect. If atom 1 and 2 (corresponding to the boron and nitrogen atom in the A sublattice, respectively, or two carbon atoms in the A sublattice) are located symmetrically with respect to the central line, combining the polarization field and the transverse electric field (TEF) add an extra term $\epsilon$ and $-\epsilon$ to the on-site energy of atom 1 and 2, respectively. Thus, they still have opposite values for their on-site energies. Within these considerations, Eqn. (2.37) always hold. As a result, we have shown that the B&N-11AGNR (or other such co-doped AGNR with odd number of rows) has chiral symmetry no matter whether a TEF is applied or not, by neglecting hopping beyond nearest neighbors and assuming the on-site energy of boron and nitrogen being of opposite values referenced to that of carbon. Our first-principles calculations show that the hopping terms beyond nearest neighbors, and other higher-order effects that might break the chiral symmetry, are negligible, indicating approximate chiral symmetry in real systems. This will further be demonstrated by mapping the first-principles Kohn-Sham Hamiltonian of this system in the $\pi$ electron manifold into a maximally localized Wannier function (MLWF) basis (Section 2.5.3).

### 2.5.2 $Z$ index invariant or winding number of B&N-11AGNR with zigzag termination: A simplified tight-binding model

We shall use the above tight-binding model to investigate the band inversion process and the change of the topological index $Z$ for B&N-11AGNR. The $Z$ index is a winding number whose value depends on the specific unit cell that is determined by the GNR's end termination of interest. This tight-binding model only has nonzero on-site energy for the $p_z$ orbitals on the boron and nitrogen atoms, and has the same nearest-neighbor hopping between any adjacent atoms. Its band structure with $\epsilon_B = -\epsilon_N = 7.2$ eV and $t = -2.7$ eV is shown in Fig. 2.15 (a). The band dispersion and the shape of the 4 bands near the charge neutrality gap are very similar to the DFT results (Fig. 2.10 (d)), and a wavefunction projection to various atomic orbitals shows that the lowest conduction band (highest valence band) is predominantly boron (nitrogen) dopant-state band. More importantly, the wavefunction symmetry of these 4 bands at the $\Gamma$ and $X$ points are the same as those calculated by DFT. Hence, this tight-binding model captures the important topological physics of the system.

Within the tight-binding formalism, the effects of TEF are mimicked by changing the on-site energy of boron and nitrogen, which are expected to be charged. A negative TEF as defined before will lower (elevate) the potential seen by an electron at the boron (nitrogen) sites.

As shown in Fig. 2.15 (b-d), using $\epsilon_B = 7.15$ eV, $\epsilon_B = 7.1$ eV, and $\epsilon_B = 7.05$ eV would give rise to results corresponding to the case in which $E > E_c$, $E \approx E_c$ ,and $E < E_c$, respectively. Here $E_c$ is the critical field at which the system changes its

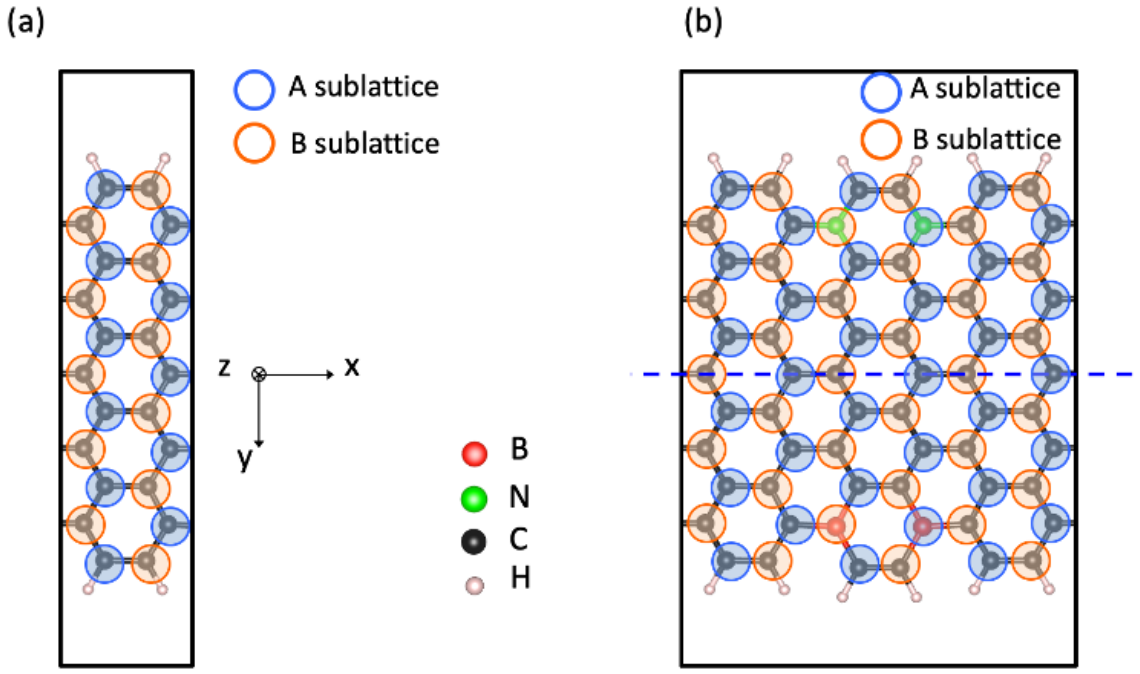


Figure 2.14: A and B sublattice in pristine and co-doped AGNR systems. In both (a) and (b), the atoms (carbon, boron or nitrogen) circled by blue and orange circles belong to A and B sublattices, respectively. (a) A pristine 11AGNR. (b) A B&N-11AGNR. The blue dashed line defines a normal plane about which the positions of the boron- and nitrogen-dimers are switched upon reflection.

topological phase. As discussed before, within a $Z_2$ classication (which is rigorously valid since our system possesses TRS and spatial symmetry), the calculated $Z_2$ invariant for the unit cell in Fig. 2.14(b), which corresponds to a zigzag end termination of the AGNR, is 1 (0) when $E > E_c$ ($E < E_c$). In the case $\epsilon_B = 7.1$ eV, the E field is just below $E_c$. As a result, the tight-binding model captures the band inversion process.

To calculate the $Z$ index within this tight-binding model, we transform the Hamiltonian $H$ in Eqn. (2.36) into the basis of eigenstates of the chiral operator $M$, and it becomes block off-diagonal.

$$H^{od}(k) = VH(k)V^{\dagger} = \begin{pmatrix} 0 & H_k \\ H_k^{\dagger} & 0 \end{pmatrix}, \tag{2.38}$$

where $V$ is the eigenvector matrix of $M$, and $k$ is the crystal wavevector (dimensionless). The chiral symmetry reduces some degrees of freedom of the Hamiltonian matrix, making it block off-diagonalizable in certain basis, so we could calculate the winding number using Eqn. ( 2.8).

As shown in Fig. 2.15 (e-g), $Z$ is equal to 1 (0) when $\epsilon_B = 7.15$ eV ($\epsilon_B = 7.05$ eV), which stands for the case where $E > E_c$ ($E < E_c$). $\epsilon_B = 7.10$ eV is the case where E is slightly below $E_c$. $E_c$ is the critical field value below which the trajectory of $det(h(k))$ does not enclose the origin and thus $Z$ changes from 1 to 0; so, $\epsilon_B = 7.10$ eV has $Z = 0$. From the simplified tight-binding model, which completely captures the band inversion process, we could deduce that the winding number $Z$ changed from 1 to 0 as the TEF goes below $E_c$ in B&N-11AGNR. The phase-transition-point for $Z$ and $Z_2$ occur both at the gap closing point.

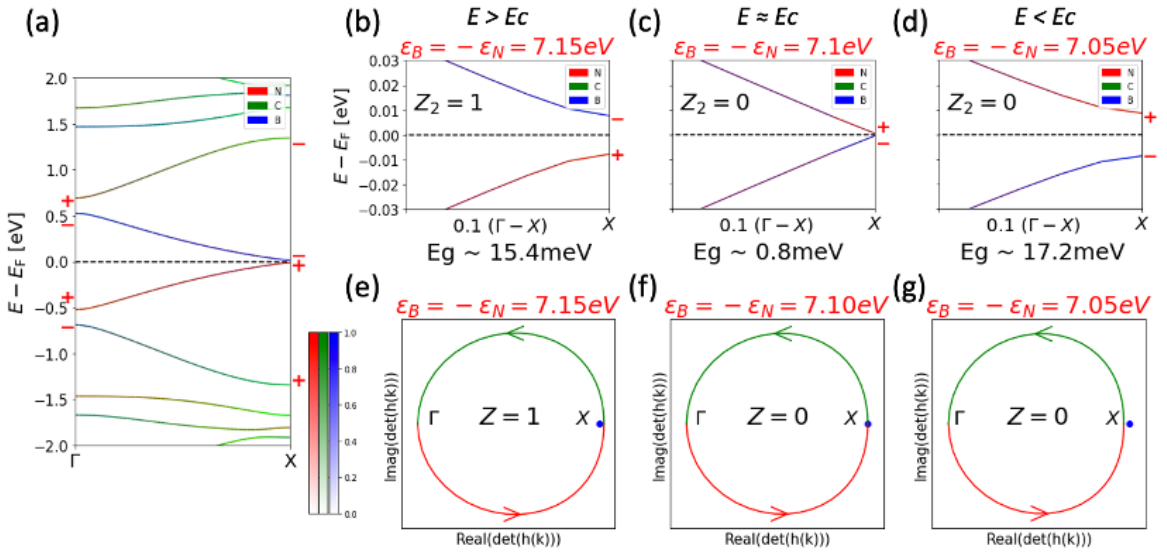


Figure 2.15: Calculation of Z index or winding number using the simplified tight-binding model. The parity eigenvalues $\langle\psi_{n\Gamma_i}|\,\hat{M}\,|\psi_{n\Gamma_i}\rangle$ of the high symmetry points are marked as "+" and "-" for value +1 and -1, respectively. (a) The band structure within the tight-binding model ($\epsilon_B = -\epsilon_N = 7.2$ eV,t=-2.7 eV). The blue, red and green colors in the band structure denote the module squared weight of the wavefunction that is projected onto boron, nitrogen, and carbon atomic orbitals, respectively. The projection has been normalized according to the total number of atoms of each species per unit cell. The scale bar defines the mapping between the color scale and the percentage weight. (b-d) The band inversion process in the simplified tight-binding model. The bands are plotted near the $X$ point in a reciprocal space spanning over 1/10 of the $\Gamma - X$ length. (e-f) The real and imaginary part of $det(h(k))$ as k moves across the 1D BZ. The red (green) curve shows the trajectory of $det(h(k))$ in the complex plane corresponding to $k$ going from $\Gamma$ to $X$ (from $X$ back to $\Gamma$), with the arrow showing the direction. The windings of $det(h(k))$ in the complex plane around the origin with the TEF above (e) and below (f, g) $E_c$ are 1 and 0, respectively, corresponding to $Z = 1$ and $Z = 0$.

### 2.5.3 $Z$ index invariant or winding number of B&N-11AGNR with zigzag termination: Hamiltonian in the maximally localized Wannier function basis

We now calculate the winding number from first-principles for the same unit cell as above, which corresponds to a zigzag end termination for B&N-11AGNR. Despite the absence of exact chiral symmetry, the self-consistent first-principles Hamiltonian at a specific TEF in the MLWF basis could be mapped to a system with exact chiral symmetry (chiral system) that closely resemble it, from which a winding number could be calculated. The values of the onsite energies and nearest-neighbor hopping terms of the chiral system should have least differences to those of the first-principles Hamiltonian in the MLWF basis.

We construct WFs from the manifold spanned by the $p_z$ orbital of carbon, boron and nitrogen atoms from first-principles calculations using the SIESTA software package with double zeta basis plus polarization orbitals [98]. The center of the $n$th WF is defined as $r_n = \langle 0,n|\,\hat{r}\,|0,n\rangle$, where $|0,n\rangle$ is the $n$th WF associated with the unit cell labeled by the 0th lattice vector. The centers of all of the MLWFs are shown in Fig. 2.16, with the radius of the circle proportional to the spread of the WFs $\Omega_n = \langle 0,n|\,\hat{r^2}\,|0,n\rangle - |\,\langle 0,n|\,\hat{r}\,|0,n\rangle\,|^2$. $\Omega_n$ are all less than 1.5 Å$^2$, indicating close resemblance to atomic orbitals in terms of localization. The WFs localized at the boron (nitrogen) atom positions have slightly larger (smaller) spread than that of the WF at the carbon atoms.

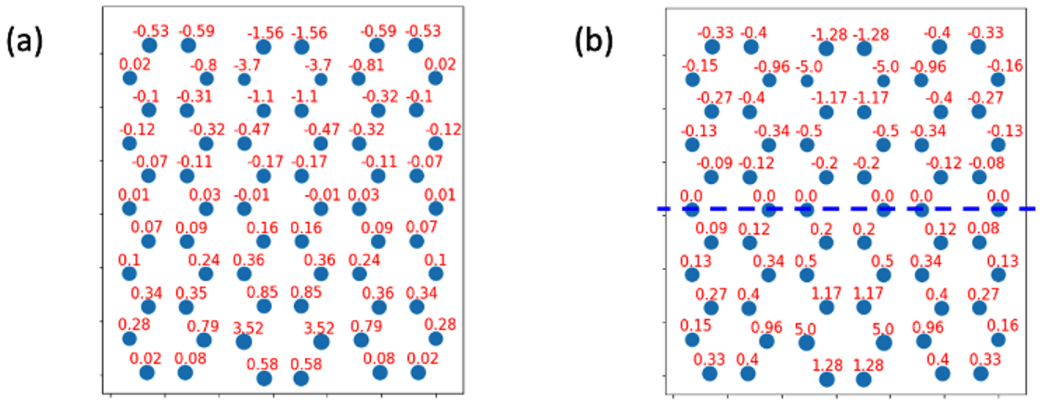


Figure 2.16: The positions of center of the MLWFs of B&N-11AGNR obtained from DFT calculations using the SIESTA package. The radius of the blue dots is proportional to the spread of the WFs. The numbers on each dot denote the onsite energy in the WF basis, while (a) is for the Kohn-Sham Hamiltonian and (b) is for the mapped chiral Hamiltonian. The blue dashed line in (b) is the normal plane about which the atomic sites switch positions upon reflection although the species of the atoms may not be the same.

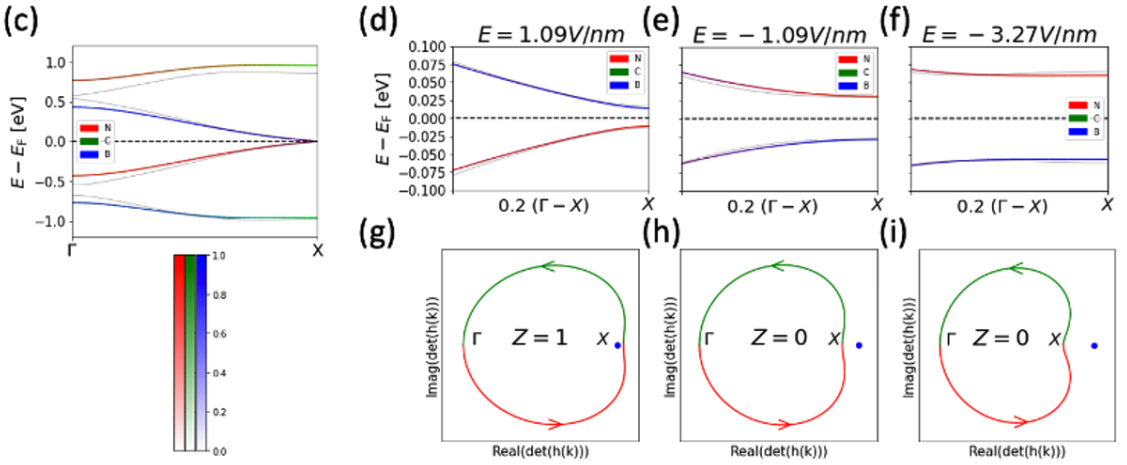


Figure 2.17: (Continued from Fig. 2.16) (c-f). The band structure of the mapped chiral system (colored line) and the Kohn-Sham system (grey line). The blue, red and green colors denote the module squared weight of the wavefunction that is projected onto WFs on boron, nitrogen and carbon atoms. The projection has been normalized according to the total number of WFs of each atom species per unit cell. The scale bar defines the mapping between the color scale and the percentage weight. (c) shows the band structure in the absence of applied field. (d-f) is the zoom-in band structure near the X point (spanning over 1/5 of the $\Gamma - X$ length) where the field-induced band inversion happens. Depicted are the band structures for E = 1.09 V/nm (d), -1.09 V/nm (e) and - 3.27 V/nm (f), which correspond to $E > E_c$ (d), $E_s < E < E_c$ (e) and $E < E_s$ (f), respectively. (g-i) The winding of the value of $det(h(k))$ of the mapped chiral Hamiltonian around the origin in the complex plane, corresponding to the case where E = 1.09 V/nm (g), -1.09 V/nm (h) and -3.27 V/nm (i). The red (green) curve shows the trajectory of $det(h(k))$ in the complex plane corresponding to $k$ going from $\Gamma$ to $X$ (from $X$ back to $\Gamma$), with the arrow showing the direction.

The MLWF basis are divided in to A and B sublattice entities in the manner as indicated in Fig. 2.14(b), according to their center positions. To map the system into a chiral system in the WF basis, we first eliminate all hopping terms that are beyond nearest-neighbor hopping. As a result, $\langle 0, m| \hat{H} |0, n\rangle$ is set to be 0 if the distance between centers of $|0, n\rangle$ and $|0, m\rangle$ is greater than the bond length ($\sim$ 1.5 Å). Secondly, WF centers are on the carbon, boron and nitrogen atom sites which exchange positions upon a reflection about a perpendicular plane at the central backbone shown in Fig. 2.16(b). The onsite energies for the WFs $\langle 0, n| \hat{H} |0, n\rangle$ that exchange positions upon

the reflection about this perpendicular plane are set to opposite numbers (Fig. 2.16(b)), while keeping the bandgap of the mapped chiral system the same as the original Kohn-Sham system. The onsite energies for the Kohn-Sham Hamiltonian $\langle 0,n|\,\hat{H}^{KS}\,|0,n\rangle$ (Fig. 2.16(a)) and those of the constructed Wannier chiral system $\langle 0,n|\,\hat{H}^{Chiral}\,|0,n\rangle$ (Fig. 2.16(b)) agree to within $\sim 0.3$ eV ($\sim 1.3$ eV) for the WFs on the carbon atoms (boron and nitrogen atoms).

The band structure of the original Kohn-Sham system of the B&N-11AGNR and that of our mapped chiral system, at different TEFs, agrees within $\sim 0.2$ eV for the 4 bands closest to the Fermi level $E_F$ (Fig. 2.17(c)), and the wavefunction characters of those bands for the Kohn-Sham system and the mapped chiral system are qualitatively the same. This indicates the changing of onsite energies and hopping terms beyond nearest neighbors qualitatively keeps the band properties of the Kohn-Sham system, which keeps its topological character. The winding number of the mapped chiral system with a unit cell commensurate to a zigzag end-termination for different TEFs are calculated to be: $Z = 1$ for $E > E_c$, and $Z = 0$ for $E < E_c$. Representatives of each of the cases where $E > E_c$, $E_s < E < E_c$, and $E < E_s$ are shown in Fig. 2.17 (d-i). Here $E_s$ is another critical field below which two localized end states emerge per end at the zigzag end termination of B&N-11AGNR. (See Fig. 2.12(e).)

### 2.5.4 Trivial end states when $E < E_s$ and the robustness of the topological end state when $E > E_c$

For the case $E < E_s$ ($Z = 0$), two end states inside the band gap are found for a B&N-11AGNR finite segment at each of the zigzag terminated end. However, we show that these end states are not protected and they can be pushed into the bulk continuum (and becomes delocalized) by applying some relatively weak perturbations on the onsite energies of the 5 outer-most carbon atoms at the end. For example, such perturbations are in the order of $\sim 0.5$ eV in the case of a TEF of E = -4.36 V/nm which has an energy gap of $\sim 0.2$ eV. As a result, the end states in this range of TEF are trivial end states.

For $E > E_c$ ($Z = 1$), the topologically protected end states on the other hand are extremely robust against perturbation on the end atoms. We find that the topological end state remains for perturbations up to at least $\sim 2.0$ eV in the case of TEF with E = 1.09 V/nm, which has an energy gap of $\sim 0.4$ eV.

The energy of the end states in the cases discussed above are calculated using a transfer matrix formalism [97]. Within this formalism, the local density of states of the end unit cell of a semi-infinite system of a B&N-11AGNR with zigzag terminations is calculated, and the Kohn-Sham Hamiltonian in the MLWFs basis is used.

For $E < E_s$, the energy of one of the 2 trivial end states in a semi-infinite system $E^1_{end}$ is close to the energy of the conduction band minimum (CBM), $E^{CBM}$, of the bulk, while the energy of the other $E^2_{end}$ is close to that of the valence band maximum (VBM), $E^{VBM}$, of the bulk. For TEF E = -4.36 V/nm, $|E^{CBM} - E^1_{end}| \sim |E^2_{end} - E^{VBM}| \sim 10$

meV, while the gap $|E^{CBM} - E^{VBM}| \sim 0.4$ eV. Thus, the end states could be pushed into bulk continuum under small perturbations. On the other hand, for TEF $E > E_c$, the one topological end state is in the middle of the energy gap, and it is extremely robust against perturbation on the end atoms.

## 2.6 Topological band engineering in graphene nanoribbon superlattices

In this section, we present an experimental and theoretical collaborative work. Thanks to the bottom-up synthesis technique, a 1D GNR superlattice formed by alternating segments of topologically distinct GNRs have been synthesized by our experimental collaborators. According to our theoretical prediction, an $N = 7$ ANR with zigzag$'$ termination has $Z_2 = 0$, while an $N = 9$ AGNR with zigzag termination has $Z_2 = 1$. In the atomically precise sythesized GNR superlattice, alternating N=7 AGNR zigzag$'$ segments and $N = 9$ AGNR zigzag segments forms interfaces through which the $Z_2$ invariant change by 1. As a result, a periodic array of topological interface states was formed in the 1D superlattice (Fig. 2.19(a) ). This section is primarily adapted from Ref. [90].

The 1D array of the topological interface states can further form two bands originated from electron topology inside the common gap of the two GNRs. If the coupling between these interface states is expressed as hopping amplitudes $t_1$ (for hopping across a 9-AGNR segment) and $t_2$ (for hopping across a 7-AGNR segment), then the band dispersion arising from the coupled topological interface states can be expressed in the standard two-band tight-binding form:

$$E_{\pm}(k) = \pm\sqrt{|t_1|^2 + |t_2|^2 + 2|t_1||t_2|cos(k)}. \tag{2.39}$$

This leads to a tunable energy gap ($E_g = 2||t_1| - |t_2||$ ) and bandwidth ($W = |t_1| + |t_2| - E_g/2$ ) for the new bands that arise from purely topological considerations.

The GNR superlattice shown in Fig. 2.19 was synthesized by the bottom-up techniques. It contains alternating segments of topologically distinct GNRs. The electronic structure of the GNR superlattice was measured by the scanning tunneling microscopy (STM). The $dI/dV$ curve was measured at the edge of the ribbon (blue and red cross in Fig. 2.18a ), which is proportional to the LDOS at such positions. The $dI/dV$ map measured at the peaks marked by A, B, C, D are shown in Fig. 2.18b. We have performed first-principles DFT calculations within the LDA. Figure 2.18d shows the theoretical bulk DOS for a freestanding 7/9-AGNR superlattice. A series of peaks arise from the superlattice band structure (Fig. 2.19c); these peaks are labelled the valence band (VB), the occupied topologically induced band (OTB), the unoccupied topologically induced band (UTB) and the conduction band (CB). The OTB and UTB are so named because they arise from the topologically induced interface states located

at each internal 7/9-AGNR heterojunction. The OTB and UTB features both have a double-peak structure in the DOS plot owing to the presence of two 1D Van Hove singularities in each band. The relative positions of these four bands correlate with peaks A–D, observed experimentally in the bulk region of a 7/9-AGNR superlattice as shown in Fig. 2.18a. Notably, the anomalously small band gap observed experimentally is nicely reproduced by the DFT calculations, which predict a gap of 0.52 eV (see band structure in Fig. 2.19c). It is not surprising that the theoretical value is smaller than the gap observed experimentally (0.74 eV) given that DFT tends to underestimate quasiparticle band gap, even accounting for the screening effects of the underlying Au substrate. Figure 2.18c shows that the theoretical LDOS maps at 4 Å above the plane of the 7/9-AGNR superlattice at energies corresponding to the VB, the OTB, the UTB and the CB. These LDOS maps are in excellent agreement with the experimental LDOS patterns shown in Fig. 2.18b. This agreement between *ab initio* theory and experiment confirms that peaks A–D observed in STS do indeed originate from the intrinsic VB, OTB, UTB and CB of the GNR superlattice.

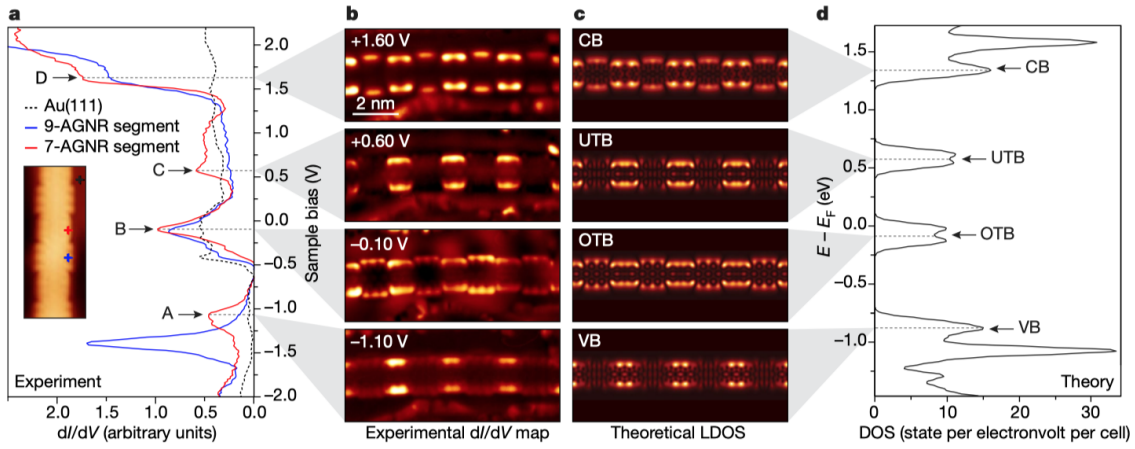


Figure 2.18: Electronic structure of 7/9-AGNR superlattice. (a) Inset, STM topography of 7/9-AGNR superlattice ($V_s$ = –0.10 V, $I_t$ = 80 pA). The red (blue) curve shows dI/dV point spectroscopy data collected on the 7-AGNR (9-AGNR) segment (tip position marked by plus sign). The dotted black curve shows a spectrum collected on bare Au(111). The spectroscopy parameters are $V_{ac}$ = 10 mV and f = 581 Hz. (b) Constantcurrent dI/dV maps obtained at voltages corresponding to peaks A, B, C and D marked by arrows in a ($I_t$ = 100 pA, $V_{ac}$ = 10 mV, f = 581 Hz). (c) LDOS maps calculated via DFT at the energies of the 7/9-AGNR superlattice VB, OTB, UTB and CB marked by arrows in (d) (obtained 4 Åabove the GNR plane). (d) Calculated DOS obtained via DFT for the 7/9AGNR superlattice (0.05 eV Gaussian broadening used). All STM data shown here were obtained at T = 4K on a 7/9-AGNR consisting of 12 fused monomer units (the total GNR length was 15.6 nm).

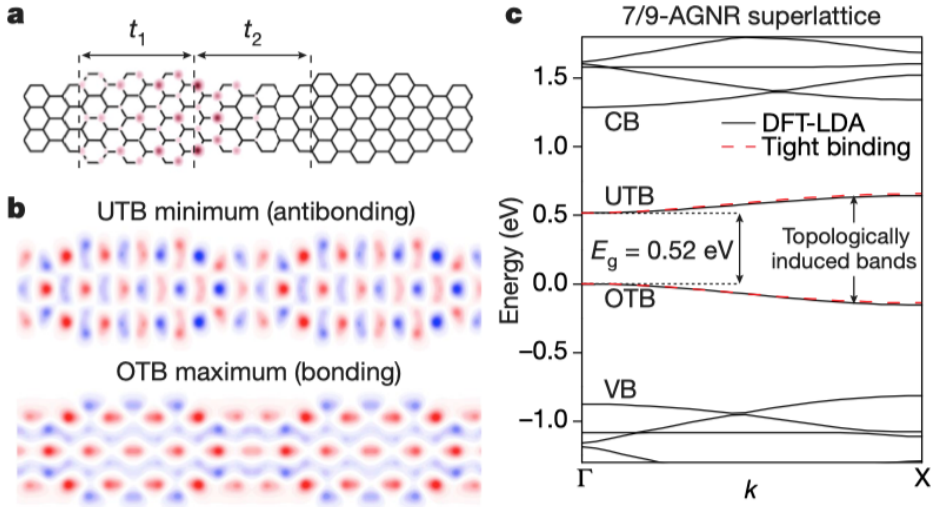


Figure 2.19: Topological bands in 7/9-AGNR superlattice. (a) Wireframe sketch of the 7/9-AGNR superlattice with superimposed charge density for only a single, isolated interface state. Arrows represent hopping amplitudes that couple interface states through different AGNR segments. (b) DFT–LDA wavefunctions for the OTB maximum and UTB minimum are composed of bonding and antibonding linear combinations of adjacent interface-state wavefunctions. The wavefunctions are plotted in the plane 1 Å above the GNR atomic plane to demonstrate bonding symmetry. (c) Solid black curves show the DFT-LDA band structure of a freestanding 7/9-AGNR superlattice. The dashed red curve shows a tight-binding fit to DFT OTB and UTB using equation 2.39.

## 2.7 Conclusion

In summary, we have discovered topological phases in GNRs, and calculated the topological invariants in GNRs of different edge shapes, end terminations, widths and different doping conditions. We have demonstrated from first-principles calculations that certain designed GNRs could have topological phases tunable by applied electric fields, and we have collaborated with experimentalists to confirm our theoretical prediction of novel topological bands from one-dimensional array of topological junction states formed by alternating segments of topologically distinct GNRs.

# Chapter 3

# Bulk-edge correspondence in $Z_2$ classification in quasi-1D systems

## 3.1 Introduction

In our investigation of the bulk-edge correspondence of the B&N-11AGNR (see previous chapter), we have found that the bulk-edge correspondence is violated in some energy gaps where the $Z_2$ invariant are well defined. For this system, because of its approximate chiral symmetry, bulk-edge correspondence still holds in the charge neutral gap, but it is violated in some other gaps since one cannot invoke chiral symmetry in analysis of other energy gaps in the band structure. In this chapter, we investigate in some detail about the bulk-edge correspondence of the $Z_2$ classification in quasi-1D systems. We find that the bulk-edge correspondence in the $Z_2$ classification is only absolutely guaranteed for the charge neutrality gap of systems with chiral symmetry. We use two simple model systems to illustrate violation of the bulk-edge correspondence in the $Z_2$ classification in quasi-1D systems.

## 3.2 Bulk-edge correspondence and $Z_2$ classification in a real GNR system

In the investigation of the topological end states of a B&N-11AGNR (see Chapter 2.5) finite-length segment and the relation between the number of end states and the value of $Z_2$ (the bulk-edge correspondence), we found that in some cases, there is no definite relation between the number of end states and the $Z_2$ invariant.

The bulk-edge correspondence for the $Z_2$ classification means that the number of end states per end of a finite-length segment formed by a system with $Z_2 = 1$ (0) at the energy gap of interest would be a odd (even) number. This was proved in Ref. [88], which shows that when the inter-cell part of the Zak phase is equal to $\pi$ (0) (mod $2\pi$), the number of end states per end of the finite segment formed by repeating such unit

cells is odd (even). The proof in Ref. [88] however relies on an argument that may not be valid in all possible cases.

In the analysis of Ref. [88], Wannier functions were constructed for a system with isolated band to calculate the accumulated charge in the end area of a finite-length segment which they use to determine the number of end states (Eqn. (19-24) in Ref. [88]). A specific gauge for the Wannier functions was used. For a Wannier function in a general gauge, Eqn. (19-24) in Ref. [88] does not hold since these equations are gauge dependent. In calculating the accumulated charge which is argued to be proportional to the number of end states, it is assumed exponential decay of the Wannier functions. But this is not guaranteed in the specific gauge of Wannier function chosen. As a result, the proof is not general and the bulk-edge correspondence of $Z_2$ classification in quasi-one-dimensional-system with spatial inversion/mirror symmetry and spinless time reversal symmetries is not proven. [96, 30, 57, 41, 6, 23]

In our study of B&N-11AGNR, we see a counter example to the bulk-edge correspondence of $Z_2$ classification at some gaps that are not the charge-neutrality gap. The calculated LDOS of the end unit cell (red box in Fig. 3.1 (b)) of a 24-unit-cell finite-length B&N-11AGNR is shown in Fig. 3.1 (c). The $Z_2$ invariants for gap 1 and gap 2 below the charge neutral gap (shown in Fig. 3.1) using the wavefunction symmetry at TRIM points (Eqn. 2.4) are 1 and 0, respectively. However, from the end unit cell LDOS, we see that the number of end states at one end inside gap 1 and 2 are 0 and 1, respectively. The number of end states in both gap 1 and 2 clearly violate the bulk-edge correspondence for the $Z_2$ classification. For the charge neutral gap, because of the approximate chiral symmetry, the bulk-edge correspondence holds.

We demonstrate in Section 3.3.1 that for a system with spatial inversion symmetry as well as the spinless TRS, if its Hamiltonian could be separated into two or more subspaces that do not or barely interact with each other, there exists energy gaps in which the bulk-edge correspondence is violated.

## 3.3 Violation of bulk-edge correspondence in some gaps in $Z_2$ classification of (quasi-) 1D systems

In this section, we give two simple model systems as counter-examples to bulk-edge correspondence of the $Z_2$ classification in the electronic band gaps of non-interacting quasi-1D systems with spatial inversion/mirror symmetry and TRS.

### 3.3.1 A 4-band model with nearest-neighbor interactions

We investigate a 4-band tight-binding model which is a system with 4 atomic orbitals per unit cell (shown in Fig. 3.2 (a) ). This system, with properly chosen hopping parameters, contains two barely interacting subsystems. We can make analogy between this constructed system to two polyacetylene chains parallel to each other. Each

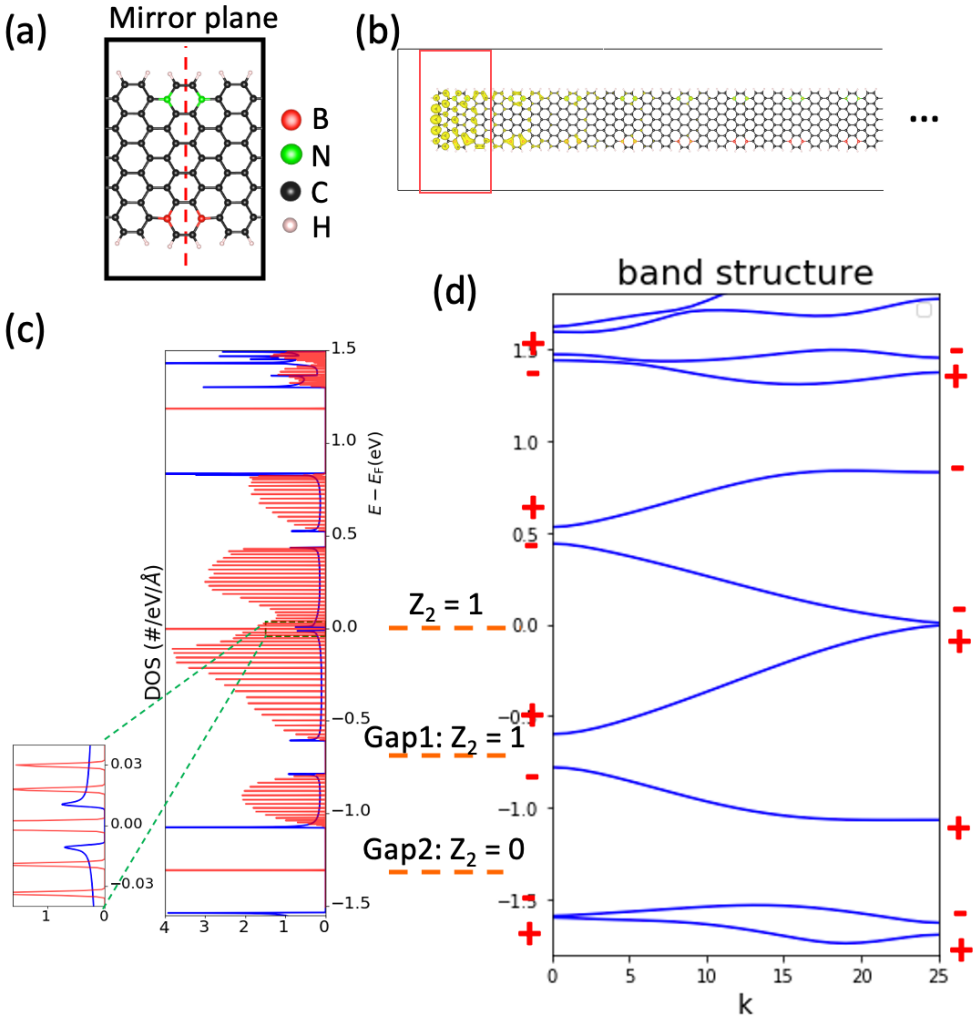


Figure 3.1: Bulk-edge correspondence violation in a practical GNR system. (a) A unit cell of the B&N-11AGNR (commensurate with a zigzag end termination). The red dashed line shows a mirror plane of the system. (b) The iso-surface charge density plot at $1.4 \times 10^{-5)}$ Å$^{-3}$ (1% of the maximum value) of the topological end state in the 24-unit-cell finite segment (only the left 1/3 of the segment is shown). (c) The red curves show the calculated end-cell LDOS (integrated in the red rectangular region in (b)) of the 24-unit-cell finite-length GNR, while the blue curves show the bulk DOS per unit cell. Both the LDOS and DOS are in units of number of states per energy per length without considering spin degeneracy. The Gaussian broadening factor is 1 meV for both the LDOS and bulk DOS. The insets zoom in the green dashed rectangular regions. (d) The B&N-11AGNR band structure without any applied field. The parity eigenvalues $\langle \psi_{n\Gamma_i} | \hat{M} | \psi_{n\Gamma_i} \rangle$ of the 8 bands near the Fermi level $E_F$ at $\Gamma$ and $X$ are marked as "+" ("-") for value of +1 (-1).

polyacetylene chain contains alternating weak and strong bonds (represented by single and double bonds in Fig. 3.2 (a) respectively), and we assume the interchain coupling exists for atomic orbitals that are nearest neighbors in different chains (i.e. $\langle i,1|\,H\,|i,3\rangle = s_1, \langle i,2|\,H\,|i,4\rangle = s_1$ where $|i,1\rangle, |i,2\rangle, |i,3\rangle, |i,4\rangle$ are atomic orbitals in the $i$-th unit cell).

We assume the nearest-neighbor hoppings inside the upper polyacetylene chain are : $\langle i,1|\,H\,|i,2\rangle = t_1, \langle i,2|\,H\,|i+1,1\rangle = t_2$, while the neighbor hoppings inside the lower polyacetylene chain are : $\langle i,3|\,H\,|i,4\rangle = t_3, \langle i,4|\,H\,|i+1,3\rangle = t_4$ (See Fig. 3.2(a).). In order to construct a system with two subspace with bands separated in energy when the interchain coupling is absent, we choose the magnitude of hoppings in the upper chain is at least an order of magnitude larger than that of the lower chain, i.e. $|t_1|, |t_2| >> |t_3|, |t_4|$. We also assume the upper chain terminates at its strong bond, while the lower chain terminates at its weak bond, so $|t_1| < |t_2|, |t_3| > |t_4|$. The unit cell of both the upper and lower chain (and the combination of them) have a mirror symmetry with the mirror plane bisecting the unit cell in the periodic direction. With obvious TRS present in the system, band gaps of both the upper and lower chain (and the combination of them) could be characterized by $Z_2$ invariants. Both chains (and the combination of them) also exhibit chiral symmetry and electron-hole symmetry (in absence or in present of the interchain coupling) as the lattice are bipartite and no hoppings beyond the nearest neighbor (See Section 2.5.1). In absence of the interchain coupling, for the one and only gap of each chain, the upper chain is topologically nontrivial ($Z_2 = 1$) while the lower chain is topologically trivial ($Z_2 = 0$), as calculated by Eqn. 2.4. The parity eigenvalues of the wavefunctions at the TRIM points are shown in Fig. 3.2(b). The band structure of the system with the interchain coupling $s_1 = 0$ and the hopping parameters $t_1 = 8$, $t_2 = 12$, $t_3 = 1.2$, $t_4 = 0.8$ eV are shown in Fig. 3.2(b). The two bands for the lower chain are both within the energy range of the gap formed by the two bands for the upper chain.

The topological nontrivial upper chain has one end state per end, and the end state appears in the center of the gap for the upper chain due to the presence of electron-hole symmetry. Thus, this end state appears in the center of gap 2 marked in Fig. 3.2(b) which is the common gap region for both chains. The topological trivial lower chain has no end state (according to our finite-length segment calculations, as well as a calculation of the LDOS in the end unit cell of a semi-infinite chain using the transfer matrix formalism [97]). As a result, there is no end state for the combination of the two non-interacting chains in gap 1 and 3 marked in Fig. 3.2(b), while there is one end state in gap 2.

However, the $Z_2$ invariants calculated for gap 1, 2, and 3 using Eqn. (2.4) (with and without interchain interactions) are all equal to 1, so there is a clearly violation of bulk-edge correspondence in gap 1 and 3, in which no end state presents with $Z_2 = 1$. Thus, we have shown a counter-example for the bulk-edge correspondence for the $Z_2$ classification in quasi-1D systems. For the noninteracting case, we have a simple explanation for this violation: Gap 1 and 3 (Fig. 3.2(b)) where the bulk-edge correspondence break are not real; they are formed by two subsystems that do not

talk to each other and the energy gaps happen to be located in the common energy forbidden region for both systems. The real energy gap for the upper chain is the combination of the three gaps plus the energy allowed region for the lower chain, and in this energy gap the bulk-edge correspondence holds: there is one end state. The energy gap for the lower chain is gap 2 (Fig. 3.2(b)), and the bulk-edge correspondence holds in absence of upper chain: there cannot be any end states in gap 2 in absence of the upper chain.

The case with interchain interaction is however physically important. To demonstrate this, we gradually increase the interchain coupling $s_1$ and see if there is a threshold $s_c$ such that when $|s_1| > |s_c|$, the bulk-edge correspondence restores in all the gaps of the combined system. We calculate the LDOS of the end unit cell (the dashed box in Fig. 3.2(a)) of a semi-infinite system with both polyacetylene chains interacting using the transfer matrix formalism [97]. The transfer matrix formalism includes the effects from the semi-infinite system exactly so it obtains the energy levels of the end states accurately, while a finite-length segment tight-binding calculation cannot eliminate finite size effect which may result in inaccurately calculated end states near band edges.

Figure 3.2 (c) shows the evolution of the band edges that define gap 3 and the energy levels of the end states if existing in gap 3 as a function of the magnitude of the interchain coupling $|s_1|$, with the parameters $t_1 = 8$, $t_2 = 12$, $t_3 = 1.2$, $t_4 = 0.8$ eV fixed. We see clearly that there is a threshold for $|s_1|$, above which an end state occurs in gap 3. When $|s_1| < |s_c| \approx 1.703$ eV, there is no end state in gap 3 and the bulk-edge correspondence is violated. When $|s_1| > |s_c|$, one end state appears in gap 3, thus the bulk-edge correspondence restores. From electron-hole symmetry of this system, we could infer that the bulk-edge correspondence also restores in gap 1 when $|s_1| > |s_c|$, which is confirmed by our explicit calculation as well.

For $0 < |s_1| < |s_c|$, the system is not two subsystems that do not interact to each other, but the bulk-edge correspondence still violates. In conclusion, we have shown the non-existence of bulk-edge correspondence in the $Z_2$ classification for arbitrary gaps in quasi 1D systems by this counter-example.

### 3.3.2 A 2-band model with 2nd and 3rd nearest neighbor interactions

We show another simple but interesting 2-band tight-binding model with hoppings beyond nearest neighbor in which the bulk-edge correspondence may be violated. This model is like a single polyacetylene chain with hoppings up to the third nearest neighbor. As shown by Fig. 3.3 (a) , there are 2 atomic sites with one orbital per site per unit cell, and the chain contains alternating weak and strong bonds. We assume that the hopping through the intercell (intracell) bond is $t_2$ ($t_1$). The magnitudes of the nearest-neighbor hoppings are further assumed to be proportional to the exponent of the bond length

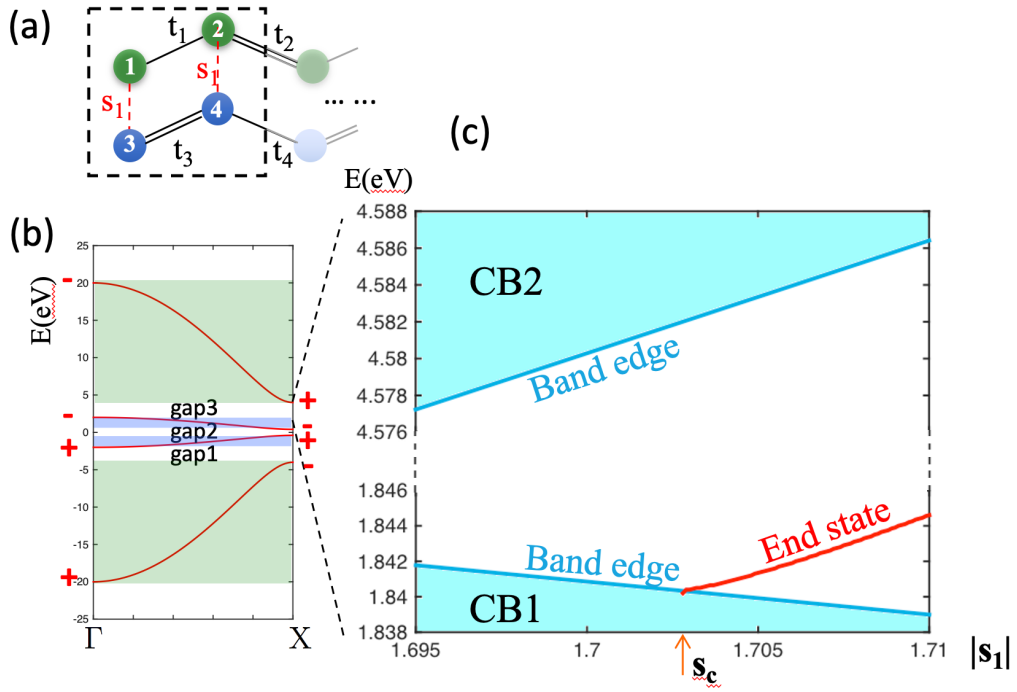


Figure 3.2: Bulk-edge correspondence violation in a 4-band system. (a) A tight binding model showing the tendency of a 4-band system towards being separated into two subsystems. (b) The band structure of the 4-band system with c. The the bands with blue and green shades are trivial and nontrivial bands, respectively. (c) The band edge that defines gap 3 and the end state in gap 3 in a semi-infinite chain as a function of the interchain coupling $|s_1|$. As $|s_1|$ goes below the critical value $s_c \sim 1.703$ eV, the end state merges into the bulk continuum and thus the bulk-edge correspondence is violated.

$$\frac{t_1}{t_2} = e^{(r_2 - r_1)/a}, \tag{3.1}$$

where $r_1$ and $r_2$ are the bond lengths for the weak and strong bond, respectively, and $a$ is the characteristic length for the exponentially decaying nearest neighbor hopping.

The second nearest-neighbor hopping through atomic orbitals $|i,1\rangle$ and $|i+1,1\rangle$ and that through $|i,2\rangle$ and $|i+1,2\rangle$ are assumed to be the same number, $s_2$, because the distance between $|i,1\rangle$ and $|i+1,1\rangle$ and the distance between $|i,2\rangle$ and $|i+1,2\rangle$ are same and all atomic orbitals in the system are assumed to be the same.

However, the third-nearest-neighbor hopping can be hoppings through $|i,1\rangle$ and $|i+1,2\rangle$ or that through $|i,2\rangle$ and $|i+2,1\rangle$, and the distance between $|i,1\rangle$ and

$|i+1,2\rangle$ and the distance between $|i,2\rangle$ and $|i+2,1\rangle$ are different. We denote

$$\langle i,1|\, H\, |i+1,2\rangle = s_3^1, \tag{3.2}$$
$$\langle i,2|\, H\, |i+2,1\rangle = s_3^2, \tag{3.3}$$

and take that the magnitude of hopping parameters is proportional to the exponent of the bond length

$$\frac{s_3^1}{s_2^2} = \frac{e^{-(2r_2+r_1)/a}}{e^{-(r_2+2r_1)/a}} = \frac{t_1}{t_2}. \tag{3.4}$$

We first investigate the bulk-edge correspondence in the one and only gap of the system when there is only nearest-neighbor and second-nearest-neighbor hopping. Figure 3.3(b) shows a phase diagram for the $Z_2$ invariant where the horizontal axis is the ratio between the magnitude of the two nearest-neighbor-hoppings $\frac{|t_2|}{|t_1|}$ and the vertical axis in the ratio between the magnitude of the second-nearest-neighbor hopping and the nearest-neighbor hopping of the strong bond $\frac{|s_2|}{|t_1|}$. For $\frac{|t_2|}{|t_1|} < 1$ ($\frac{|t_2|}{|t_1|} > 1$) and the system has a nonzero gap (Fig. 3.3(b)), the system has $Z_2 = 0$ ($Z_2 = 1$), and there is no end state (one end state per end) according to the calculated LDOS of the end unit cell of the semi-infinite chain by the transfer matrix formalism [97]. As a result, the bulk-edge correspondence holds for all cases in the absence of any third-nearest-neighbor hoppings in this model.

When we introduce the third-nearest-neighbor hopping, things are different. We plot a phase diagram for conditions over which bulk edge correspondence (BEC) holds in the ( $\frac{s_3^1}{|t_1|}$, $\frac{s_2}{|t_1|}$ ) parameter plane, while fixing the ratio $\frac{|t_2|}{|t_1|}$. The horizontal and vertical axis are the third-nearest-neighbor hopping $s_3^1$ and second-nearest-neighbor hopping $s_2$, made dimensionless by dividing the magnitude of the nearest-neighbor hopping $|t_1|$. We note that the ratio between $s_3^2$ and $s_3^1$ is always taken to satisfy Eqn. (3.4).

In Fig. 3.3(c,d), the gray regions are the parts of parameter space in which the system is gapless. In the parameter space where there is a finite gap, we calculate the LDOS of the end unit cell of the semi-infinite chain by the transfer matrix formalism and find that the bulk-edge correspondence is violated in the region marked red (Fig. 3.3(c,d)), and the bulk-edge correspondence holds in the region marked blue (Fig. 3.3(c,d)). In Fig. 3.3(c), $\frac{|t_2|}{|t_1|}$ is 0.9, and the calculated $Z_2$ invariant is 0 in the regime with nonzero gap. We find the system has no end state in the gap in the region marked blue, but the system has one end state in the gap in the region marked red and thus bulk-edge correspondence is violated. In Fig. 3.3(d), $\frac{|t_2|}{|t_1|}$ is 1.1, and our computed $Z_2$ invariant is 1 in the regime with nonzero gap. The system has one end state in the gap in the region marked blue, but there in no end state in the gap in the region marked red where the bulk-edge correspondence is violated. We note that the region where the bulk-edge correspondence is violated has either $s_2$ or $s_3^1$ ($s_3^2$) with similar magnitude as the nearest-neighbor hoppings. This hardly exists in a practical system,

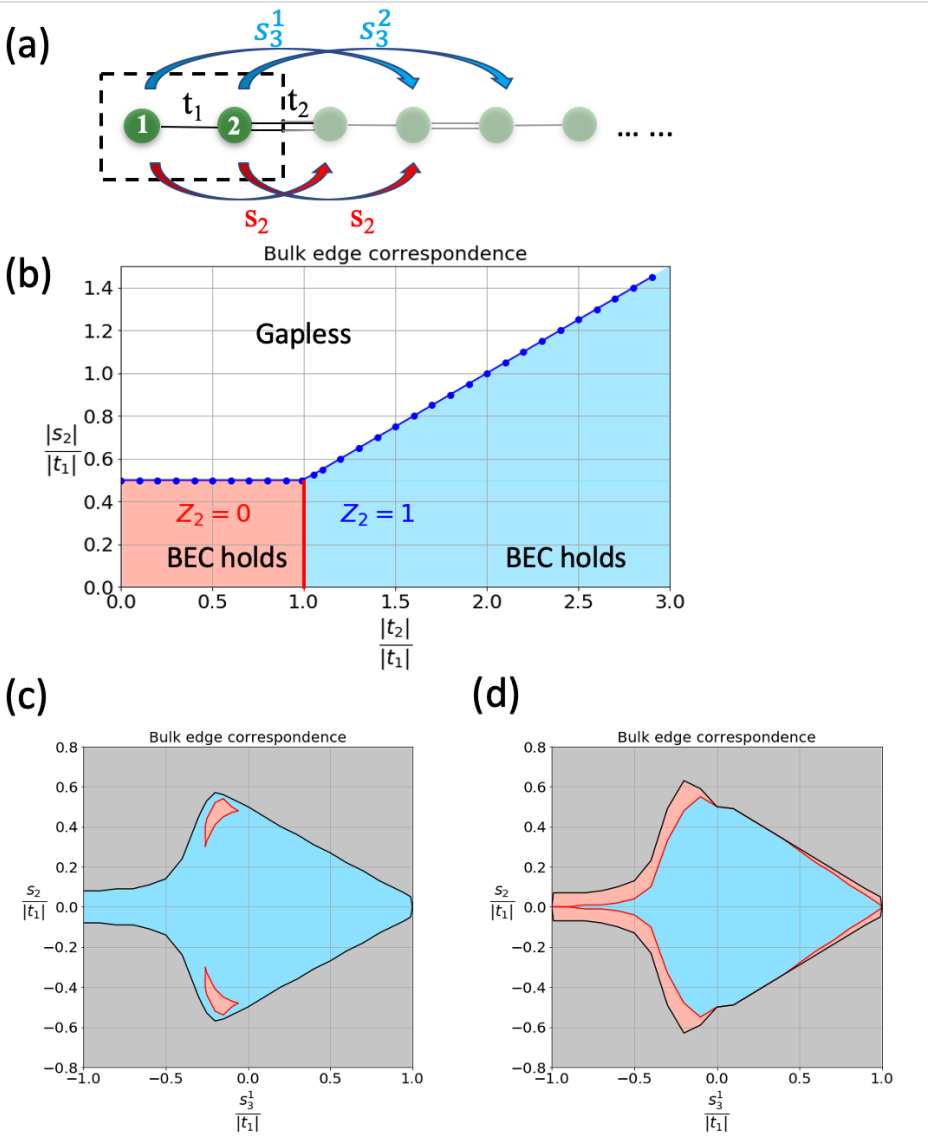


Figure 3.3: Bulk-edge correspondence (BEC) violation in a modified SSH model. (a) A SSH model with second- and third-nearest-neighbor hopping. (b) The phase diagram in the ($\frac{|t_2|}{|t_1|}$ , $\frac{|s_2|}{|t_1|}$ ) parameter plane, showing the bulk edge correspondence holds when only nearest-neighbor and second-nearest-neighbor hopping are present. (c, d) The phase diagram in the ( $\frac{s_3^1}{|t_1|}$, $\frac{s_2}{|t_1|}$ ) parameter plane. The red, blue, and grey region in the phase diagram denotes the regime where the bulk edge correspondence is violated, the regime where the bulk edge correspondence holds, and the regime where the system is gapless, respectively. (c) The phase diagram with $\frac{|t_2|}{|t_1|} = 0.9$ fixed. The $Z_2$ invariant of the system in the nonzero gap regime is 0. (d) The phase diagram with $\frac{|t_2|}{|t_1|} = 1.1$ fixed. The $Z_2$ invariant of the system in the nonzero gap regime is 1.

but it still provides a model system which violates the bulk-edge correspondence for $Z_2$ classification in quasi-1D systems. We note that in these regions chiral symmetry is also significantly broken.

In conclusion, we have provide two model systems as counter-examples of bulk-edge correspondence using $Z_2$ classification in quasi-1D systems. Thus, bulk-edge correspondence may not hold for some quasi-1D systems with spatial inversion/mirror symmetry and spinless TRS which can be characterized by a $Z_2$ invariant.

# Chapter 4

# Substrate interaction in boron-doped graphene nanoribbons

## 4.1 Introduction

In this chapter, we present a first-principles study of electronic properties of GNRs collaborated with the experimental groups. We present a study of the interaction between the gold substrate and the boron dopant states in a boron-doped AGNR sitting on top of the gold. This section is primarily adapted from Ref. [81].

## 4.2 Strong substrate interaction in boron-dimer-doped armchair graphene nanoribbons

Bottom-up fabrication techniques enable atomically precise integration of dopant atoms into the structure of GNRs. Such dopants exhibit perfect alignment within GNRs and behave differently from bulk semiconductor dopants. The effect of dopant concentration on the electronic structure of GNRs, however, remains unclear despite its importance in future electronics applications. In this section, we show our first-principles calculations study of the strong interaction between gold substrates and the dopant states in boron-dimer-doped AGNRs. First-principles calculations of freestanding GNRs predict that the inclusion of boron atoms in the form of dimers into a GNR backbone induces two sharp dopant states whose energy splitting varies with dopant concentration. Scanning tunneling spectroscopy experiments, however, reveal two broad dopant states with an energy splitting greater than expected. This anomalous behavior results from an unusual hybridization between the dimer dopant states and the Au(111) surface, with the dopant-surface interaction strength dictated by the dimer dopant orbital symmetry. First-principles calculations including the gold substrate atoms further explained the observed phenomena in the scanning tunneling spectroscopy experiments.

Here, we report the characterization of boron-dimer-doped N = 7 armchair GNRs (AGNRs) at two extreme doping regimes: the dilute and highly dense limits. Scanning tunneling spectroscopy (STS) measurements and density functional theory (DFT) calculations were performed to study the local electronic properties of boron-dimer-doped GNRs in both concentration regimes. Our calculations show that there exist two boron-dimer-induced dopant states in the gap, one with $s$-like (even parity) and the other with $p$-like (odd parity) orbital character that persist in both concentration limits. In the dilute limit our freestanding calculations (i.e., no substrate coupling) show that the boron-dimer-induced dopant states are nearly degenerate. As the density of dopant dimers increases in the freestanding regime, the energy separation between the boron dimer induced states increases, and the dimer dopant states form impurity bands since the dimer dopants are arranged periodically. The experimentally measured results, however, are not consistent with the freestanding GNR predictions. In the dilute limit, the experimental results show two dopant states with different symmetries that are strongly split in energy and broadened into asymmetric peaks(i.e., one is broader than the other). In the dense limit, the experimental upper dopant energy band is shifted in energy with respect to the freestanding theoretical prediction and is significantly broader than expected. This anomalous behavior is explained by hybridization between the boron-dimer-induced dopant states and the surface states of the gold substrate. First-principles calculations taking substrate coupling into account confirm that there is a strong and symmetry-dependent hybridization between GNR dopant states and Au(111). Consequently, as seen experimentally, this induces strong energy splitting and asymmetrical broadening whose magnitude depends on the dopant state symmetry.

Figure 4.1 shows a DFT calculation (using the LDA) of the electronic structure of a freestanding N = 7 AGNR (i.e., no substrate included in the calculation) for three boron dimer dopant concentrations: (i) the undoped case (Fig. 4.1d), (ii) the dilute doping limit (Fig. 4.1e), and (iii) the dense doping limit (Fig. 4.1f) (Fig. 4.1a-c show the unit cells used for the three calculations). The ground state of the freestanding boron-dimer-doped N = 7 AGNR in the dilute doping limit (Fig. 4.1e) is actually ferromagnetic [34] with a total magnetization of 2.00 $\mu_B$ per unit cell according to DFT calculation with a local spin density approximation (LSDA), but the magnetization would be suppressed due to a combined effect of $p$-doping and surface electric fields induced by the underlying Au(111) substrate [89], so the ferromagnetic ground state may not be seen experimentally for the boron-dimer-doped AGNR sitting on the gold substrate.

In the freestanding GNRs, GW calculations [26, 21, 50] were seen to give similar results but with larger band gap values due to self-energy effects. We focus here on the DFT results since substrate screening typically reduces the GW band gaps to values close to the DFT level when the system is put on a metallic surface (as done in the experiments here). The undoped GNR band structure shows the familiar conduction (CB) and valence (VB) bands that have been calculated within DFT before, [94] while the dilute-doped GNR exhibits bulk band edges at similar energies. The

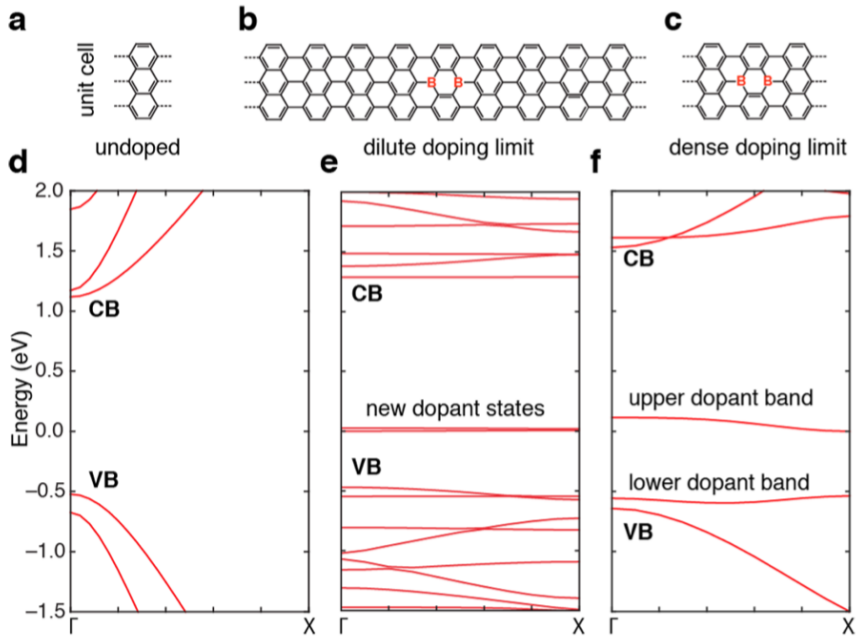


Figure 4.1: Band structure evolution of freestanding boron-dimer-doped N = 7 armchair graphene nanoribbons (AGNRs) at different dopant densities. Unit cells of (a) undoped, (b) dilute-doped, and (c) densely doped N = 7 GNRs. (d-f) Corresponding band structures calculated by DFT within LDA. The relative Brillouin zone sizes in panels d, e, f are 9 : 1 : 3, and when this is taken into account, the dispersion of the VB top and CB bottom does not change significantly after doping.

most significant difference between the undoped and dilute-doped band structure is the presence of two new defect levels at $\sim 0.5$ eV above the VB edge for the dilute-doped case (the appearance of multiple bands above (below) the conduction (valence) band edge for the dilute doped limit is due to band-folding from the supercell geometry used in the calculation). The new impurity states are nearly degenerate ($\Delta E < 20$ meV ) and exhibit a large contribution from the $\pi$-orbitals of the boron dopant dimers. Analysis of the wave function for the lower defect state shows that it has $p$-like symmetry (odd parity) along the GNR axial direction (Fig. 4.2 (b, c) ), while the upper defect state has $s$-like symmetry (even parity) (Fig. 4.2c) (a similar theoretical result for the dilute, freestanding limit was reported in Ref. [22]). As the dopant concentration increases, the energy splitting between the two impurity states correspondingly increases, and the defect states evolve into impurity bands with an energy gap of 0.5 eV, as shown in the band structure for the densely doped GNR in Fig. 4.1f (Fig. 4.3 shows the calculated band structures for other intermediate dopant densities) (the band labeling convention used here is different compared to a previous publication, Ref. [29], in order to make the role of the dopants more clear).

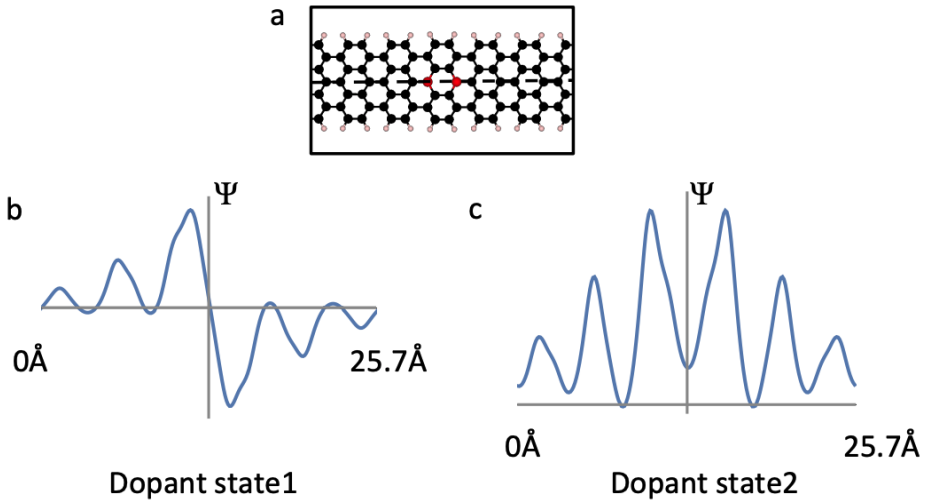


Figure 4.2: (a) The unit cell for a freestanding dilute boron-dimer-doped 7AGNR. Red, black, and purple spheres represent boron, carbon, and hydrogen atoms, respectively. (b, c) Calculated wavefunctions of the two dopant states at the Γ point for a freestanding GNR. The wavefunctions are plotted along the axial line of the unit cell in (a) (black dashed line) 1 Å above the GNR.

Figure 4.4b shows an STM topographic image of a resulting dilute-doped N = 7 GNR on Au(111) with vertical dashed lines indicating the location of a boron defect (a sketch of the wireframe structure is shown in Fig. 4.4a). The region surrounding the dopant dimers has a reduced apparent height in the STM image, suggesting that the boron dimers sit closer to the Au(111) surface than the GNR carbon atoms.

The experimental electronic structure of dilute-doped GNRs was investigated by measuring STM differential conductance (dI/dV) spectra at the position of boron dimer dopants and then comparing that to spectra acquired on undoped GNR segments at the positions marked in Fig. 4.4b (the respective positions are color-coded with the dI/dV curves). Figure 4.4c shows a characteristic dI/dV point spectrum (green curve) recorded at the edge of an undoped segment of the GNR. This spectrum exhibits a peak at $V_s = 1.68 \pm 0.02$ V, which is identified as the CB edge, as well as a peak at $V_s = -0.80 \pm 0.02$ V, which is identified as the VB edge ($V_s$ is sample voltage). This leads to an overall GNR bandgap of $2.48 \pm 0.02$ eV, similar to band gap measurements on undoped N = 7 AGNRs performed previously [26, 94, 61]. The identity of these familiar spectroscopic peaks was confirmed via energy-resolved dI/dV mapping, which allows visualization of the surface LDOS as depicted in Fig. 4.4d-g. Two new states attributed to the dopant dimers are observed in the STM spectroscopy measured at the center (top inset of Fig. 4.4c, blue curve) and edge (bottom inset of Fig. 4.4c, red curve) of the boron defect shown in Fig. 4.4b. The dI/dV spectrum measured

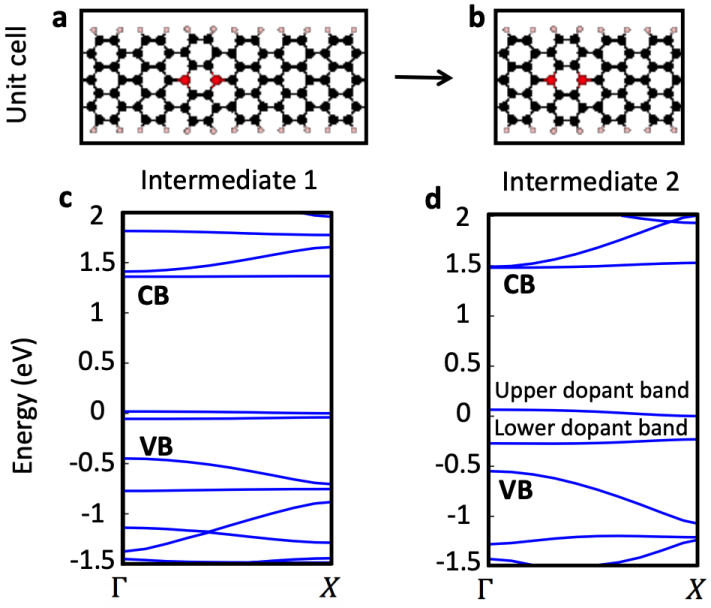


Figure 4.3: Band structures of freestanding boron-dimer-doped N=7 AGNR at two intermediate dopant concentrations. (a, b) Unit cells of freestanding N=7 AGNRs at two intermediate dopant concentrations 1 and 2, respectively. (c, d) Corresponding band structures calculated by DFT. The band gap for Intermediate 1 is 40 meV, and for Intermediate 2 is 230 meV.

at the impurity edge (red curve) shows the presence of a new peak (labeled State 1) that is centered at $V_s = -0.52 \pm 0.02$ V and that has a full width at half-maximum (fwhm) of 0.23 V. The dI/dV spectrum measured at the center of the dopant site (blue curve) exhibits a pronounced upward slope starting at $V_s \approx 0.3$ V and extending to $V_s \approx 1.2$ V that is not observed in the reference spectrum taken at the center of the undoped segment with the same tip (black curve). This second dopant-induced feature is labeled as State 2. These spectroscopic features (States 1 and 2) persist even as adjacent dopant dimers in the dilute regime have interimpurity distances as small as 2.5 nm center-to-center.

The spatial distributions of dopant-induced States 1 and 2 were determined using dI/dV mapping. Figure 4.4f shows a dI/dV map measured at the energy of State 1 that exhibits bright lines along the edges of the dopant segment as well as two small high intensity spots near the boron dimers (the two central bright spots are located at the sites of the two horizontal boron-carbon bonds). Figure 4.4e shows a representative dI/dV map of State 2 recorded at 0.8 V that exhibits bright, diffuse LDOS that is elliptically symmetric and centered at the position of the dopant dimers (dI/dV maps recorded for State 2 at different energies in the range $0.3V < V_s < 1.35V$ show similar

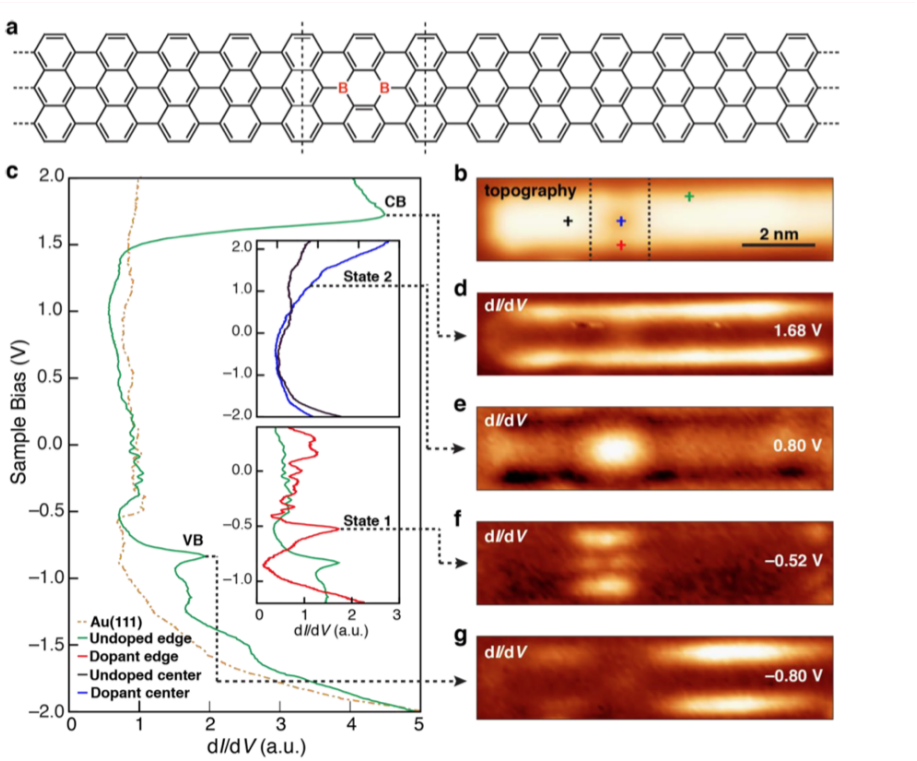


Figure 4.4: Electronic structure of a dilute boron-dimer-doped N = 7 AGNR on Au(111). (a) Wireframe sketch of a dilute-doped GNR. (b) STM topographic image of dilute-doped GNR ($V_s = -0.4$ V, $I_t = 60$ pA). (c) STM dI/dV spectroscopy measurement taken at the edge of an undoped segment of the GNR (green). Top inset shows dI/dV spectroscopy taken at the center of a boron dimer segment (blue) compared to the center of an undoped GNR segment (black). Bottom inset shows dI/dV spectroscopy taken at the edge of a boron-dimer-doped segment (red) compared to the edge of an undoped GNR segment (green). Two new states, dopant States 1 and 2, are observed at -0.52 and 0.8 eV, respectively. dI/dV maps of the GNR are shown at energies corresponding to (d) the CB edge ($V_s = 1.68$ V), (e) State 2 ($V_s = 0.8$ V), (f) State 1 ($V_s = -0.52$ V), and (g) the VB edge (the fact that the VB feature on the left side is darker is due to the asymmetrical defect placement, which likely increases quantum confinement effects on the left side) ($V_s = -0.8$ V). T = 7 K for all measurements. Panels d-g have the same scale as panel b.

LDOS patterns).

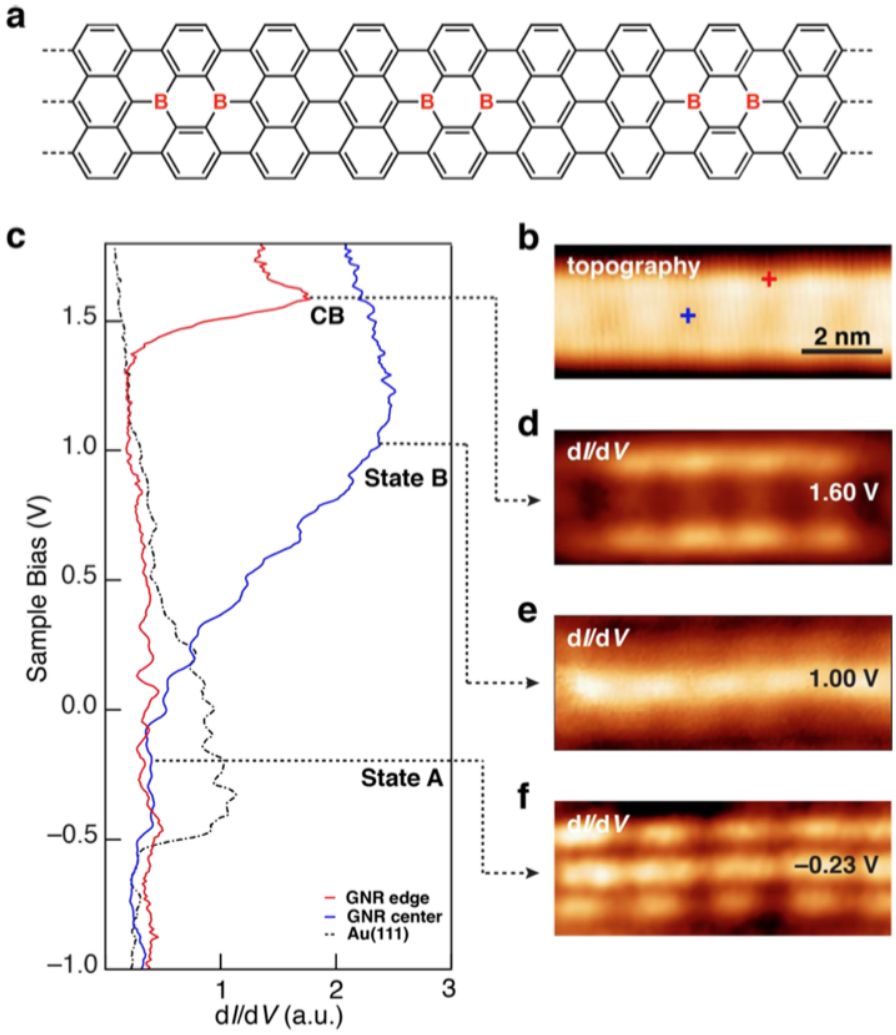


Figure 4.5: Electronic structure of densely boron-dimer-doped N = 7 AGNR on Au(111). (a) Wireframe sketch of a densely doped GNR. (b) STM topograph parameters: $V_s = 1.60$ V, $I_t = 20$ pA. (c) STM dI/dV spectroscopy measured at the edge and center of a densely doped GNR as shown in panel b. (d) dI/dV map taken at $V_s = 1.60$ V visualizes state at the CB edge. (e) dI/dV map taken at $V_s = 1.0$ V visualizes unoccupied dopant-induced state (State B). (f) dI/dV map taken at $V_s = -0.23$ V visualizes occupied dopant-induced state (State A). T = 4.5 K for all measurements. Panels d-f have the same scale as panel b.

GNRs doped with boron dimers in the dense limit was also explored. A wireframe sketch of the resulting boron-dimer-doped GNR structure is depicted in Fig. 4.5a, and an STM topograph is shown in Fig. 4.5b. As seen previously [29, 58], the boron-dimer-

doped segments of this GNR sit slightly closer to the substrate than the unsubstituted regions and lead to a $1.30 \pm 0.05$ Å amplitude periodic height modulation along the GNR long axis in topography. The electronic structure of densely doped GNRs is first characterized via dI/dV point spectroscopy. Figure 4.5c shows typical dI/dV spectra measured at a position along the backbone (blue curve) and at the edge (red curve) of a densely doped GNR with the same tip (spectroscopy positions are marked in Fig. 4.5b; the spectroscopic features had no significant dependence on how the tip was axially aligned with respect to dopants. The dI/dV spectrum recorded at the GNR edge shows a well-defined peak at $1.63 \pm 0.04$ eV above the Fermi level, $E_F$ [58]. The spectrum recorded along the densely doped GNR backbone is quite different and reveals a new, broad spectroscopic feature at $1.0 \pm 0.2$ eV above $E_F$ (this peak is absent in STS of undoped GNRs [94, 61, 52] ). Reproducible spectroscopic features below $E_F$ in the dI/dV point spectra was not observed for densely doped GNRs on Au(111).

Figure 4.5d shows a dI/dV map recorded at 1.60 eV, the energy of the upper spectroscopic peak. Here, the intensity of the LDOS is highest along the GNR edges, similar to what has previously been observed for energies near the CB edge in undoped N = 7 AGNRs [58, 26, 94, 61]. The dI/dV map obtained at an energy near the broad spectroscopic peak at 1.0 eV shows a pronounced shift in LDOS away from the GNR edges to the GNR backbone (Fig. 4.5e). Figure 4.5f shows a dI/dV map obtained in the filled states at a voltage of $V_s = -0.23$ V. Although no peak at this energy is observed in the dI/dV point spectroscopy, a clear transition is observed in the spatial LDOS distribution compared to dI/dV maps obtained at higher voltages. At this filled state energy, the LDOS is pushed outward toward the GNR edges, and a longitudinal nodal structure is seen that does not appear in the map at $V_s = 1.0$ V. The new densely doped spectroscopic features observed at $V_s = -0.23$ and 1.0 V do not occur for undoped N = 7 GNRs and so must arise from the influence of boron dopant dimers. We label them here as State A ($V_s = -0.23$ V) and State B ($V_s = 1.0$ V).

The experimental results for dilute and densely doped GNRs exhibit some qualitative agreement with our theoretical calculations for freestanding boron-dimer-doped GNRs, but there are significant discrepancies. For example, in the dilute-doping limit, the experiments faithfully reproduce the two expected defect states in the gap with one exhibiting *s*-like symmetry (State 2, which has no node) and the other exhibiting *p*-like symmetry (State 1, which has a node). However, the experimental measurements show a significant splitting between the two states ($\sim 1$ eV), whereas the theoretical defect states are essentially degenerate. Furthermore, it is not clear why the experimental peak seen for State 1 is so much narrower than the broad, sloping spectroscopic feature that defines State 2.

In the densely doped regime, the experimental peak observed at $V_s = 1.6$ eV (Fig. 4.5c, red curve) is consistent with the theoretically predicted CB (Fig. 4.1f). The new spectroscopic peak at $V_s \approx 1.0$ V (Fig. 4.5c, blue curve) also roughly corresponds to spectroscopic features expected to arise from a new dopant-induced band [22] (e.g., the upper dopant band in Fig. 4.1f). However, there are major discrepancies between experiment and theory here as well. Most significant is the energy alignment of the

observed spectroscopic features. The energy difference between the two experimental spectroscopic peaks shown in Fig. 4.5c is only $\sim$ 0.5 eV, whereas the theoretically predicted energy difference between the CB and the upper dopant band in Fig. 4.1f is $\sim$ 1.5 eV. Also, if the state imaged at V = -0.23 eV (Fig. 3f) is assigned to the lower dopant band, then the energy difference between the two dopant-induced bands in the experiment ($\sim$ 1.2 eV) is significantly larger than the calculated energy difference (0.5 eV). Moreover, the anomalously broad spectroscopic peak at $V_s = 1.0$ V is inconsistent with the calculation since the upper dopant bandwidth is predicted to be quite narrow (Fig. 4.1f).

We conclude that the freestanding GNR model used in the calculations is insufficient to describe our experimental data, most likely because it neglects the substrate. Therefore, in order to better understand the experimental results, we performed additional calculations that fully take into account coupling from the underlying Au(111) substrate upon which the boron doped GNRs rest. The electronic structures of both dilute-doped and densely-doped GNRs on Au(111) were calculated via DFT using the supercells shown in Fig. 4.6d and 4.7e, respectively. Similar to the experimental data, the boron dimers in a fully relaxed simulated GNR sit closer to the Au(111) surface than the carbon atoms in undoped segments of the ribbon. This reduction of the boron-gold distance indicates significant interaction between the boron dimer dopants and the gold substrate atoms.

In order to simulate the dilute-doped dI/dV spectroscopy of Fig. 4.4c, we calculated the energy-resolved LDOS (including gold substrate effects) averaged over a 7.5 Å$\times$ 7.5 Å area at 4 Å above the boron-dimer-doped segment following the topography of the GNR. The results are plotted in Fig. 4.6a . Substantial features are seen to appear in previously gapped regions due to hybridization between the GNR and the underlying Au(111) substrate (the CB (1.6 eV) and VB (-0.9 eV) edges are obtained from the undoped segment). In particular, two features are observed that arise from the boron defect: a broad resonance in the unoccupied states and a narrower resonance in the occupied states. The occupied resonance appears in the range -0.4 eV $< E <$ -0.1 eV and exhibits the LDOS pattern shown in Fig. 4.6c (obtained at E = -0.21 eV). This LDOS map has bright features at the outer edges and two interior peaks of high intensity located on the C-B bonds that lie along the GNR axis. As seen in Fig. 4.6f, the wave function at this energy has odd parity ($p$-like) under mirror symmetry.

The unoccupied LDOS is quite different from what is seen in the occupied states. Here a much broader feature arises over the range 0.3 eV $< E <$ 0.9 eV (a slight dip can be seen at $E \approx 0.5$ eV). Figure 4.6b shows a representative LDOS map of this defect state (obtained at E = 0.38 eV). As seen in Fig. 4.6e, this dopant state has a more delocalized wave function than the occupied state feature and exhibits approximate even parity ($s$-like).

The calculated behavior of the dilute-doped GNR on Au(111) supports our hypothesis that differences observed between the experiment and the "freestanding" theory arise from the interaction between boron-dimer-doped GNRs and the gold substrate. The reasonably good agreement between theory and experiment for the defect state

energies and broadening allows us to identify the occupied and unoccupied features in the theoretical LDOS of Fig. 4.6a with experimentally observed State 1 and State 2 of Fig. 4.2c. Further evidence for this assignment is found in the striking resemblance of the theoretical occupied state LDOS pattern (Fig. 4.6c) to State 1 (Fig. 4.4f), as well as the resemblance of the theoretical unoccupied LDOS pattern (Fig. 4.6b) to State 2 (Fig. 4.4e). The energy splitting between the central energy of the two simulated defect state peaks ($\sim$ 1 V) is also similar to what is observed experimentally, indicating that the boron-dimer-induced defect states (which are nearly degenerate for a freestanding GNR) are strongly split by interaction with the Au(111) substrate. This interaction also explains the different broadening of the two defect states, which is faithfully reproduced by the calculation and which arises due to the different symmetries of the dopant states. Because State 1 has $p$-like character, it hybridizes more weakly with the $s$-like surface states of gold (leading to a narrower peak), whereas State 2 has $s$-like character and so hybridizes more strongly with gold (leading to a broader peak). The $s$- and $p$-like symmetries of the boron defect states are thus primary factors in determining the dopant electronic structure for the strongly hybridized boron-dimer-doped GNR/Au(111) complex.

Motivated by the agreement between experiment and theory for the dilute-doped GNRs in the presence of Au(111), we examined the electronic structure of densely doped GNRs supported by Au(111). The energy-resolved LDOS 4 Å above the boron-dimer-doped segment was calculated using the same method as in the dilute case and is shown in Fig. 4.7a. The energy-dependent LDOS of Fig. 4.7a is very similar to what is seen in the dilute-doped case (Fig. 4.6a). For example, a broad unoccupied resonance and a narrower occupied resonance arise due to substrate interactions, and the resonances have almost identical energy and width as the State 1 and 2 features of the dilute regime. A representative LDOS map of the theoretical unoccupied states obtained at E = 0.35 eV (Fig. 4.7c) is dominated by nearly uniform bright intensity along the longitudinal axis of the densely doped GNR (i.e., bright intensity occurs at the boron dimer sites as well as at the carbon dimer sites between them). This theoretical LDOS map is qualitatively very similar to the experimental unoccupied state dI/dV map of Fig. 4.5e, and so we identify the broad, unoccupied state feature of Fig. 4.7a as State B. A representative map of the theoretical occupied states obtained at E = -0.22 eV (Fig. 4.7d) shows a shifting of LDOS intensity to the GNR edges and a new lateral periodicity whose wavelength matches the distance between boron dimers (due to reduction in LDOS at the carbon dimer sites between boron dimers). This theoretical LDOS map is qualitatively similar to the experimental occupied state dI/dV map of Fig. 4.5f, and so we identify the narrow, occupied state feature of Fig. 4.7a as State A. The lack of a clear peak due to State A in the experimental dI/dV point spectroscopy (Fig. 4.5c) is likely due to increased hybridization between densely doped lower dopant band states and the Au(111) surface compared to dopant states in the dilute-doped regime.

Our calculations allow us to confirm that the underlying physics determining the behavior of densely doped GNRs is similar to the symmetry-dependent mechanism at

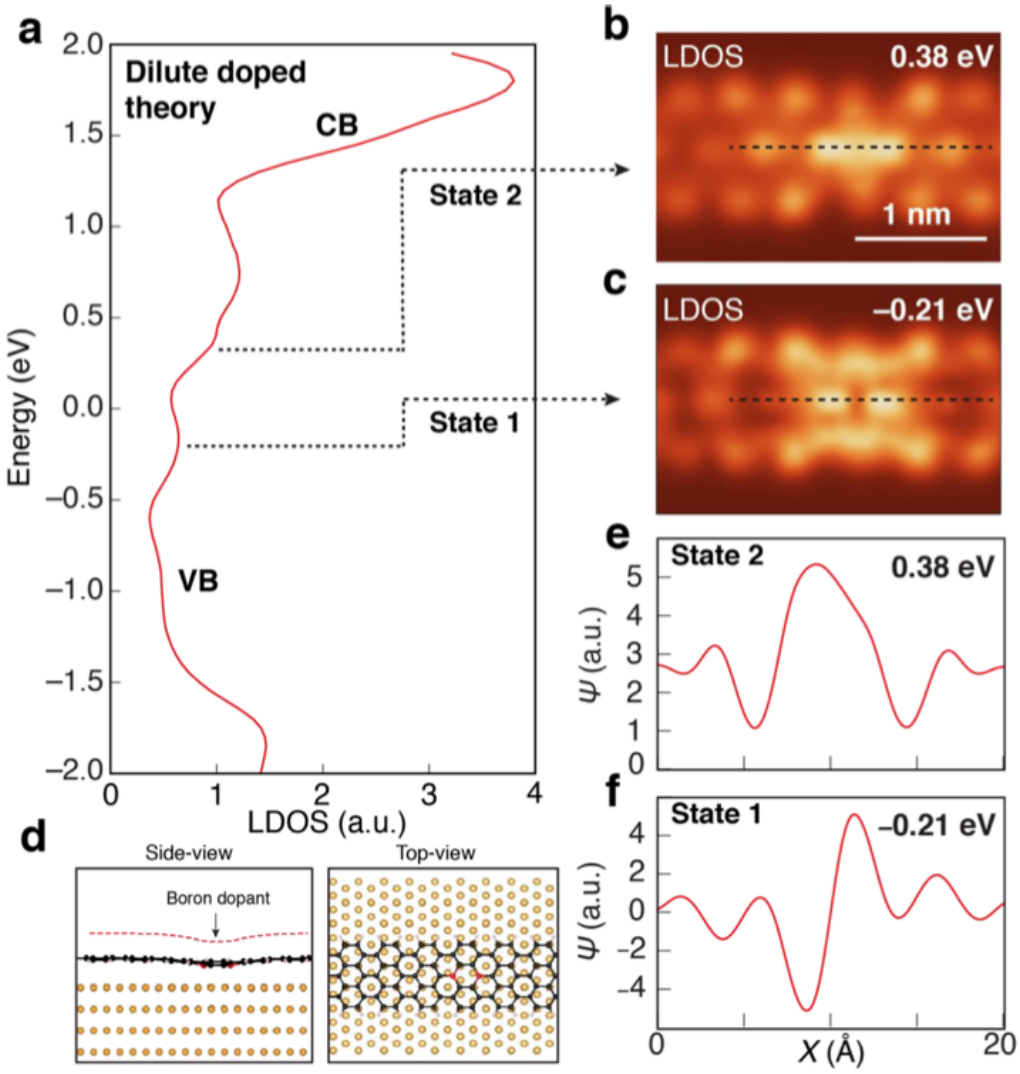


Figure 4.6: DFT-LDA calculation of dilute-doped N = 7 GNR on Au(111) substrate. (a) Calculated LDOS 4 Åabove the boron-dimer-doped segment shows dopant States 1 and 2 (theoretical LDOS is broadened by a Gaussian function with standard deviation $\sigma$ = 125 meV). Calculated LDOS map is shown for (b) E = 0.38 eV (integrated over a 0.05 eV energy window) and (c) E = -0.21 eV (integrated over a 0.05 eV energy window). (d) Side-view and top-view of the supercell and the relaxed structure used to calculate the dilute-doped GNR. The supercell includes four layers of Au atoms. Red dashed line shows the surface upon which the LDOS maps are calculated. (e) Calculated wave function along the dashed line in panel b for E = 0.38 eV. (f) Calculated wave function along the dashed line in panel c for E = -0.21 eV. Panels b and c have the same scale.

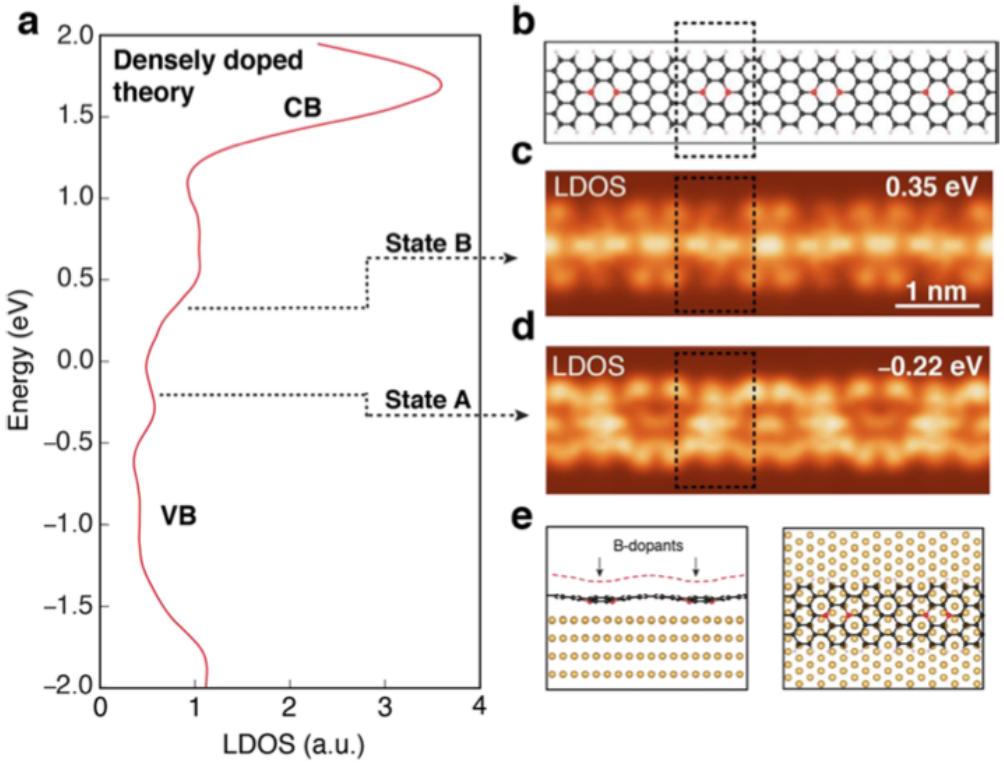


Figure 4.7: DFT-LDA calculation of densely doped N = 7 GNR on Au(111) substrate. (a) Calculated LDOS 4 Åabove boron-dimer-doped segment shows dopant States A and B (theoretical LDOS is broadened by a Gaussian function with standard deviation $\sigma = 125$ meV). (b) Wireframe sketch shows location of boron dimers. Calculated LDOS maps (each including four boron dimers) are shown for (c) E = 0.35 eV (integrated over a 0.05 eV energy window) and (d) E = -0.22 eV (integrated over a 0.05 eV energy window). (e) Side view and top view of the supercell and the relaxed structure (includes four layers of Au atoms) used to calculate the relaxed densely doped GNR. The red dashed line shows the surface upon which the LDOS maps are calculated. Panels c and d have the same scale.

work in the dilute-doped regime, despite the significant difference in dopant concentrations. This can be seen by examining the wave functions of occupied and empty states for densely doped GNRs (Fig. 4.8). The wave function for State B is seen to be symmetric around a line bisecting a boron dimer and thus exhibits $s$-like symmetry similar to State 2 of the dilute regime (Fig. 4.6e). This explains why the densely doped GNR couples so strongly to the $s$-like conduction band of Au(111) at this energy, thus leading to the broad, unoccupied resonance observed both theoretically (Fig. 4.7a) and experimentally (Fig. 4.5c), which looks so similar to State 2 of the dilute regime. The wave function for State A, however, has $p$-like symmetry around the boron dimer which explains why it couples less strongly to the gold conduction band and exhibits a narrower resonance, similar to State 1 of the dilute regime. Due to the dominant effects of substrate hybridization, States A and B of the dense regime can be heuristically thought of as simple 1D arrays of States 1 and 2 of the dilute regime, respectively. Despite this strong substrate interaction, however, states A and B can still be associated with the lower and upper dopant bands of the freestanding GNR shown in Fig. 4.1f. The experimental energies of these states can thus be used to extract an apparent band gap of $E_g \approx 1.2$ eV for densely doped GNRs on Au(111).

In conclusion, our experimental and theoretical studies show that introduction of boron dimer dopants into AGNRs induces the formation of two new in-gap dopant states that have different symmetries. These dopant-induced states continuously evolve as the boron dopant concentration increases. Moreover, we see that hybridization between dopant dimers and the underlying Au(111) substrate has an unusually strong impact on the electronic structure of boron-dimer-doped GNRs, much greater than for other doped GNR systems studied to date [16, 19, 78]. Both the dilute and densely doped electronic behavior depends strongly on the impurity state symmetry, with $s$-like (p-like) states hybridizing more strongly (weakly) with the gold substrate, thus leading to strong, symmetry-dependent energy splitting. This strong substrate coupling masks the effects of impurity-impurity interactions that are predicted for freestanding boron-dimer-doped GNRs. We thus expect very different electronic behavior (including a clearer, more well-defined bandgap) for boron-dimer-doped GNRs placed on substrates that interact less strongly with boron impurity atoms than gold.

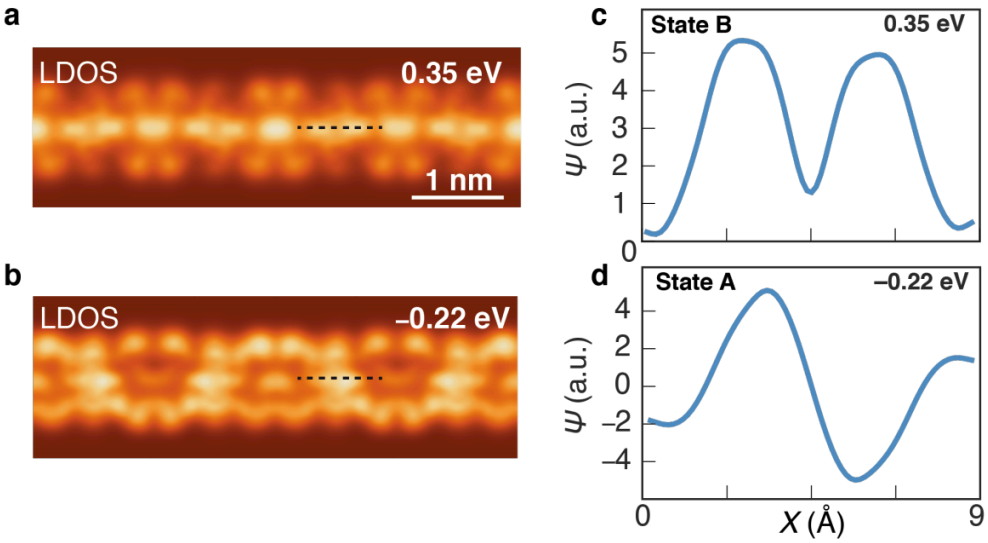


Figure 4.8: Calculated wavefunctions of densely-doped AGNRs. Wavefunctions of States A and B of the densely-doped GNR, (a, b) Calculated LDOS maps of States A and B for the densely-doped AGNR. (c) Calculated wavefunction along the dashed line in (a) at E = 0.35 eV shows the *s*-like symmetry nature of State B. (d) Calculated wavefunction along the dashed line in (b) at E = - 0.22 eV exhibits a node (i.e., the wavefunction crosses the x-axis) which indicates the *p*-like symmetry of State A. (a) and (b) have the same scale.

# Chapter 5

# Designing of graphene nanoribbon double-quantum-well transistor

## 5.1 Introduction

A typical tunneling field effect transistor (TFET) contains a source and drain made of semiconductors with a finite gap. Between the source and drain part, there is a gapped barrier region whose energy levels can be tuned by external electric field generated by the gate voltage. By tuning the relative energy level of the barrier part using an applied gate voltage, the energy allowed region (energy range with finite density of states) of the source, drain and barrier will align or misalign so that current could go through the transistor or be forbidden, which leads to the on or off state of the TFET.

Because of widely present defects, finite temperature effect, and other effects, the density of states near a band edge of the source, drain or barrier materials never decays sharply into nominally the energy gap. The change of gate voltage that is required to magnify the tunneling current by ten times is defined as the swing voltage $V_s$. Since a typical TFET works at room temperature, there is a thermal limit on the swing voltage,

$$V_s > \frac{1}{\frac{dlogI}{dV_g}} \approx \frac{k_B T}{q} ln(10) \approx 60mV/decade, \tag{5.1}$$

where $I$ is the tunneling current, $V_g$ denotes the gate voltage, $q$ is the elementary charge of an electron, $k_B$ is the Boltzmann's constant, and $T$ is the room temperature. Because of the slow decaying density of states at the band edges, one needs at least a 60 meV change in the gate voltage to magnify or reduce the tunneling current by 10 times [2]. To make a logic gate using the TFET, a typical on/off ratio ( the ratio between the current in the on and off state) greater than $10^6$ is needed, thus the gate voltage applied on the barrier would be in the order of 1 V to make the logic gate working.

If one could decrease the limit on the swing voltage so that a logic gate could be manipulated by a gate voltage $\sim$ 0.1 V or even lower, this will save a lot of energy in operating electronic devices and solve the heating problem in electronic devices. This would be very important in improving the power of scientific computing. In this chapter, we introduce a new scheme in designing a double-quantum-well TFET to try to break this thermal limit in the swing voltage.

## 5.2 Double-quantum-well transistor

The quantum wells (or often called dots) will contain discrete quantum energy levels because of quantum confinement. The density of states of an isolated quantum energy level is often sharp and not affected by the thermal broadening. Thus, we can put two quantum dots next to each other, and connect them to two different metallic leads. The two quantum dots and two metallic leads are arranged in the way shown in Fig. 5.1 (a) and the adjacent elements are separated by a barrier with a wide energy gap that is also formed by GNRs (See Fig. 5.1(a) ). By tuning the energy level of the two isolated quantum well states in the two quantum dots, one could align or misalign the energy levels. In this way, we can turn on or turn off the double-quantum-well transistor. [109]

The swing voltage of the system only depends on the lineshape of the two isolated quantum well energy levels without the thermal effects from the broadened band edges. If the lineshape of the quantum dot decays fast in energy(e.g. exponentially), it is possible to break the 60 mV / decade thermal limit on the swing voltage. Therefore, we study the lineshape of a quantum dot coupled to the metallic wire in the following section.

We design the double-quantum-well transistor using GNRs exploiting its versatile electronic properties determined by its edge shape and widths. Figure 5.1 (a) shows a schematic design of the double-quantum-well transistor using GNRs. The lead parts are formed with zigzag GNRs which has very small energy gap. The barrier parts are formed using the N=7 armchair GNR which has a $\sim$ 3.8 eV quasiparticle gap [113], and its gap will be further increased due to its finite length because of quantum confinement effects. The quantum dots are made of N = 11 armchair GNRs which has a $\sim$ 1.0 eV quasiparticle gap [113]. The quantum well states could be confined in the quantum dot region according to tight-binding calculations. The wavefunction of the quantum well states closest to the Fermi level are localized at the zigzag edges at the corner of the quantum dots.

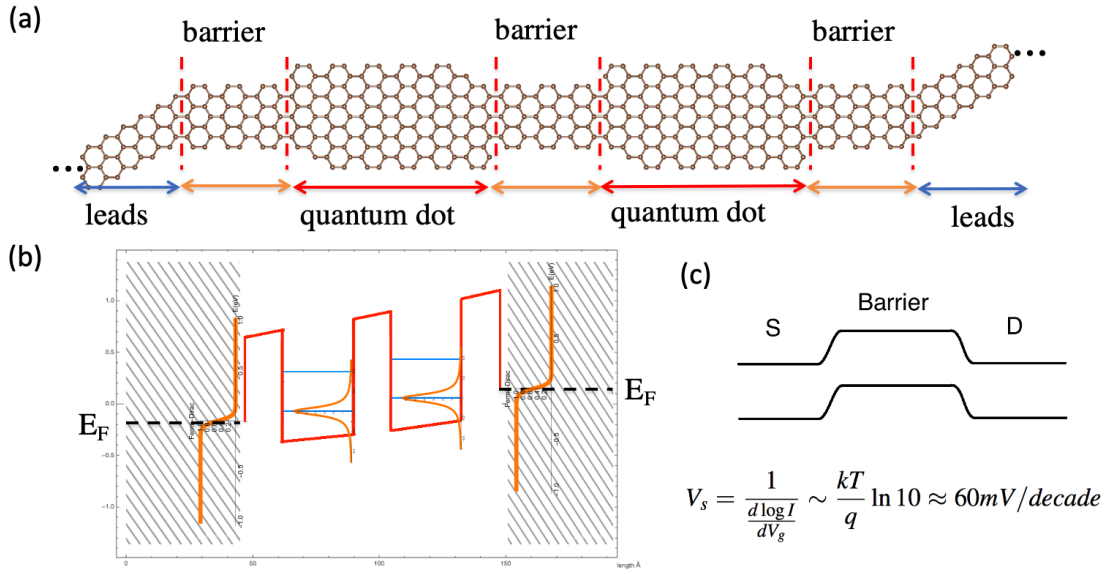


Figure 5.1: The schematic configuration of a double-quantum-well transistor. The leads part are made of metallic zigzag GNRs, the barrier parts are made of N=7 AGNRs with $\sim$ 3.8 eV quasiparticle gap, and the quantum dot part are made of deformed N=11 AGNRs with smaller band gap than the barrier part. The dangling bands at the edge the GNR structure should be capped by hydrogen atoms. (b) The band diagram of the double-quantum-well transistor. The orange curve shows the Fermi-Dirac filling in the metallic GNR leads and the density of states of the isolated quantum energy levels in the quantum dots. (c) The band diagram of a typical field effect transistor.

## 5.3 Lineshape of a quantum well state coupled to metallic leads

The energy level broadening of an isolated quantum energy level coupled to metallic wire is a hybridization broadening, and its lineshape could be calculated by the Kubo's formalism [64]. The Kubo's formalism calculates the spectral function of a system in response to a time-dependent perturbation applied on the system.

The leads that the quantum well state coupled to can be treat as a perturbation to the isolated energy level, and the lineshape of the quantum level is related to its response functions under perturbations. Assuming the perturbation is a plane wave electric field

$$E_\beta(\boldsymbol{x'}, t) = E^0_\beta(\omega) e^{i\boldsymbol{q}\cdot\boldsymbol{x'} - i\omega t}, \tag{5.2}$$

where $\beta$ denotes the spatial component of the field, $\omega$ is the frequency, and $q$ is the wavevector.

The resulting current can by calculated by the Kubo's formalism.

$$\langle \hat{j_\alpha}(\boldsymbol{x},t)\rangle = \langle \hat{j_\alpha}(\boldsymbol{x},t)_0\rangle + \frac{1}{\hbar\omega}\int_{-\infty}^{t} dt' \int d^3x' E_\beta(\boldsymbol{x'},t') Tr\left\{\rho_0\left[\hat{j_\alpha}(\boldsymbol{x},t),\hat{j_\beta}(\boldsymbol{x'},t')\right]\right\}, \tag{5.3}$$

where $Tr\left\{\rho_0\left[\hat{j_\alpha}(\boldsymbol{x},t),\hat{j_\beta}(\boldsymbol{x'},t')\right]\right\} = \sigma_{\alpha\beta}(\boldsymbol{x}-\boldsymbol{x'},t-t')$ is the current-current correlation function. We note that the response could only react to the perturbation in previous times. The time integration limit from $-\infty$ to a time $t$ is restricted by causality. With a change of variable,

$$\langle \hat{j_\alpha}(\boldsymbol{x},t)\rangle = \frac{1}{\hbar\omega}\int d^3\boldsymbol{x'} E^0_\beta(\omega) e^{i\boldsymbol{q}\cdot\boldsymbol{x'}-i\omega t}\left[\int_0^{+\infty} d\tau e^{i\omega\tau} Tr\left\{\rho_0\left[\hat{j_\alpha}(\boldsymbol{x},\tau),\hat{j_\beta}(\boldsymbol{x'},0)\right]\right\}\right] \tag{5.4}$$

$$= \frac{1}{\hbar\omega}\int d^3\boldsymbol{x'} E_\beta(\boldsymbol{x'},t)\sigma_{\alpha\beta}(\boldsymbol{x}-\boldsymbol{x'},\omega). \tag{5.5}$$

The response function $\sigma_{\alpha\beta}(\boldsymbol{x}-\boldsymbol{x'},\omega)$ is calculated from a time integration starting from the zero time

$$\lim_{\boldsymbol{x}-\boldsymbol{x'}\to 0}\sigma_{\alpha\beta}(\boldsymbol{x}-\boldsymbol{x'},\omega) = \int_0^{+\infty} d\tau e^{i\omega\tau}\lim_{\boldsymbol{x}-\boldsymbol{x'}\to 0} Tr\left\{\rho_0\left[\hat{j_\alpha}(\boldsymbol{x},\tau),\hat{j_\beta}(\boldsymbol{x'},0)\right]\right\}. \tag{5.6}$$

$\lim_{\boldsymbol{x}-\boldsymbol{x'}\to 0}\sigma_{\alpha\beta}(\boldsymbol{x}-\boldsymbol{x'},\omega)$ is the Fourier transform of a discontinuous function since

$$\lim_{\tau\to 0^+}\lim_{\boldsymbol{x}-\boldsymbol{x'}\to 0} e^{i\omega\tau} Tr\left\{\rho_0\left[\hat{j_\alpha}(\boldsymbol{x},\tau),\hat{j_\beta}(\boldsymbol{x'},0)\right]\right\} = 1. \tag{5.7}$$

because the correlation between two current operators at the same position and nearly the same time should be 1. As a result, $\lim_{\boldsymbol{x}-\boldsymbol{x'}\to 0}\sigma_{\alpha\beta}(\boldsymbol{x}-\boldsymbol{x'},\omega)$ is the Fourier transform of a discontinuous function (See Eqn.(5.6)). The Fourier transform of a discontinuous function always has algebraic decay as $\sim \frac{1}{\omega^2} + i\frac{1}{\omega}$ for high frequencies, thus $\lim_{\boldsymbol{x}-\boldsymbol{x'}\to 0}\sigma_{\alpha\beta}(\boldsymbol{x}-\boldsymbol{x'},\omega)$ will decay as $\sim \frac{1}{\omega^2} + i\frac{1}{\omega}$ for large $\omega$ . The real part of $\sigma_{\alpha\beta}(t)$ is proportional to the spectral function of the energy level, which is the lineshape. Thus, we have shown that the decay of the density of states of a quantum energy level coupled to a metallic lead has the slow algebraic under the assumption that Eq. (5.6) is valid. If the lineshape is a Lorentzian then we may not use the double-quantum-well scheme shown in Fig. 5.1 to beat the thermal limit in the swing voltage.

We also perform a first-principles transport calculation to investigate the lineshape of a quantum dot state coupled to metalic leads. As shown by Fig. 5.2 (a), a quantum dot made of N=11 armchair GNR is connected to metallic leads made of nitrogen

doped N=7 armchair GNR through barriers made by N=7 armchair GNR. The nitrogen doped N=7 armchair GNR shown in the "leads" part in Fig. 5.2 (a) is metallic according to first-principles DFT calculations with LDA. The leads extend infinitely to the left and to the right, and only four unit cells of this nitrogen doped N=7 armchair GNR is shown on each side. The quantum conductance of the system shown in Fig. 5.2 (a) from the left to the right is calculated by the Quantum ESPRESSO package [37] and the Wannier90 [76] package, using a "Left-conductor-right" formalism [20] implemented in Wannier90. The numbers "1", "2", "3", "4" denote the peaks corresponding to the isolated quantum well energy levels confined in the quantum dot region. By the Landauer formula, the quantum conductance $G$ is proportional to the number of transverse mode $T$.

$$G(\mu) = G_0 T(\mu) \tag{5.8}$$

where $G_0$ is the conductance quantum, and $\mu$ is the chemical potential. The number of transverse mode is proportional to the density of states of the quantum well state, thus the quantum conductance spectrum is the lineshape of the quantum well state. By fitting the peak "1" with a Lorentzian profile (the orange curve in Fig. 5.2(b)), we can see that the lineshape of the quantum well states has a Lorentzian decay, consistent with our theoretical calculation via the Kubo's formalism.

## 5.4 Lineshape of a quantum well state coupled to metallic leads with finite band width

The previous section calculates the lineshape of a quantum well state coupled to metallic leads with infinite band widths. If the metallic leads has finite band width, the density of states of the quantum well state must decay to zero in the energy forbidden region of the metallic leads. Thus, we investigate the lineshape of a quantum well state coupled to metallic leads with finite band width and see if the finite band width in the metallic leads helps to build quantum well state with faster decaying density of states.

We use a simple tight-binding model system to calculate the analytic form of the density of states (DOS) of a quantum dot coupled to the metallic leads with finite band width. We assume the metallic leads with finite band width is formed by a semi-infinite chain of unit cells (Fig. 5.3) with one atomic orbitals per unit cell, and the hopping parameter between two adjacent atomic orbitals is assumed to be $t$. Thus the semi-infinite chain of atomic orbitals with one electron per orbital form a metallic wire with bandwidth equal to $2|t|$. We assume the hopping parameter between the end atomic orbital on the metallic wire and the quantum dot is $s$. We also assume there is only one atomic orbital in the quantum dot, and the onsite energy for all the atomic orbitals in the leads and the quantum dot are 0, and we ignore all hoppings beyond nearest neighbor.

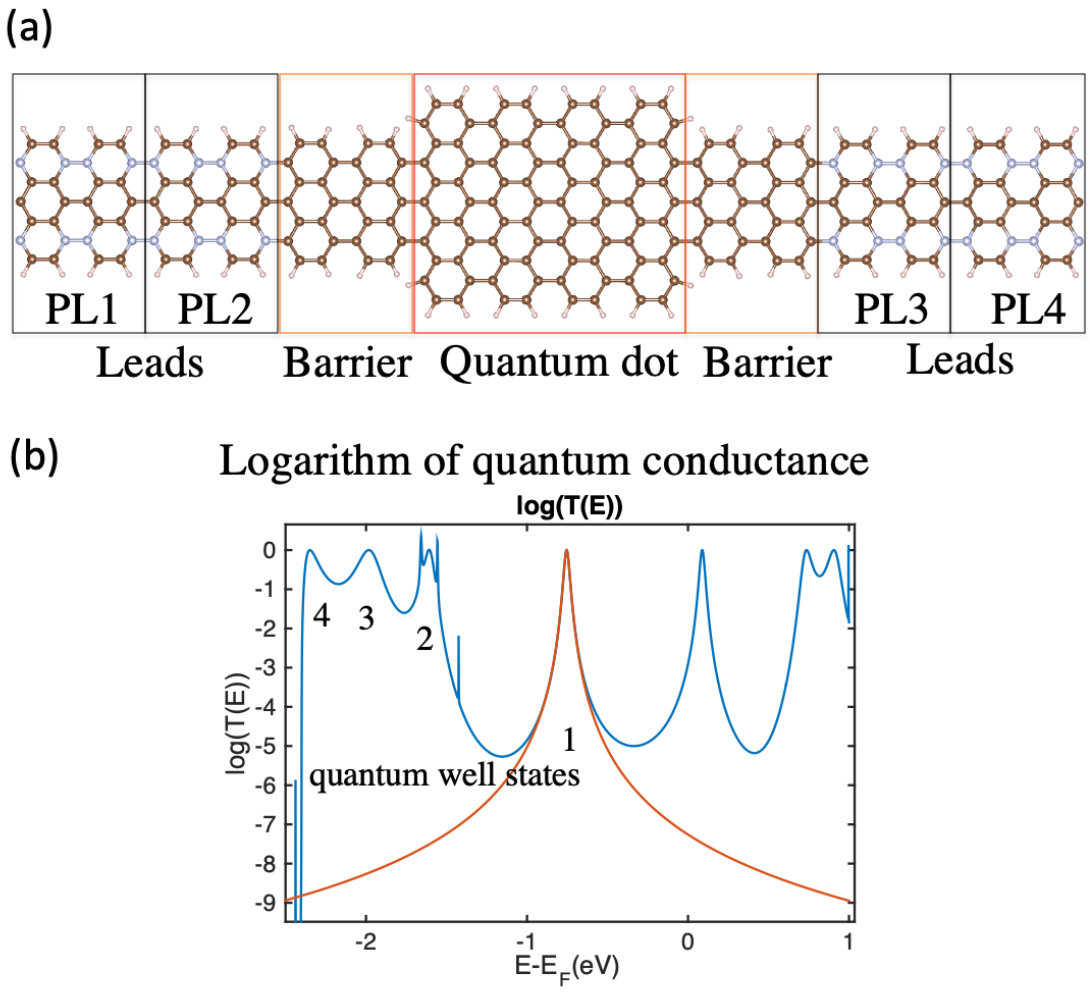


Figure 5.2: (a) The structure of a quantum well made by N=11 armchair GNR coupled to metallic leads made by nitrogen doped armchair GNR. The barrier is made of N=7 armchair GNR. (b) The calculated quantum conductance $T(E)$ of the system as a function of bias voltage, plotted in logarithm scale. The orange curve is a Lorentzian profile fitted to the peak marked by "1".

We divide all the quantities by the magnitude of the hopping parameter $|t|$ to make them dimensionless. Assume the energy is denoted by $\omega$, so the dimensionless energy $x$ is defined by

$$x = \frac{\omega}{|t|}. \tag{5.9}$$

The dimensionless hopping between the metallic leads and the quantum dot state is:

$$\sigma = \frac{s}{|t|}. \tag{5.10}$$

Using the transfer matrix formalism, we could calculate the analytic form of the local density of states of the quantum dot, expressed by the dimensionless energy $x$, and the dimensionless hopping $\sigma$

$$DOS(x) = \frac{1}{\pi}|\Im(\frac{1}{x - \sigma^2 \frac{1}{\frac{x}{2}+i\sqrt{1-(\frac{x}{2})^2}}})| \tag{5.11}$$

$$= \frac{\sigma^2}{\pi(1-\sigma^2)} \frac{1}{x^2 + \frac{\sigma^4}{1-\sigma^2}} \sqrt{1-(\frac{x}{2})^2}. \tag{5.12}$$

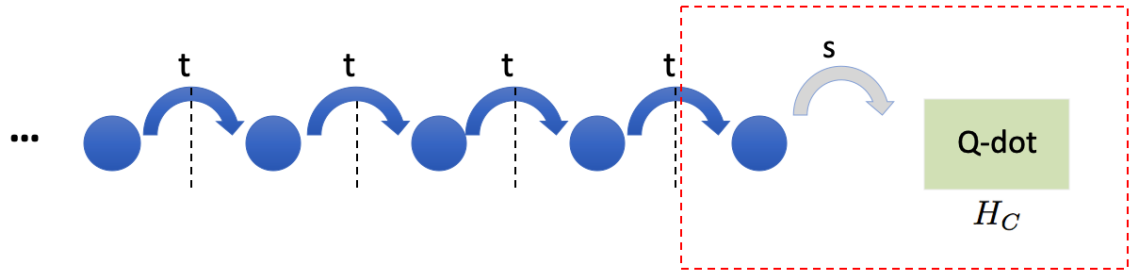


Figure 5.3: The model system of a quantum dot (Q-dot) coupled to a metallic leads with a finite band width. The interaction between the metallic chain and the Q-dot is described by the hopping between the end atom in the metallic chain and the Q-dot, $s$. The hoppings between adjacent atoms in the metallic chain is $t$.

The DOS and the logarithm of the DOS) is plotted in Fig. 5.4 (a) and (b), respectively. Near the peak of the density of states, the lineshape is still Lorentzian. However, the density of states decays rapidly at the band edge of the metallic leads. This decays faster than an exponential decay.

We could align and misalign the peak of the DOS of the quantum dot coupled to metallic leads to try to made a transistor with sharp turning on and off (Fig. 5.4

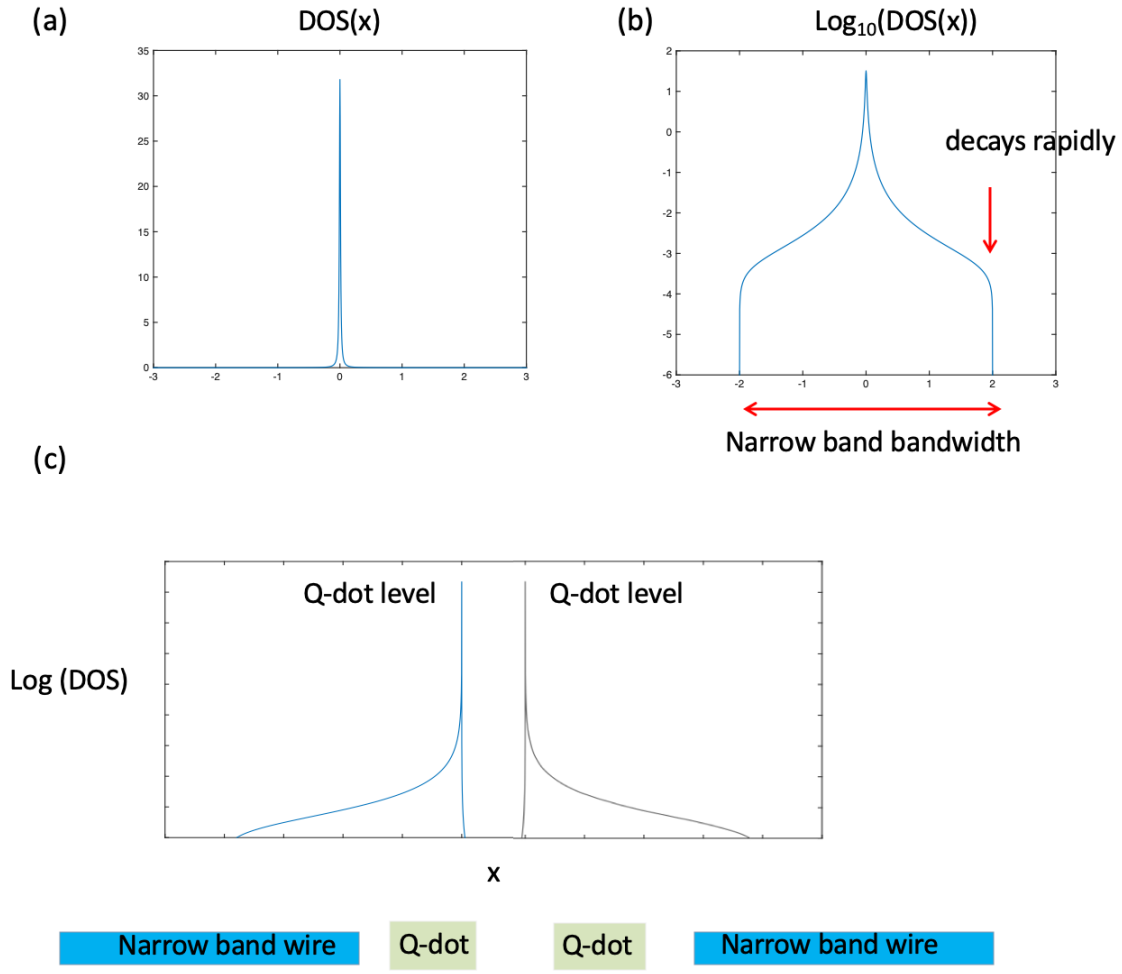


Figure 5.4: (a) The local density of states of the quantum well coupled to a narrow band metal. (b) The logarithm of the local density in (a). (c) The configuration of double-quantum-well with quantum dots (Q-dots) coupled to metallic wires with finite band widths. The blue curve and the gray curve are the logarithm of the local density of states on the left Q-dot and right Q-dot, respectively. The horizontal axis is logarithm of density of states while the vertical axis is the dimensionless energy x. It shows the case where the energy level of the two Q-dots are not aligned (off-state). The peak positions of the LDOS of the Q-dots could be tuned by the gate voltage to be aligned (on-state).

(c)). However, the band edge of the metallic leads will be further broadened as it would be eventually connected to other metallic leads further away, and the presence of unavoidable defects in the leads would also broaden the lineshape at the band edges. It remains a challenge if a double-quantum-well designing scheme of the TFET for breaking the 60 meV / decade limit on the swing voltage. To further explore this possibility, detailed calculations including other effects, such as phonons, defects and so on, need to be further performed.

# Chapter 6

# Optical properties of crystalline conjugated polymers

## 6.1 Introduction

Conjugated polymers such as poly(p-phenylene vinylene) (PPV) polymers are promising candidates for optoelectronic applications, for example, light emitting diodes (LED) due to its fascinating electronic and optoelectronic properties [105, 74, 80, 4]. In this chapter, we present our first-principles study of the optical properties of crystalline PPV polymer using the GW-BSE formalism. Our calculated optical spectra show a level of agreement with experiments significantly superior to previous studies [92, 110, 111]. This chapter is based on a manuscript in preparation [117].

## 6.2 Optical excitations in poly(p-phenylene vinylene) polymer crystals

### 6.2.1 Background and motivation

The optical spectrum of the crystalline PPV has been measured since two decades ago [42, 72, 15, 59, 93, 84, 13] due to its potential application in building organic LEDs. The measured absorption at the room temperature [42, 15, 59, 93, 84, 13] or at 77 K [72] show that the first absorption peak is at energy about 2.3 - 2.7 eV. However, first-principles calculations using the GW-BSE formalism by Van der Horst et al. [110, 111] on a crystalline PPV shows an optical gap at around 1.75 eV, and the calculation performed by Rohlfing and Louie [92] on an isolated single chain PPV only shows a prominent peak at around 2.1 eV, while the peaks at higher energies $\sim$ 4.8 eV and $\sim$ 6.0 eV has very small peak heights (see Fig. 6.2) comparing to the measured optical absorption spectra. The former theoretical result is far from experiment, and the latter also appears not quantitative since environment screening in a crystal would reduce the optical excitation energies.

To explain the discrepancy between the previously calculated optical absorption spectra and the measured results, we perform a more detailed calculation using the GW-BSE formalism to obtain the absorption spectra of crystalline PPV, and to see if the measured absorption spectra can be explained by the GW-BSE formalism incorporating electron-electron and electron-hole interaction in the optical excitation processes.

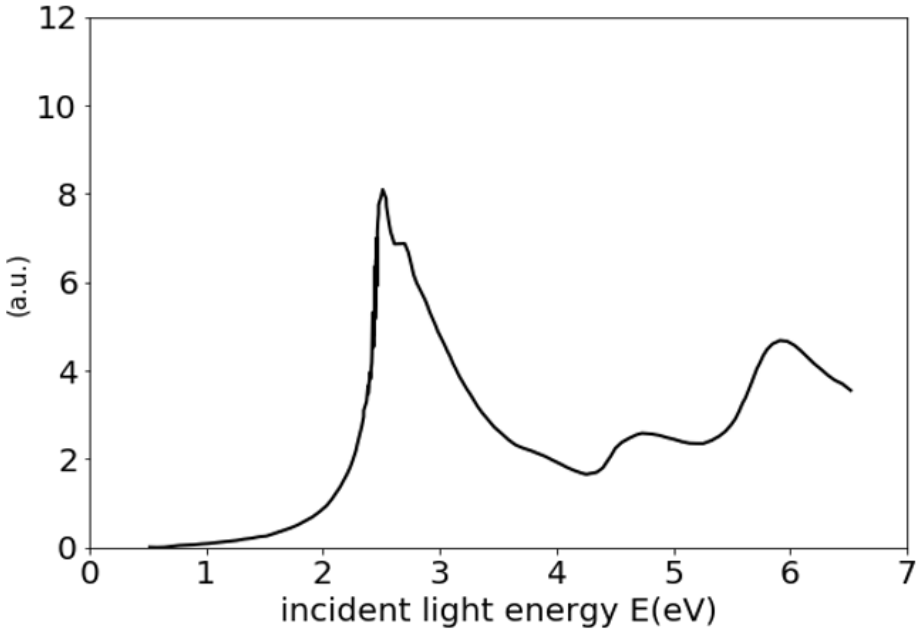


Figure 6.1: The measured absorption spectrum of crystalline PPV. The data is taken from Ref. [42].

### 6.2.2 Structural optimization

To calculate the optical excitation properties of the crystalline PPV, we first determine the structure of the crystalline PPV by first-principles DFT calculations. Crystalline PPV has an orthorhombic unit cell (Fig. 6.3 (a)), in which each contains two PPV chains. Each chain inside the unit cell has its molecular plane tilted with respect to the plane defined by the lattice vector $a$ and $c$, and the tilted angle is defined as the setting angle (Fig. 6.3(b)). The layer shift between the two PPV chains inside one unit cell is defined as the length of the shift vector divided by the lattice constant in the direction defined by c (See Fig. 6.3 (c)) . Many experimental studies on measuring the structure of the crystalline PPV had been conducted decades ago [14, 108, 38, 25], including an accurate measurement of the lattice constants [38], and measurements on structural parameters such as setting angles and so on [14, 108, 25, 38]. Thus we use the experimental values for the lattice constants (See Fig. 6.3 (a)) from Ref. [38].

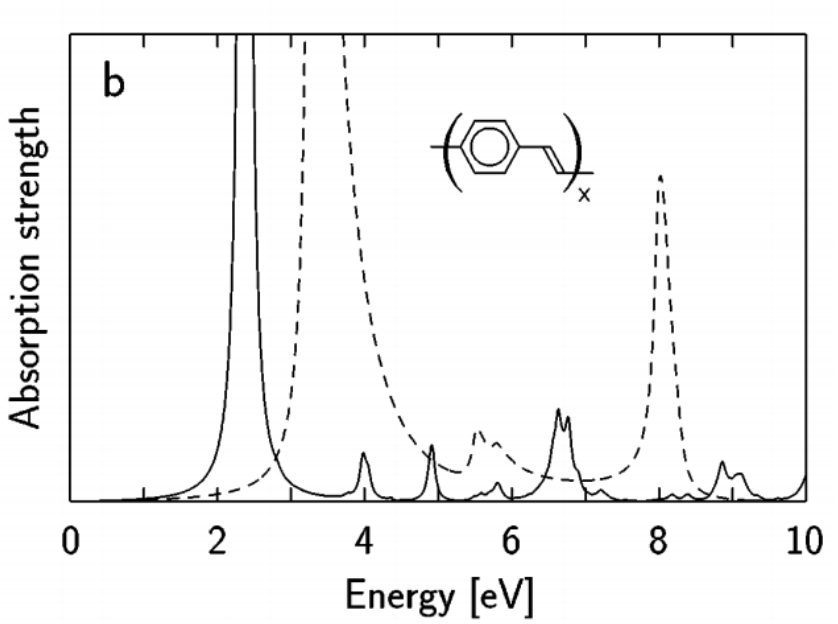


Figure 6.2: Calculated optical absorption spectrum of PPV in arbitrary units. The solid (dashed) lines denote spectra including (neglecting) electron-hole interaction. The polarization vector of the electric field is along the polymer chain. The figure includes an artificial broadening of 0.05 eV. The figure is taken from Ref. [92].

We determine the structure parameters such as the setting angle (Fig. 6.3 (b)) and the layer shift (Fig. 6.3 (c, d)) by finding the lowest energy structure configurations using first-principles DFT calculations. The relative total energy per unit cell was calculated using DFT-LDA with "grimme-d2" Van der Waals correction [39] to better incorporate the Van der Waals interaction between different polymer chains. For a setting angle of 52 degrees (Fig. 6.3(b)), the system has the lowest energy, and this matches well with experimental measurement showing a setting angle being $50 \pm 2$ degrees [25]. For the layer shift, Fig. 6.3 (d) shows the energy diagram per unit cell as a function of the layer shift parameter, and the global minimum is located at 0.18 while a local minimum exists at 0.5. The energy difference between systems at the local minimum and the global minimum is only $\sim$ 2.72 meV per unit cell, which corresponds to the average kinetic energy per atom at $\sim$ 20 K, so the system may have large probability sitting in both configurations at 300K at which the optical absorption experiments is performed. As a result, we perform the GW-BSE calculations on structures corresponding to both the local and global minimum to analyze the optical absorption properties.

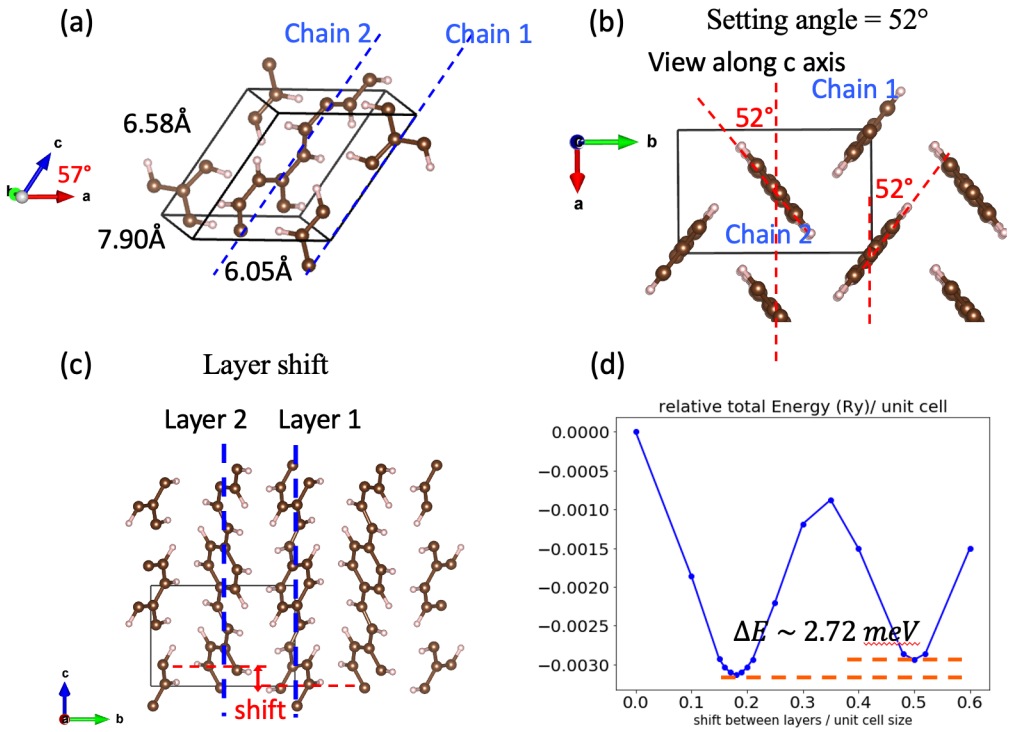


Figure 6.3: Structural optimization of the crystalline PPV. (a) The orthorhombic unit cell of the crystalline PPV determined by experiments. The lattice constants in the three directions a, b, and c are 6.05, 7.90, 6.58 Å, respectively. The angle between the two non-perpendicular axis, $a$ and $c$, is 57 degrees. (b) The definition of the setting angle: the angle between the molecular plane of one PPV chain and the plane defined by axis $a$ and $c$. (c) The definition of the layer shift between the two PPV chains inside one unit cell: the length of the shift vector divided by the lattice constant in the direction defined by $c$. (d) The relative total energy per unit cell as a function of the layer shift. The global (local) minimum is located at layer shift = 0.18 (0.5).

### 6.2.3 Quasiparticle band structures

We perform GW calculations on the crystalline PPV with the layer shift parameter being 0.18 and 0.5. The GW calculation is performed with a starting mean field wavefunctions calculated from DFT with LDA. A $2 \times 2 \times 24$ k grid was used, and the dielectric function $\epsilon_{G,G'}(q, \omega = 0)$ is calculated on a $2 \times 2 \times 24$ q grid. The frequency dependent screening is incorporated by the Hybertson-Louie GPP model [50]. The cutoff energy for the (quasiparticle) wavefunctions is 60 Ry, and the cutoff energy for the dielectric function is 10 Ry as the screened coulomb interaction distribution function is in general smoother than the charge density distribution which is related to the wavefunctions. The calculation parameters have been tested to converge the quasiparticle band structure to within $\sim 0.1$ eV.

We also self-consistently update the quasiparticle energy eigenvalues in the Green's function, $G$, when building the self-energy operator $\Sigma$. The Green's function as a function of energy $\omega$ has the quasiparticle energy eigenvalues in its denominator

$$G(\omega) = \sum_{n\boldsymbol{k}} \frac{\psi_{n\boldsymbol{k}} \psi^*_{n\boldsymbol{k}}}{\omega - \epsilon_{n\boldsymbol{k}}}. \tag{6.1}$$

In the one-shot $G_0W_0$ calculation, the energy eigenvalues $\epsilon_{n\boldsymbol{k}}$ are taken to be the DFT energy eigenvalues. We plug in energy eigenvalues calculated by $G_0W_0$ as $\epsilon_{n\boldsymbol{k}}$ and do the iteration to get converged quasiparticle energy eigenvalues. The result of $n$-th iteration is denoted as $G_nW_0$ and the converged value for the quasiparticle energy eigenvalues is denoted as $GW_0$ energy eigenvalues. As shown by Fig. 6.4, the quasiparticle gap for the structure with layer shift parameter being 0.5 has a $G_0W_0$ band gap of $\sim 2.03$ eV and a $GW_0$ gap of $\sim 2.20$ eV. The quasiparticle energy eigenvalues are converged after three iterations, and the $GW_0$ gap is about 10 % larger than the $G_0W_0$ gap.

We have also tested that there is no need to update the wavefunction in the $GW$ calculation by the fact that the magnitude of the off-diagonal matrix element for the self-energy operator $\langle \psi_{n\boldsymbol{k}} | \Sigma | \psi_{m\boldsymbol{k}} \rangle$ are all less than 5% of the energy difference between the diagonal matrix elements, $| \langle \psi_{n\boldsymbol{k}} | \Sigma | \psi_{n\boldsymbol{k}} \rangle - \langle \psi_{m\boldsymbol{k}} | \Sigma | \psi_{m\boldsymbol{k}} \rangle |$ , which means the wavefunction calculated by DFT is already a very good approximation to the quasiparticle wavefunctions within the GW approximation.

The $GW_0$ quasiparticle band structure for the crystalline PPV with layer shift parameter being 0.5 and 0.18 are shown in Fig. 6.5 and Fig. 6.7, respectively. The $GW_0$ band gap of the system with layer shift of 0.5 is 2.20 eV, while the $GW_0$ band gap of the system with layer shift of 0.18 is 2.09 eV. In most part of the BZ, the $2p+1$ and $2p+2$ th bands ($p$ is an integer) counting from the Fermi level are close in energy, and their wavefunction characters are similar, and this is due to the two chains inside one unit cell of the crystalline PPV. If we group the $2p+1$ and $2p+2$ th conduction or valence bands in pairs, the first (second) set of conduction bands and valence bands are mostly contributed from the extended states located at the carbon-carbon double bounds (narrow-band states localized mostly at the benzene rings) (Fig. 6.5, 6.6 and

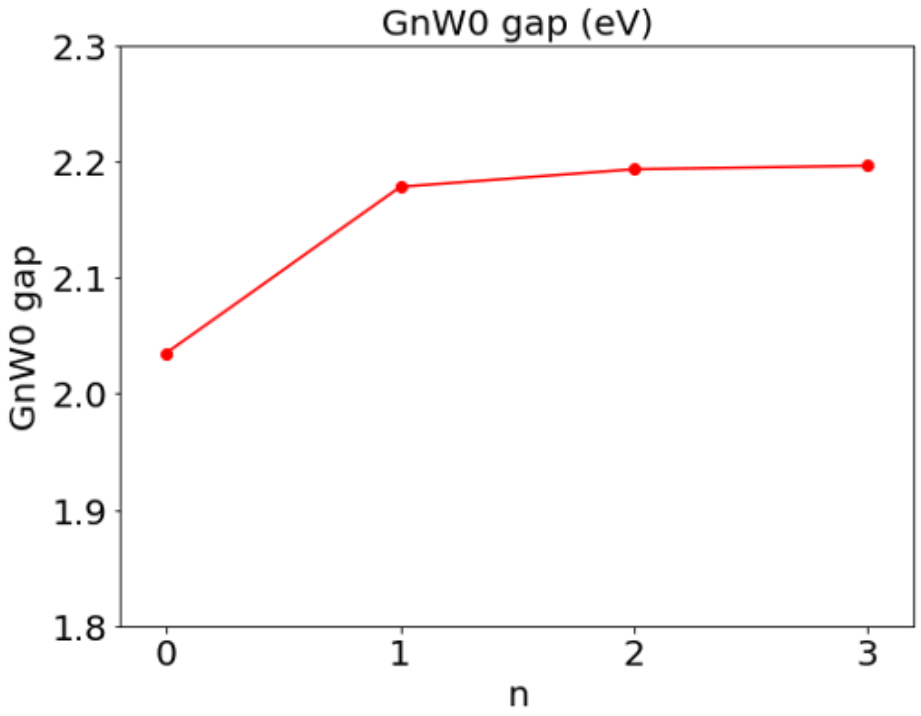


Figure 6.4: The quasiparticle band gap as a function of iteration number $n$ in $G_nW_0$ calculations for structure with layer shift being 0.5. We stop at the $G_3W_0$ level at which the self-consistency is reached. The $GW_0$ gap is 2.2 eV, which is about 10 % larger than the $G_0W_0$ gap.

6.7). The gap for the structure with 0.18 layer shift is only slightly ($\sim 0.1eV$) smaller than that of the structure with 0.5 layer shift, but the energy splitting between the bands within a pair (Fig. 6.5 and 6.7) at the Y point is larger than that of the structure with 0.5 layer shift.

### 6.2.4 Optical absorption spectra

Figure. 6.8 shows the calculated absorption spectrum by GW-BSE formalism for the crystalline PPV with layer shift parameter being 0.5, comparing with the measured absorption spectrum on the crystalline PPV sample with chain length of $\sim$ 90 Å at the room temperature (taken from Ref. [42] ). We used the Tamm-Dancoff approximation (TDA) [8, 33] which ignores anti-electron-hole excitation in the BSE calculation. Transitions from the top 22 valence bands to the bottom 22 conduction bands has been included in the diagonalization of the BSE, and the number of bands have been tested to converge the optical absorption spectrum in the energy range from 0 eV at least up to 7 eV. We can clearly see three major peaks in the calculated absorption spectrum (Fig. 6.8). The first two major peaks agree well with the measured first two peaks: the

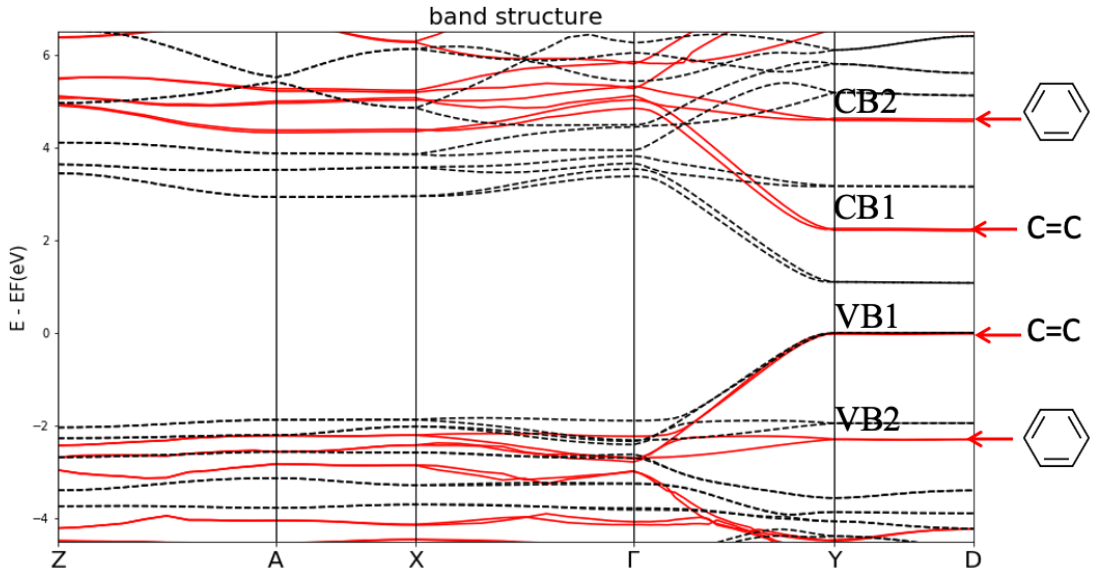


Figure 6.5: Quasiparticle band structure of a crystalline PPV with layer shift = 0.5. The red solid line and black dashed line show the $GW_0$ band structure and the DFT-LDA band structure, respectively. The first and second set of valence bands (conduction bands) are marked VB1 and VB2 (CB1 and CB2), respectively. One set contains two bands due to two PPV chains inside one unit cell. The first (second) set of conduction bands and valence bands are mostly contributed from the extended state located at the carbon-carbon double bounds (narrow-band states localized at the benzene rings).

calculated first major peak is $\sim 0.3$ eV lower than the measured first peak while the calculated second major peak agrees with the measured second peak within $\sim 0.2$ eV. The calculated third major peak is about 1 eV higher than the measured third peak, so the third major peak is not well explained in the BSE calculation with TDA.

The three major peaks are mainly contributed from exciton states associated with different interband transitions. The first peak is mainly contributed from exciton states associated with transitions from the first set of valence bands to the first set of conduction bands (Fig. 6.5 and Fig. 6.8 ). The second and third peak are mainly contributed from exciton states associated with transitions from the second set of valence bands to the first set of conduction bands and the transitions from the second set of valence bands to the second set of conduction bands, respectively (Fig. 6.5 and Fig. 6.8 ). The exciton states in the three peaks have the largest contribution from the electron-hole transitions for states along the Y-D line of the BZ, and the transition energies of the transitions contributing most for the three major peaks are listed in Fig. 6.9. We could estimate that the exciton binding energy for exciton states in the three major peaks are $\sim 0.1$ eV.

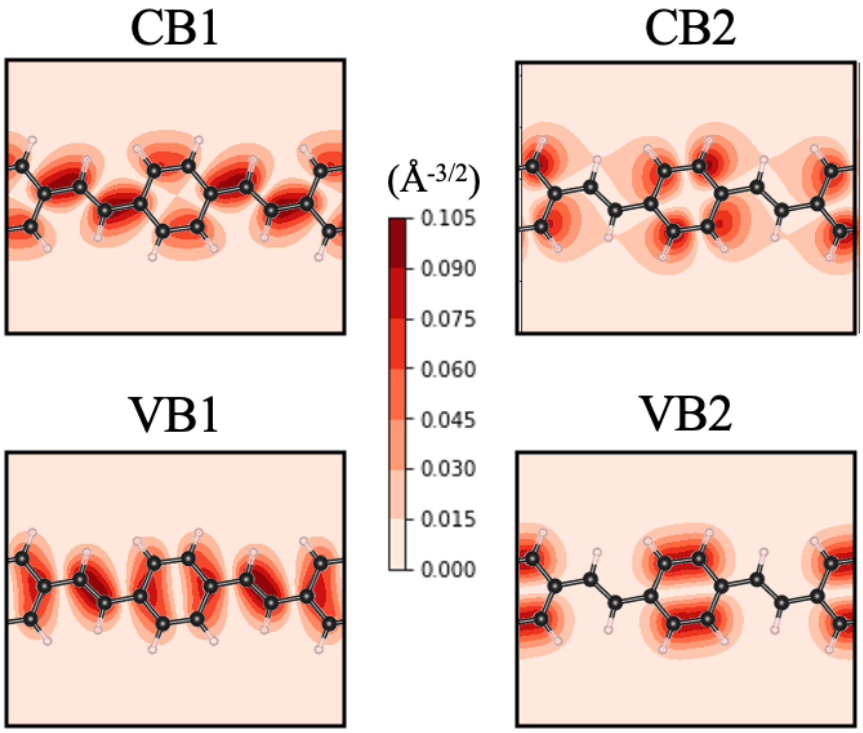


Figure 6.6: The contour map plot of the absolute value of the wavefunction at Y point. The wavefunction is plotted at a plane 1 Å above the PPV chain molecular plane.

The GW-BSE calculation performed for crystalline PPV includes the screening effect of other chains in the bulk PPV samples which is absent in a single chain calculation. Table 6.1 shows the calculated LDA gap, $G_0W_0$ gap, $GW_0$ gap, optical gap and exciton binding energy calculated for single chain and for crystalline PPV with layer shift parameter being 0.18 and 0.5. The LDA gap of a single chain PPV is $\sim$ 20 % larger than that of the crystalline PPV, and the $G_0W_0$ gap of a single chain is almost 2 times that of the crystalline PPV, showing much less screening effect in the single chain calculation comparing to the crystalline PPV calculation. The exciton binding energy for the dominant bright excitons in the first peak in the single chain calculation (1.68 eV) is much larger than the binding energy in the crystalline calculation. Combining the two effects (larger quasiparticle gap and larger binding energy), the optical gap of single chain PPV calculation is similar to the optical gap for crystalline PPV (Table 6.1).

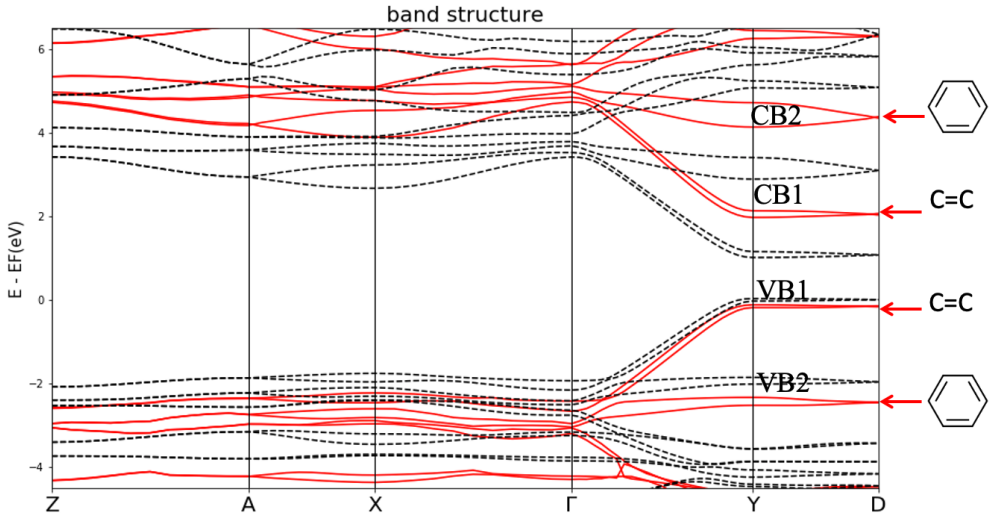


Figure 6.7: Quasiparticle band structure of crystalline PPV with layer shift = 0.18. (a) The red solid line and black dashed line show the GW0 band structure and the DFT-LDA band structure, respectively. The first and second set of valence bands (conduction bands) are marked VB1 and VB2 (CB1 and CB2), respectively. One set contains two bands due to two PPV chains inside one unit cell. The first (second) set of conduction bands and valence bands are mostly contributed from the extended state located at the carbon-carbon double bounds (narrow-band states localized at the benzene rings).

| (eV) | LDA gap | $G_0W_0$ gap | $GW_0$ gap | Optical gap | $E_b$ |
|---|---|---|---|---|---|
| Single chain | 1.23 | 3.68 | | 2.00 [1] | 1.68 |
| Crystalline (shift 0.18) | 0.96 | 1.94 | 2.09 | 2.01 | 0.08 |
| Crystalline (shift 0.5) | 1.07 | 2.04 | 2.20 | 2.09 | 0.11 |

Table 6.1: The LDA gap, $G_0W_0$ gap, $GW_0$ gap, optical gap and exciton binding energy calculated for single chain and crystalline PPV with layer shift parameter being 0.18 and 0.5. [1] The 2.00 eV optical gap for single chain PPV is calculated from the $G_0W_0$ quasiparticle band structure. The binding energy $E_b$ for a single chain is defined as the $G_0W_0$ gap minus the optical gap because we did not calculate $GW_0$ gap for a single chain. The bindin energy $E_b$ for crystalline PPV is defined as the $GW_0$ gap minus the optical gap.

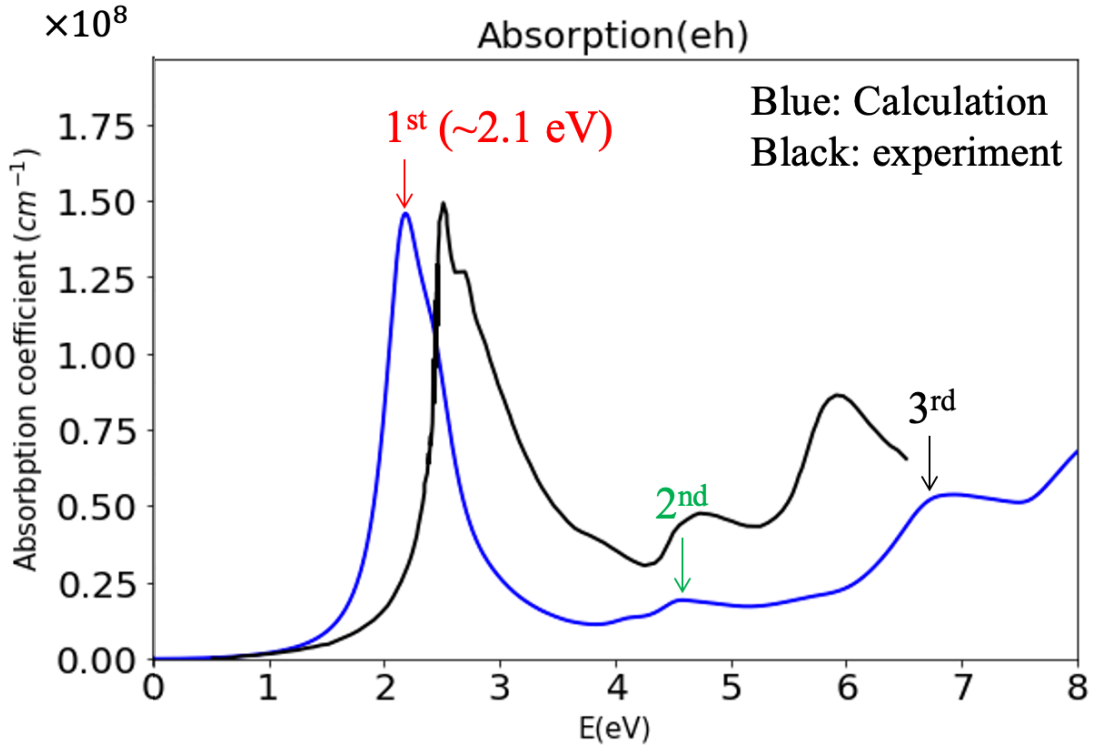


Figure 6.8: Blue line: calculated absorption spectrum for the crystalline PPV with layer shift parameter = 0.5 by GW-BSE starting from DFT-LDA. Black line: the measured absorption spectra on the crystalline PPV sample with chain length of $\sim 90$ Å(data taken from Ref. [42] ). The three major peaks are indicated by red, green and black arrows. The measured spectra are in arbitrary unit (not to the same scale marked on the vertical axis). A 0.2 eV Gaussian broadening is used in the calculated absorption spectrum.

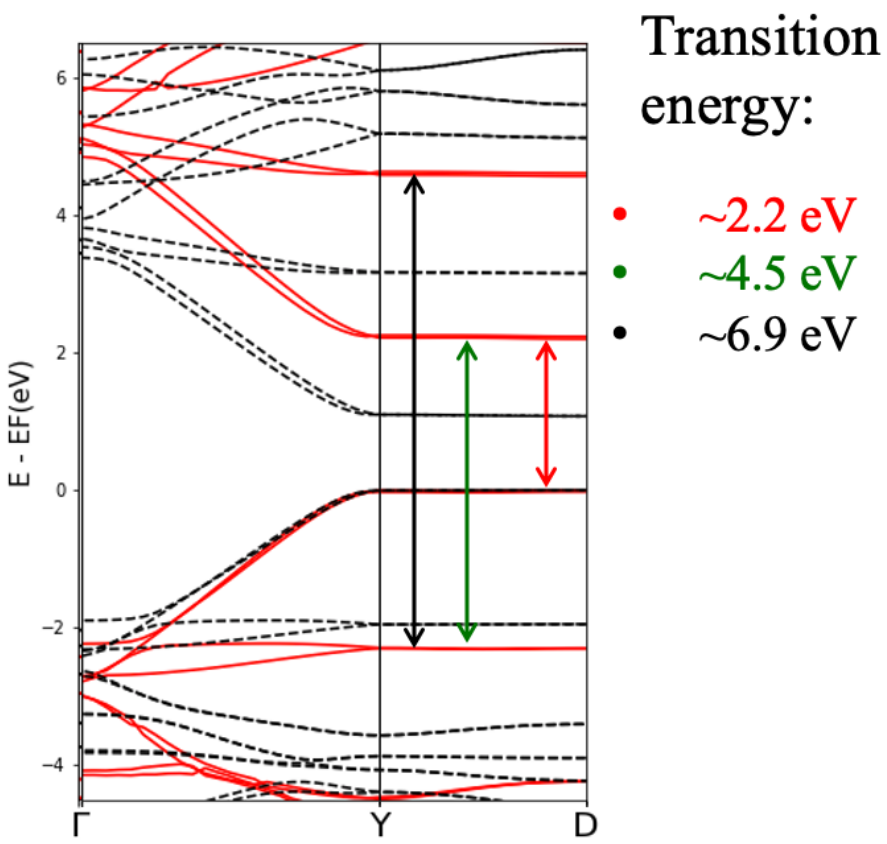


Figure 6.9: The $GW_0$ quasiparticle band structure showing the transitions contributing to the three major peaks in Fig. 6.8.

#### 6.2.4.1 Peak height

We also note that the relative height of the third major peak in the calculated optical absorption spectrum is much lower than that in the measured spectrum. This can be explained by the finite chain length of the PPV chains in the samples [42]. Figure 6.10 shows the measured absorption spectra using crystalline PPV samples with different qualities (chain length). The sample with longer chains shows relative higher first major peak and lower third peak. This is due to the fact that the transitions contributing to the first major peak are from electronic states more uniformly extended along the PPV chain, and if the sample chain length is not long enough and varying, those electronic states would differ in energy. The exciton states contributing the first peak are suppressed because the different segments of different length have different energies and the cannot easily form a coherent exciton state. Thus, the longer the chain is, the lower relative peak height the third peak will have. In the calculation, the chain length is infinite, so the calculated third peak would be relatively lower in height comparing to the experimental results.

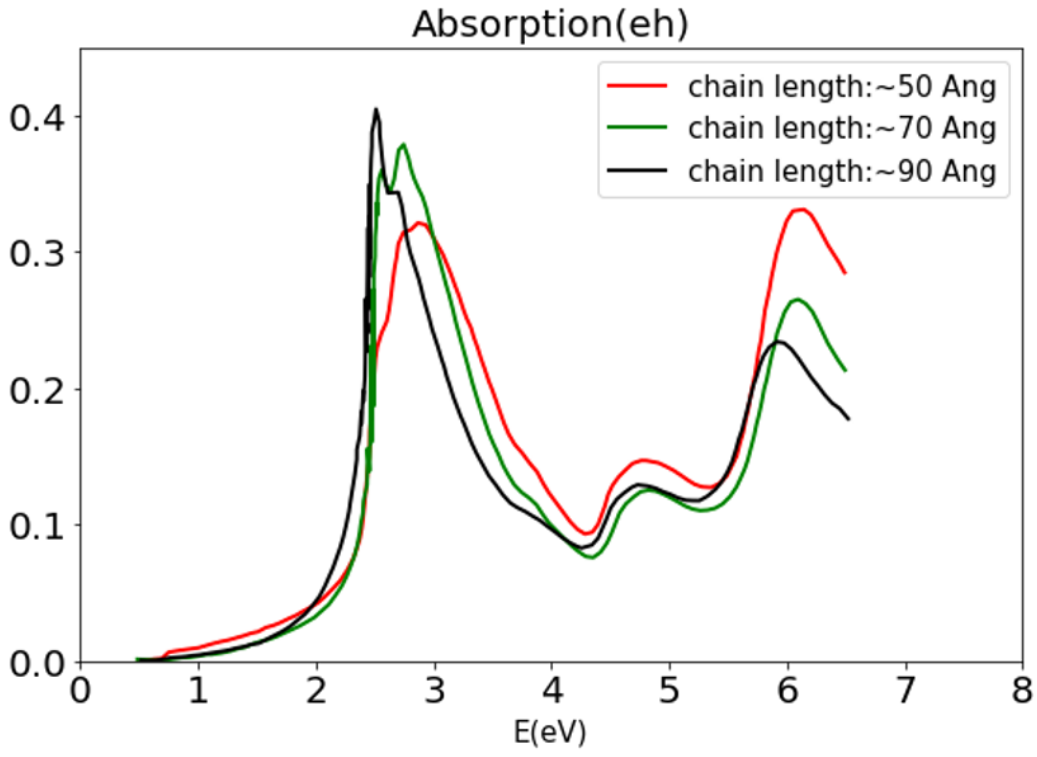


Figure 6.10: The measured absorption spectra on the crystalline sample with a chain length of $\sim$ 50 Å(red line), $\sim$ 70 Å(green line), and $\sim$ 90 Å(black line) (data taken from Ref. [42] ). The absorbance curve for different samples are not plotted to the same scale.

#### 6.2.4.2 Tam-Dancoff approximation

We have also investigated in effect of the TDA on the calculated absorption spectrum. Figure 6.11 shows the calculated spectrum of crystalline PPV with layer shift parameter being 0.5. Comparing with the calculation with TDA, the full calculation gives all the three major peak a red shift by an amount of $\sim 0.3$ eV. The energy positions for the three peaks are $\sim 1.8$ eV, $\sim 4.2$ eV, and $\sim 6.5$ eV, respectively. The energy position of the third peak matches the experimental results better, but the energy of the first peak is underestimated by about 0.6 eV. Comparing with the calculation with TDA, the absorption percentage is also decreased by about 20 percent. The TDA ignores the anti-excitation (anti-electron-hole pairs) in the BSE, and this calculation shows that the effects from anti-electron-hole pairs in the optical excitation of crystalline PPV are important. The energy mismatch of the peak positions between the calculations and the experiments still need further investigations.

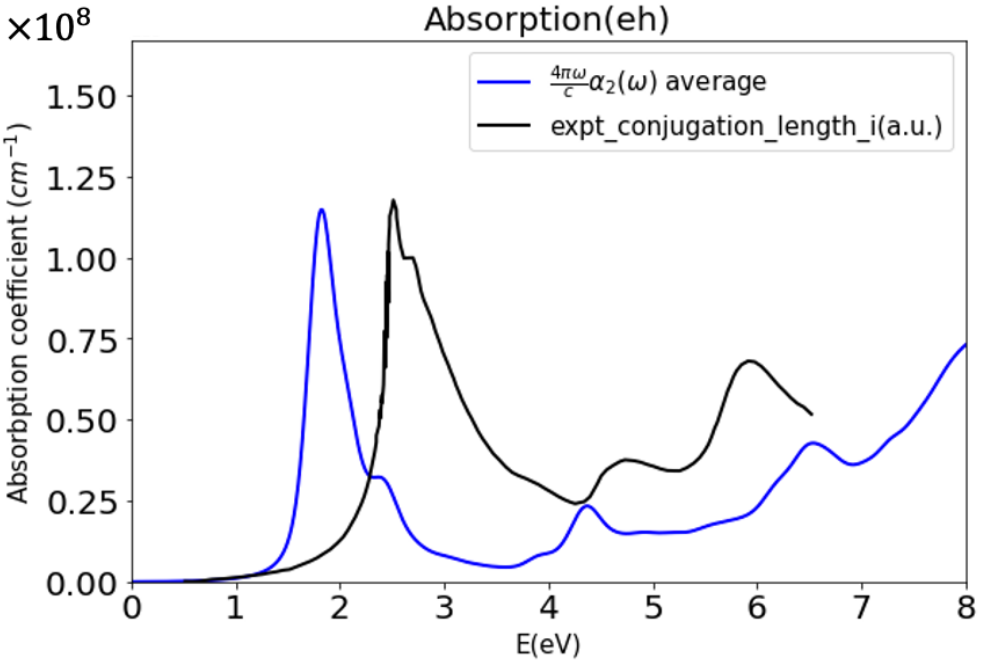


Figure 6.11: Blue line: The calculated absorption spectrum of crystalline PPV with layer shift parameter being 0.5. Black line: the measured absorption spectra on the crystalline PPV sample with chain length of $\sim 90$ Å(data taken from Ref. [42] ). The calculation solves the full BSE without the TDA. The measured spectra are plotted using an arbitrary unit (not to the same scale marked on the vertical axis). A 0.2 eV Gaussian broadening is used in the calculated absorption spectrum.

### 6.2.5 GW-BSE calculations starting from DFT with different exchange-correlation functionals

We further investigate the dependence of the GW-BSE calculation of the crystalline PPV optical absorption on the exchange-correlation functionals used in its DFT starting point. Table 6.2 shows the DFT gap calculated using LDA, PBE [83], and the strongly constrained and appropriately normed (SCAN) [104] functionals. The $GW_0$ gap, gap increase $E_g^{GW_0} - E_g^{DFT}$, and the "head" element of dielectric function $\epsilon_{0,0}(\boldsymbol{q})$ calculated using those exchange-correlation functionals as the starting point are also shown in Table 6.2. The subscript in $\epsilon_{0,0}(\boldsymbol{q})$ means $\boldsymbol{G} = \boldsymbol{G}' = 0$ [51, 50, 49, 115]. $\boldsymbol{q}$ is the wavevector commensurate with the size of the envelope wavefunctions of the exciton state with the highest oscillator strength in the first peak of the optical absorption spectrum, so $\epsilon_{0,0}(\boldsymbol{q})$ shows the strength of screening effect on the exciton states in the first major peak.

The SCAN functional gives the largest DFT gap, and SCAN functional ground state would have weaker screening. This is demonstrated in the "head" element of dielectric function $\epsilon_{0,0}(\boldsymbol{q})$. However, the $GW_0$ gaps calculated for different functionals as starting point agrees within 0.04 eV, so this shows that the quasiparticle gap produced by the $GW_0$ calculation are quite independent of mean field DFT starting points for this system. We note that the gap increase $E_g^{GW_0} - E_g^{DFT}$ comparing the $GW_0$ gap with the DFT gap are proportional to the screening effect indicated by $\epsilon_{0,0}(\boldsymbol{q})$, and this needs to be further investigated.

Figure. 6.12 (b) shows the optical absorption spectra calculated by GW-BSE using LDA and SCAN functional DFT starting points, with all the other calculation parameters set to be the same. We see that the two calculated absorption spectra sit almost on top of each other, thus we conclude that the GW-BSE calculation of the absorption spectrum of crystalline PPV depends weakly on its mean field DFT starting point.

In conclusion, we have explained the mismatch of the relative peak height of the three major optical absorption spectrum peaks between the calculations and the experiments, given that the third peak measured in the experiment is coming from the exciton states associated with transitions from narrow bands formed by less extended benzene states. The peak energy of the third peak is still overestimated, and it requires further investigation including the effect of TDA used in the calculation and so on.

## 6.3 Development for the interface code between Quantum ESPRESSO and BerkeleyGW

The GW-BSE calculation in the previous section involves the GW-BSE calculation starting from the SCAN functional which is a meta-GGA functional. The DFT calculations are performed by the Quantum ESPRESSO (QE) [37] package, while the GW-BSE calcaulations are performed by the BerkeleyGW [31] package. Feeding the DFT calculation data from QE to BerkeleyGW is done by the interface code, *pw2bgw.x*.

| (eV) | DFT gap | $GW_0$ gap | Gap increase | $\epsilon_{0,0}(q)$ (q = (0, 0, 0,1667) ) |
|---|---|---|---|---|
| LDA | 1.07 | 2.20 | 1.13 | 13.52 |
| PBE | 1.13 | 2.23 | 1.10 | 12.87 |
| SCAN | 1.20 | 2.19 | 0.99 | 12.10 |

Table 6.2: GW-BSE calculation starting from DFT using different exchange-correlation functionals. (a) The calculated DFT gap, $GW_0$ gap and the "head" element of dielectric function $\epsilon_{0,0}(\boldsymbol{q})$ using LDA, PBE and SCAN functionals. $\boldsymbol{q}$ is the wavevector commensurate with the size of the envelope wavefunction of the exciton state with the highest oscillator strength in the first peak.

However, the interface code did not support feeding data from meta-GGA DFT calculation previously. Therefore, we have developed an interface code to make it compatible with DFT calculations with all kinds of meta-GGA functionals, as well as all kinds of hybrid functionals. This development has enabled GW-BSE calculation by the BerkeleyGW package starting from the mean field DFT calculation with all kinds of meta-GGA and hybrid functionals by the QE package. The development also supports spinless, collinear spin, and noncollinear spin calculations. Below we show the detailed developed new features in the interface code, *pw2bgw.x*.

In the DFT mean field calculation performed by a typical DFT code, the band energy is separated into four parts

$$E^{mf}_{n\boldsymbol{k}} = E^{Kinetic}_{n\boldsymbol{k}} + E^{Ion}_{n\boldsymbol{k}} + E^{Hartree}_{n\boldsymbol{k}} + V^{xc}_{n\boldsymbol{k}}, \tag{6.2}$$

where $E^{Kinetic}_{n\boldsymbol{k}}$ is the kinetic energy, $E^{Ion}_{n\boldsymbol{k}}$ is the ionic potential energy containing the electron-ion interaction energy represented by the local and non-local part of the pseudopotential [24, 71], $E^{Hartree}_{n\boldsymbol{k}}$ is the Hartree energy, and $V^{xc}_{n\boldsymbol{k}}$ is the exchange-correlation energy.

The BerkeleyGW package calculates the self energy matrix element $\langle n\boldsymbol{k}| \Sigma |n\boldsymbol{k}\rangle$, so that the quasiparticle band energy could be calculate by the formula below

$$E^{qp}_{n\boldsymbol{k}} = E^{Kinetic}_{n\boldsymbol{k}} + E^{Ion}_{n\boldsymbol{k}} + E^{Hartree}_{n\boldsymbol{k}} + \langle n\boldsymbol{k}| \Sigma |n\boldsymbol{k}\rangle \,. \tag{6.3}$$

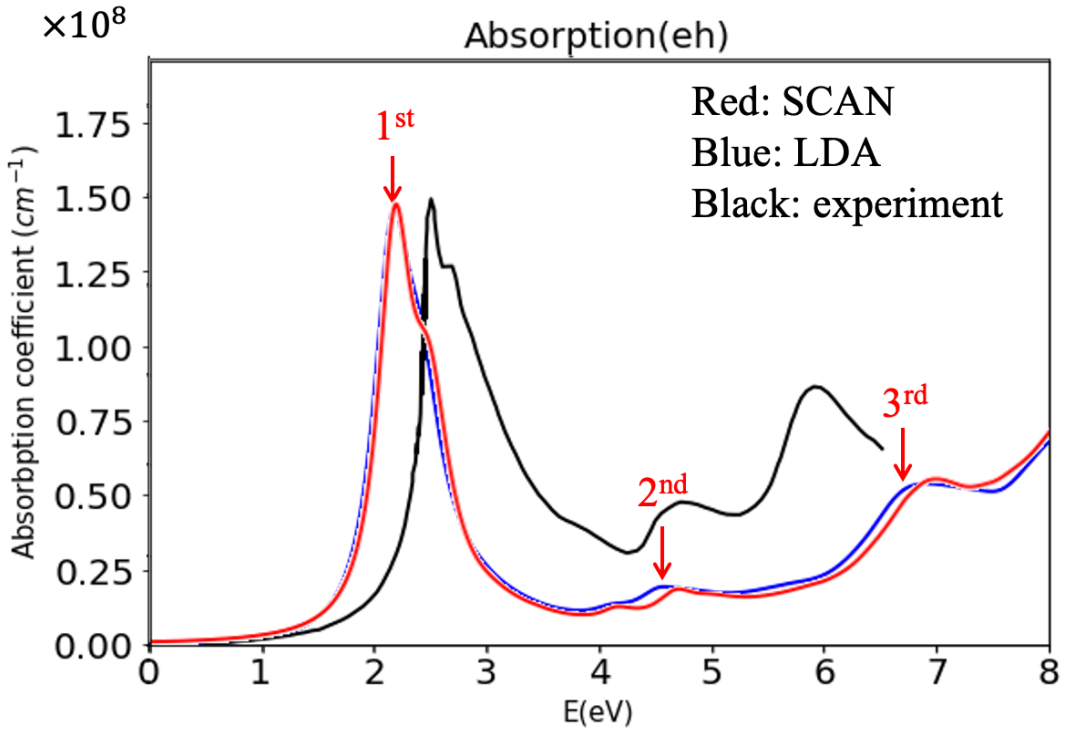


Figure 6.12: GW-BSE calculation starting from DFT using different exchange-correlation functionals. The GW-BSE absorption spectra calculated starting from SCAN and LDA exchange-correlation functionals (compared with the measured absorption spectra). The measured spectra are plotted using an arbitrary unit (not to the same scale marked on the vertical axis). A 0.2 eV Gaussian broadening is used in the calculated absorption spectra.

Previously, the *pw2bgw.x* interface code calculates the $V^{xc}_{n\boldsymbol{k}}$ part and feeds $V^{xc}_{n\boldsymbol{k}}$ into the BerkeleyGW code. The BerkeleyGW package does the subtraction of $V^{xc}_{n\boldsymbol{k}}$ from $E^{mf}_{n\boldsymbol{k}}$ and adds back the $\langle n\boldsymbol{k}|\,\Sigma\,|n\boldsymbol{k}\rangle$ term to construct the quasiparticle band energy $E^{qp}_{n\boldsymbol{k}}$. The calculation process is shown in the formula below

$$E^{qp}_{n\boldsymbol{k}} = E^{mf}_{n\boldsymbol{k}} - V^{xc}_{n\boldsymbol{k}} + \langle n\boldsymbol{k}|\,\Sigma\,|n\boldsymbol{k}\rangle\,. \tag{6.4}$$

The exchange-correlation energy $V^{xc}_{n\boldsymbol{k}}$ depends on the charge density $n(\boldsymbol{r})$, the gradient of charge density $\nabla n(\boldsymbol{r})$, the kinetic energy density $\tau(\boldsymbol{r})$ (for meta-GGA functionals), as well as some empirical parameter used in hybrid functionals [7, 47, 32]. As a result, the calculation of $V^{xc}_{n\boldsymbol{k}}$ would not only need merely the ground state charge density and ground state wavefunctions, and making a general interface code able to

| DFT Functionals | spin support |
|---|---|
| LDA, GGA, | spinless, collinear spin, noncollinear spin |
| MetaGGA | spinless, colinear spin, (noncollinear spin incompatible with metaGGA in Quantum ESPRESSO) |
| Hybrid functionals | spinless, colinear spin, noncollinear spin |

Table 6.3: The DFT functionals and type of spin schemes supported by the *pw2bgw.x* interface code. Black: Supported type of DFT functionals and type of spin schemes before the development. Red: Newly supported type of DFT functionals and type of spin schemes after the development.

handling all kinds of meta-GGA and hybrid functionals would need a large number of additional input parameters from the QE package other than the ground state wavefunctions (charge densities). This would take multiple subroutines for different cases and is error-prone.

Thus, we choose another way to calculate $E^{qp}_{n\boldsymbol{k}}$ which circumvents the direct calculation of the exchange-correlation energy $V^{xc}_{n\boldsymbol{k}}$. We directly calculate the first three terms in the band energy, namely the kinetic energy, ionic energy and Hartree energy, which only depends on the ground state wavefunctions. We define the sum of these three part as "KIH" energy:

$$E^{KIH}_{n\boldsymbol{k}} = E^{Kinetic}_{n\boldsymbol{k}} + E^{Ion}_{n\boldsymbol{k}} + E^{Hartree}_{n\boldsymbol{k}}. \tag{6.5}$$

Thus the quasiparticle band energy is evaluated in the way below:

$$E^{qp}_{n\boldsymbol{k}} = E^{KIH}_{n\boldsymbol{k}} + \langle n\boldsymbol{k}| \Sigma |n\boldsymbol{k}\rangle . \tag{6.6}$$

The calculation of the "KIH" energy $E^{KIH}_{n\boldsymbol{k}}$ has been implemented in the new version of the interface code, *pw2bgw.x*, and this new version of *pw2bgw.x* will be released for public use in BerkeleyGW version 3.0 in 2021.

Before the development, the interface code *pw2bgw.x* only supports the GW-BSE calculation by the BerkeleyGW package using mean field DFT results with LDA and GGA exchange-correlation functionals calculated from the QE package, and it only supports spinless calculation, nonlinear spin calculation and noncollinear spin calculation in limited ways. (The *pw2bgw.x* could feed the BerkeleyGW package with the matrix elements of exchange-correlation potential $V^{xc}_{n\boldsymbol{k}}$ or the special dependent potential itself $V^{xc}(\boldsymbol{r})$, the previous *pw2bgw.x* could support the latter way in the spinor calculation. The former way is now supported in the new version of *pw2bgw.x*. )

The new version of the interface code *pw2bgw.x* supports GW-BSE calculation by the BerkeleyGW package using the ground state calculated by DFT using all kinds of meta-GGA and hybrid functionals, for spinless, collinear spin and noncollinear spin calculations (except for the noncollinear calculation for the meta-GGA functionals which is not implemented in the QE package).

This development is useful for first-principles calculations of the excited properties using the GW-BSE formalism starting from ground states calculated by different DFT exchange-correlation functionals.

# Bibliography


[1] LB Abdalla et al. "Topological phase transitions of (BixSb1- x) 2Se3 alloys by density functional theory". In: *Journal of Physics: Condensed Matter* 27.25 (2015), p. 255501.

[2] Sapan Agarwal and Eli Yablonovitch. "Band-edge steepness obtained from Esaki backward diode current–voltage characteristics". In: *IEEE Transactions on Electron Devices* 61.5 (2014), pp. 1488–1493.

[3] Gabriel Antonius and Steven G Louie. "Temperature-induced topological phase transitions: promoted versus suppressed nontrivial topology". In: *Physical review letters* 117.24 (2016), p. 246401.

[4] AC Arias et al. "The use of tin oxide thin films as a transparent electrode in PPV based light-emitting diodes". In: *Thin Solid Films* 371.1-2 (2000), pp. 201–206.

[5] János K Asbóth, László Oroszlány, and András Pályi. "A short course on topological insulators". In: *Lecture notes in physics* 919 (2016), pp. 997–1000.

[6] Ryan Barnett. "Edge-state instabilities of bosons in a topological band". In: *Physical Review A* 88.6 (2013), p. 063631.

[7] Axel D Becke. "A new mixing of Hartree–Fock and local density-functional theories". In: *The Journal of chemical physics* 98.2 (1993), pp. 1372–1377.

[8] Lorin X Benedict, Eric L Shirley, and Robert B Bohn. "Optical absorption of insulators and the electron-hole interaction: An ab initio calculation". In: *Physical review letters* 80.20 (1998), p. 4514.

[9] Lennart Bengtsson. "Dipole correction for surface supercell calculations". In: *Physical Review B* 59.19 (1999), p. 12301.

[10] Patrick B Bennett et al. "Bottom-up graphene nanoribbon field-effect transistors". In: *Applied Physics Letters* 103.25 (2013), p. 253114.

[11] Hans Bethe. "Zur theorie der metalle". In: *Zeitschrift für Physik* 71.3-4 (1931), pp. 205–226.

[12] EI Blount. "Formalisms of band theory". In: *Solid state physics*. Vol. 13. Elsevier, 1962, pp. 305–373.

[13] DDC Bradley. "Precursor-route poly (p-phenylenevinylene): polymer characterisation and control of electronic properties". In: *Journal of physics D: Applied physics* 20.11 (1987), p. 1389.

[14] DDC Bradley et al. "Structural studies of oriented precursor route conjugated polymers". In: *Synthetic Metals* 17.1-3 (1987), pp. 473–478.

[15] Donal DC Bradley. "Characterisation of polymers for semiconductor applications". In: *Polymer international* 26.1 (1991), pp. 3–16.

[16] Christopher Bronner et al. "Aligning the band gap of graphene nanoribbons by monomer doping". In: *Angewandte Chemie* 125.16 (2013), pp. 4518–4521.

[17] Christopher Bronner et al. "Hierarchical on-surface synthesis of graphene nanoribbon heterojunctions". In: *ACS nano* 12.3 (2018), pp. 2193–2200.

[18] Jinming Cai et al. "Atomically precise bottom-up fabrication of graphene nanoribbons". In: *Nature* 466.7305 (2010), pp. 470–473.

[19] Jinming Cai et al. "Graphene nanoribbon heterojunctions". In: *Nature nanotechnology* 9.11 (2014), p. 896.

[20] Arrigo Calzolari et al. "Ab initio transport properties of nanostructures from maximally localized Wannier functions". In: *Physical Review B* 69.3 (2004), p. 035108.

[21] Ting Cao, Fangzhou Zhao, and Steven G Louie. "Topological phases in graphene nanoribbons: junction states, spin centers, and quantum spin chains". In: *Physical review letters* 119.7 (2017), p. 076401.

[22] Eduard Carbonell-Sanromà et al. "Quantum dots embedded in graphene nanoribbons by chemical substitution". In: *Nano letters* 17.1 (2017), pp. 50–56.

[23] Y-H Chan et al. "Ca 3 P 2 and other topological semimetals with line nodes and drumhead surface states". In: *Physical Review B* 93.20 (2016), p. 205132.

[24] James R Chelikowsky and Marvin L Cohen. "Nonlocal pseudopotential calculations for the electronic structure of eleven diamond and zinc-blende semiconductors". In: *Physical Review B* 14.2 (1976), p. 556.

[25] Dong Chen et al. "A structural study of poly (p-phenylene vinylene)". In: *Polymer* 33.15 (1992), pp. 3116–3122.

[26] Yen-Chia Chen et al. "Molecular bandgap engineering of bottom-up synthesized graphene nanoribbon heterojunctions". In: *Nature nanotechnology* 10.2 (2015), pp. 156–160.

[27] Yen-Chia Chen et al. "Tuning the band gap of graphene nanoribbons synthesized from molecular precursors". In: *ACS nano* 7.7 (2013), pp. 6123–6128.

[28] Feng-Chuan Chuang et al. "Tunable topological electronic structures in Sb (111) bilayers: A first-principles study". In: *Applied Physics Letters* 102.2 (2013), p. 022424.

[29] Ryan R Cloke et al. "Site-specific substitutional boron doping of semiconducting armchair graphene nanoribbons". In: *Journal of the American Chemical Society* 137.28 (2015), pp. 8872–8875.

[30] Pierre Delplace, D Ullmo, and G Montambaux. "Zak phase and the existence of edge states in graphene". In: *Physical Review B* 84.19 (2011), p. 195452.

[31] Jack Deslippe et al. "BerkeleyGW: A massively parallel computer package for the calculation of the quasiparticle and optical properties of materials and nanostructures". In: *Computer Physics Communications* 183.6 (2012), pp. 1269–1289.

[32] Matthias Ernzerhof and Gustavo E Scuseria. "Assessment of the Perdew–Burke–Ernzerhof exchange-correlation functional". In: *The Journal of chemical physics* 110.11 (1999), pp. 5029–5036.

[33] Alexander L Fetter and John Dirk Walecka. *Quantum theory of many-particle systems*. Courier Corporation, 2012.

[34] Niklas Friedrich et al. "Magnetism of topological boundary states induced by boron substitution in graphene nanoribbons". In: *Physical Review Letters* 125.14 (2020), p. 146801.

[35] Liang Fu, Charles L Kane, and Eugene J Mele. "Topological insulators in three dimensions". In: *Physical review letters* 98.10 (2007), p. 106803.

[36] Mitsutaka Fujita et al. "Peculiar localized state at zigzag graphite edge". In: *Journal of the Physical Society of Japan* 65.7 (1996), pp. 1920–1923.

[37] Paolo Giannozzi et al. "QUANTUM ESPRESSO: a modular and open-source software project for quantum simulations of materials". In: *Journal of physics: Condensed matter* 21.39 (2009), p. 395502.

[38] Thierry Granier et al. "Structure investigation of poly (p-phenylene vinylene)". In: *Journal of Polymer Science Part B: Polymer Physics* 24.12 (1986), pp. 2793–2804.

[39] Stefan Grimme. "Semiempirical GGA-type density functional constructed with a long-range dispersion correction". In: *Journal of computational chemistry* 27.15 (2006), pp. 1787–1799.

[40] Oliver Gröning et al. "Engineering of robust topological quantum phases in graphene nanoribbons". In: *Nature* 560.7717 (2018), pp. 209–213.

[41] Fabian Grusdt, Michael Höning, and Michael Fleischhauer. "Topological edge states in the one-dimensional superlattice Bose-Hubbard model". In: *Physical review letters* 110.26 (2013), p. 260405.

[42] DA Halliday et al. "Extended $\pi$-conjugation in poly (p-phenylenevinylene) from a chemically modified precursor polymer". In: *Synthetic metals* 55.2-3 (1993), pp. 954–959.

[43] M Zahid Hasan and Charles L Kane. "Colloquium: topological insulators". In: *Reviews of modern physics* 82.4 (2010), p. 3045.

[44] Lars Hedin. "New method for calculating the one-particle Green's function with application to the electron-gas problem". In: *Physical Review* 139.3A (1965), A796.

[45] Lars Hedin and Stig Lundqvist. "Effects of electron-electron and electron-phonon interactions on the one-electron states of solids". In: *Solid state physics*. Vol. 23. Elsevier, 1970, pp. 1–181.

[46] Alan J Heeger et al. "Solitons in conducting polymers". In: *Reviews of Modern Physics* 60.3 (1988), p. 781.

[47] Jochen Heyd, Gustavo E Scuseria, and Matthias Ernzerhof. "Hybrid functionals based on a screened Coulomb potential". In: *The Journal of chemical physics* 118.18 (2003), pp. 8207–8215.

[48] Pierre Hohenberg and Walter Kohn. "Inhomogeneous electron gas". In: *Physical review* 136.3B (1964), B864.

[49] Mark S Hybertsen and Steven G Louie. "Ab initio static dielectric matrices from the density-functional approach. I. Formulation and application to semiconductors and insulators". In: *Physical Review B* 35.11 (1987), p. 5585.

[50] Mark S Hybertsen and Steven G Louie. "Electron correlation in semiconductors and insulators: Band gaps and quasiparticle energies". In: *Physical Review B* 34.8 (1986), p. 5390.

[51] Mark S Hybertsen and Steven G Louie. "First-principles theory of quasiparticles: calculation of band gaps in semiconductors and insulators". In: *Physical review letters* 55.13 (1985), p. 1418.

[52] Mari Ijäs et al. "Electronic states in finite graphene nanoribbons: Effect of charging and defects". In: *Physical Review B* 88.7 (2013), p. 075429.

[53] Roman Jackiw and Cláudio Rebbi. "Solitons with fermion number 1/2". In: *Physical Review D* 13.12 (1976), p. 3398.

[54] GE Jellison Jr, MF Chisholm, and SM Gorbatkin. "Optical functions of chemical vapor deposited thin-film silicon determined by spectroscopic ellipsometry". In: *Applied physics letters* 62.25 (1993), pp. 3348–3350.

[55] Jingwei Jiang and Steven G Louie. "Topology Classification using Chiral Symmetry and Spin Correlations in Graphene Nanoribbons". In: *Nano Letters* (2020).

[56] Robert O Jones and Olle Gunnarsson. "The density functional formalism, its applications and prospects". In: *Reviews of Modern Physics* 61.3 (1989), p. 689.

[57] Toshikaze Kariyado and Yasuhiro Hatsugai. "Symmetry-protected quantization and bulk-edge correspondence of massless Dirac fermions: Application to the fermionic Shastry-Sutherland model". In: *Physical Review B* 88.24 (2013), p. 245126.

[58] Shigeki Kawai et al. "Atomically controlled substitutional boron-doping of graphene nanoribbons". In: *Nature communications* 6.1 (2015), pp. 1–6.

[59] R Kersting et al. "Femtosecond site-selective probing of energy relaxing excitons in poly (phenylenevinylene): Luminescence dynamics and lifetime spectra". In: *The Journal of chemical physics* 106.7 (1997), pp. 2850–2864.

[60] K v Klitzing, Gerhard Dorda, and Michael Pepper. "New method for high-accuracy determination of the fine-structure constant based on quantized Hall resistance". In: *Physical review letters* 45.6 (1980), p. 494.

[61] Matthias Koch et al. "Voltage-dependent conductance of a single graphene nanoribbon". In: *Nature nanotechnology* 7.11 (2012), pp. 713–717.

[62] Walter Kohn and Lu Jeu Sham. "Self-consistent equations including exchange and correlation effects". In: *Physical review* 140.4A (1965), A1133.

[63] John Michael Kosterlitz and David James Thouless. "Ordering, metastability and phase transitions in two-dimensional systems". In: *Journal of Physics C: Solid State Physics* 6.7 (1973), p. 1181.

[64] Ryogo Kubo. "Statistical-mechanical theory of irreversible processes. I. General theory and simple applications to magnetic and conduction problems". In: *Journal of the Physical Society of Japan* 12.6 (1957), pp. 570–586.

[65] Yea-Lee Lee et al. "Topological Phases in Cove-Edged and Chevron Graphene Nanoribbons: Geometric Structures, Z 2 Invariants, and Junction States". In: *Nano letters* 18.11 (2018), pp. 7247–7253.

[66] Feng Liu. "Self-consistent tight-binding method". In: *Physical Review B* 52.15 (1995), p. 10677.

[67] Jianpeng Liu and David Vanderbilt. "Topological phase transitions in (Bi 1- x In x) 2 Se 3 and (Bi 1- x Sb x) 2 Se 3". In: *Physical Review B* 88.22 (2013), p. 224202.

[68] Junzhi Liu et al. "Toward cove-edged low band gap graphene nanoribbons". In: *Journal of the American Chemical Society* 137.18 (2015), pp. 6097–6103.

[69] Qihang Liu et al. "Switching a normal insulator into a topological insulator via electric field with application to phosphorene". In: *Nano letters* 15.2 (2015), pp. 1222–1228.

[70] Juan Pablo Llinas et al. "Short-channel field-effect transistors with 9-atom and 13-atom wide graphene nanoribbons". In: *Nature communications* 8.1 (2017), pp. 1–6.

[71] Steven G Louie, Sverre Froyen, and Marvin L Cohen. "Nonlinear ionic pseudopotentials in spin-density-functional calculations". In: *Physical Review B* 26.4 (1982), p. 1738.

[72] SJ Martin et al. "Linear and nonlinear optical properties of the conjugated polymers PPV and MEH-PPV". In: *Physical Review B* 59.23 (1999), p. 15133.

[73] Nicola Marzari and David Vanderbilt. "Maximally localized generalized Wannier functions for composite energy bands". In: *Physical review B* 56.20 (1997), p. 12847.

[74] M Meier, S Karg, and W Riess. "Light-emitting diodes based on poly-p-phenylene-vinylene: II. Impedance spectroscopy". In: *Journal of Applied Physics* 82.4 (1997), pp. 1961–1966.

[75] Bartomeu Monserrat and David Vanderbilt. "Temperature effects in the band structure of topological insulators". In: *Physical review letters* 117.22 (2016), p. 226801.

[76] Arash A Mostofi et al. "An updated version of wannier90: A tool for obtaining maximally-localised Wannier functions". In: *Computer Physics Communications* 185.8 (2014), pp. 2309–2310.

[77] Akimitsu Narita et al. "New advances in nanographene chemistry". In: *Chemical Society Reviews* 44.18 (2015), pp. 6616–6643.

[78] Giang D Nguyen et al. "Atomically precise graphene nanoribbon heterojunctions from a single molecular precursor". In: *Nature nanotechnology* 12.11 (2017), p. 1077.

[79] Giang D Nguyen et al. "Bottom-up synthesis of N= 13 sulfur-doped graphene nanoribbons". In: *The Journal of Physical Chemistry C* 120.5 (2016), pp. 2684–2687.

[80] Ian D Parker. "Carrier tunneling and device characteristics in polymer light-emitting diodes". In: *Journal of Applied Physics* 75.3 (1994), pp. 1656–1666.

[81] Zahra Pedramrazi et al. "Concentration dependence of dopant electronic structure in bottom-up graphene nanoribbons". In: *Nano letters* 18.6 (2018), pp. 3550–3556.

[82] John P Perdew. "Density-functional approximation for the correlation energy of the inhomogeneous electron gas". In: *Physical Review B* 33.12 (1986), p. 8822.

[83] John P Perdew, Kieron Burke, and Matthias Ernzerhof. "Generalized gradient approximation made simple". In: *Physical review letters* 77.18 (1996), p. 3865.

[84] K Pichler et al. "Optical spectroscopy of highly ordered poly (p-phenylene vinylene)". In: *Journal of Physics: Condensed Matter* 5.38 (1993), p. 7155.

[85] Mohammad Mehdi Pour et al. "Laterally extended atomically precise graphene nanoribbons with improved electrical conductivity for efficient gas sensing". In: *Nature communications* 8.1 (2017), pp. 1–9.

[86] Emil Prodan and Hermann Schulz-Baldes. "Bulk and boundary invariants for complex topological insulators: From K-Theory to Physics". In: *Mathematical Physics Studies* (2016).

[87] Xiao-Liang Qi and Shou-Cheng Zhang. "Topological insulators and superconductors". In: *Reviews of Modern Physics* 83.4 (2011), p. 1057.

[88] Jun-Won Rhim, Jan Behrends, and Jens H Bardarson. "Bulk-boundary correspondence from the intercellular Zak phase". In: *Physical Review B* 95.3 (2017), p. 035421.

[89] Daniel J Rizzo et al. "Inducing metallicity in graphene nanoribbons via zero-mode superlattices". In: *Science* 369.6511 (2020), pp. 1597–1603.

[90] Daniel J Rizzo et al. "Topological band engineering of graphene nanoribbons". In: *Nature* 560.7717 (2018), pp. 204–208.

[91] Michael Rohlfing and Steven G Louie. "Electron-hole excitations and optical spectra from first principles". In: *Physical Review B* 62.8 (2000), p. 4927.

[92] Michael Rohlfing and Steven G Louie. "Optical excitations in conjugated polymers". In: *Physical review letters* 82.9 (1999), p. 1959.

[93] L Rossi et al. "Influence of alkoxy substituents on the exciton binding energy of conjugated polymers". In: *Synthetic metals* 111 (2000), pp. 527–530.

[94] Pascal Ruffieux et al. "Electronic structure of atomically precise graphene nanoribbons". In: *Acs Nano* 6.8 (2012), pp. 6930–6935.

[95] Pascal Ruffieux et al. "On-surface synthesis of graphene nanoribbons with zigzag edge topology". In: *Nature* 531.7595 (2016), pp. 489–492.

[96] Shinsei Ryu and Yasuhiro Hatsugai. "Entanglement entropy and the Berry phase in the solid state". In: *Physical review B* 73.24 (2006), p. 245115.

[97] MP Lopez Sancho, JM Lopez Sancho, and Jessy Rubio. "Quick iterative scheme for the calculation of transfer matrices: application to Mo (100)". In: *Journal of Physics F: Metal Physics* 14.5 (1984), p. 1205.

[98] José M Soler et al. "The SIESTA method for ab initio order-N materials simulation". In: *Journal of Physics: Condensed Matter* 14.11 (2002), p. 2745.

[99] Alexey A Soluyanov and David Vanderbilt. "Computing topological invariants without inversion symmetry". In: *Physical Review B* 83.23 (2011), p. 235401.

[100] Alexey A Soluyanov and David Vanderbilt. "Wannier representation of Z 2 topological insulators". In: *Physical Review B* 83.3 (2011), p. 035108.

[101] Young-Woo Son, Marvin L Cohen, and Steven G Louie. "Energy gaps in graphene nanoribbons". In: *Physical review letters* 97.21 (2006), p. 216803.

[102] Young-Woo Son, Marvin L Cohen, and Steven G Louie. "Half-metallic graphene nanoribbons". In: *Nature* 444.7117 (2006), pp. 347–349.

[103] W_P Su, JR Schrieffer, and Ao J Heeger. "Solitons in polyacetylene". In: *Physical review letters* 42.25 (1979), p. 1698.

[104] Jianwei Sun, Adrienn Ruzsinszky, and John P Perdew. "Strongly constrained and appropriately normed semilocal density functional". In: *Physical review letters* 115.3 (2015), p. 036402.

[105] LS Swanson et al. "Electroluminescence-detected magnetic-resonance study of polyparaphenylenevinylene (PPV)-based light-emitting diodes". In: *Physical Review B* 46.23 (1992), p. 15072.

[106] Leopold Talirz et al. "Termini of bottom-up fabricated graphene nanoribbons". In: *Journal of the American Chemical Society* 135.6 (2013), pp. 2060–2063.

[107] David J Thouless et al. "Quantized Hall conductance in a two-dimensional periodic potential". In: *Physical review letters* 49.6 (1982), p. 405.

[108] B Tian et al. "Optical spectra and structure of oligomeric models of polyparaphenylenevinylene". In: *The Journal of chemical physics* 95.5 (1991), pp. 3191–3197.

[109] Sri Krishna Vadlamani et al. "Tunnel-fet switching is governed by non-lorentzian spectral line shape". In: *Proceedings of the IEEE* 108.8 (2019), pp. 1235–1244.

[110] J-W Van der Horst, PA Bobbert, and MAJ Michels. "Electronic and optical excitations in crystalline conjugated polymers". In: *Physical Review B* 66.3 (2002), p. 035206.

[111] J-W Van Der Horst et al. "Excitons in conjugated polymers from first principles". In: *Computer physics communications* 147.1-2 (2002), pp. 331–334.

[112] Di Xiao, Ming-Che Chang, and Qian Niu. "Berry phase effects on electronic properties". In: *Reviews of modern physics* 82.3 (2010), p. 1959.

[113] Li Yang et al. "Quasiparticle energies and band gaps in graphene nanoribbons". In: *Physical Review Letters* 99.18 (2007), p. 186801.

[114] Liang Zhang et al. "Discovery of a novel spin-polarized nodal ring in a two-dimensional HK lattice". In: *Nanoscale* 10.44 (2018), pp. 20748–20753.

[115] SB Zhang et al. "Evaluation of quasiparticle energies for semiconductors without inversion symmetry". In: *Physical Review B* 40.5 (1989), p. 3162.

[116] Fangzhou Zhao, Ting Cao, and Steven G Louie. "Electric Field Tunable Topological Phases in Graphene Nanoribbons". In: *arXiv preprint arXiv:2102.04440* (2021).

[117] Fangzhou Zhao et al. "Optical excitations in poly(p-phenylene vinylene) polymer crystals in the GW plus Bethe-Salpeter equation approach". In: *In preparation* (2021).